Université de Montréal

Rôle de la tomodensitométrie à double énergie/double source pour la personnalisation des traitements de radiothérapie

Par Houda Bahig, MD

Directeurs
Dr Jacques de Guise
Dr David Roberge

Sciences Biomédicales, Faculté de Médecine

Thèse présentée en vue de l'obtention du grade de doctorat en
Sciences Biomédicales, option Médecine Expérimentale

Septembre 2018

TABLES DES MATIÈRES

1 RÉSUMÉ

Le futur de la radiothérapie réside dans le développement de stratégies visant à adapter les traitements à chaque individu. La tomodensitométrie à double énergie/double source (DECT/DSCT) est une technologie d'imagerie permettant de caractériser avec précision les tissus (sains et tumoraux) et d'imager le cœur en mouvement. En raison de ses fonctionnalités, la technologie du DECT/DSCT a le potentiel de jouer un rôle important dans la personnalisation des traitements de radiothérapie. Nous avons exploré le rôle du DECT/DSCT dans 3 études cliniques prospectives, relatives à la planification des traitements de radiothérapie.

Dans une première approche, nous avons évalué le rôle du DECT pour l'évaluation de la fonction du parenchyme pulmonaire en radiothérapie thoracique (conventionnelle et stéréotaxique). Nous avons émis l'hypothèse qu'une quantification précise de la concentration d'iode du parenchyme pulmonaire, dérivée du DECT, permettrait de déterminer les régions pulmonaires les plus fonctionnelles à éviter lors de la planification de la radiothérapie. Nous avons démontré la faisabilité et la validité d'une méthode de quantification de la fonction pulmonaire en utilisant la cartographie d'iode du DECT. De plus, nous avons montré que l'incorporation de cette information en planification de radiothérapie peut réduire significativement la dose aux régions pulmonaires fonctionnelles dans le but de réduire les toxicités.

Dans une deuxième approche, nous avons évalué le rôle du l'imagerie à double-source (DSCT) pour une évaluation individualisée du mouvement cardiaque lors de la planification des traitements de radiothérapie. Nous avons montré que le DSCT permettait de visualiser et quantifier le mouvement des sous-structures cardiaques notamment les veines pulmonaires et les artères coronaires, et ainsi déterminer un volume cible personnalisé pour chaque patient. De plus, nous avons montré le bénéfice dosimétrique d'une irradiation du sein gauche avec synchronisation cardiaque (limitée à la phase systolique) pour épargner les sous-structures cardiaques, notamment de l'artère antérieure descendante gauche, une structure critique dans le développement des toxicités cardiaques post-radiques.

Finalement, utilisant à nouveau la capacité de quantification précise de la concentration d'iode, nous avons évalué le rôle du DECT pour dériver la perfusion des tumeurs du larynx et de l'hypopharynx traitées par radiothérapie. Dans un contexte exploratoire de 25 patients, nous avons démontré que les statistiques quantitatives dérivées des cartes d'iodes tumorales étaient prédictives du contrôle locorégional chez ces patients, suggérant un rôle de ces cartes d'iode comme bio-marqueurs prédisant l'agressivité tumorale.

Les résultats de nos travaux centrés sur ces 3 stratégies démontrent que le DECT/DSCT a le potentiel de jouer un rôle important à divers niveaux dans la personnalisation de la planification des traitements radiothérapie, notamment: 1) pour l'évaluation de la fonction des tissus sains; 2) pour la détermination personnalisée du mouvement cardiaque, et 3) comme outil prédictif du contrôle tumoral.

Mots clés: *Tomodensitométrie à double énergie (DECT); tomodensitométrie à double source (DSCT); radiothérapie; cancer; toxicités; médicine personnalisée; imagerie fonctionnelle; imagerie cardiaque.*

2 ABSTRACT

The future of radiotherapy lies in the development of strategies to adapt treatments to each individual. Dual energy / dual source computed tomography (DECT/DSCT) is an imaging technology that allows for accurate tissue characterisation (organs at risk or tumors) and that can capture precisely the anatomy of the heart in motion. DECT/DSCT technology has the potential to be important player in personalized radiotherapy. We explored the role of DECT/DSCT in radiotherapy planning in the context of 3 prospective clinical studies.

First, we evaluated the role of DECT imaging for the assessment of lung function in lung cancer radiotherapy planning (both conventionally fractionated and stereotaxic radiotherapy). We hypothesized that accurate quantification of DECT iodine concentration could be used in treatment planning to assesses and preserve functional parenchyma. We demonstrated the feasibility and validity of a novel lung function quantification method using DECT iodine mapping. In addition, we showed that incorporating this information into radiotherapy planning could help improve lung dosimetry, and thus potentially reduce toxicities.

In a second approach, we evaluated the role of DSCT for individualized assessment of cardiac motion in radiotherapy planning. We showed that the DSCT allows visualization and quantification of motion of cardiac sub-structures, including the pulmonary veins and coronary arteries, and therefore can be used to determine personalized target volume for each patient. In addition, we quantified the dosimetric impact of cardiac-gated radiotherapy in left breast cancer radiotherapy and demonstrated significant sparing of cardiac sub-structures with this method, in particular sparing of left anterior descending artery, a critical structure involved in radiation-induced cardiovascular toxicities.

Finally, we assessed the role of DECT in determining tumor perfusion in larynx/hypopharynx cancers using the iodine concentration quantification method. In an exploratory prospective cohort of 25 patients with cancer of the larynx or hypopharynx, we demonstrated that histogram statistics derived from tumor iodine maps could predict locoregional control in these patients. This finding supports the role of iodine concentration maps as functional biomarkers to predict tumor aggressiveness.

The results of our work focused on these various strategies demonstrate that DECT/DSCT has the potential to play an important role in the following 3 avenues of personalized radiotherapy: 1) for the evaluation of functional healthy tissues; 2) for individualized determination of optimal margins or cardiac-gating window in radiotherapy involving the heart and, 3) for prediction of cancer control outcomes.

Key words: *Dual-energy computed tomography (DECT); dual source computed tomography (DSCT); radiotherapy; cancer; toxicities; personalized medicine; functional imaging; cardiac imaging.*

3 LISTE DES TABLEAUX/LIST OF TABLES

4 LISTE DES FIGURES/LIST OF FIGURES

5 REMERCIEMENTS

Premièrement, j'aimerai remercier mes 2 formidables directeurs de recherche : Les Drs Jacques de Guise et David Roberge. Je n'aurai pu espérer un meilleur duo pour supporter mon début de carrière en recherche et je les remercie pour la confiance et la liberté intellectuelle qu'ils m'ont accordée. Le Dr Jacques de Guise m'a accueilli les bras ouverts dans son monde de l'imagerie, m'a donné une grande autonomie tout en étant toujours disponible, mais surtout, il a été un rôle modèle inestimable. Le Dr Roberge, ce génie de la radio-oncologie qui « pense plus vite que son ombre », a été un mentor exceptionnel sans qui je n'aurai pu naviguer à travers les défis rencontrés. Je lui suis reconnaissante pour son support continuel et pour toutes les opportunités qu'il a mis sur mon chemin.

Je tiens également à remercier l'équipe de physique médicale, incluant les Drs Stéphane Bedwani, Andréanne Lapointe et Hugo Bouchard, ainsi que Danis Blais. Leur rigueur et leur créativité à solutionner les problèmes ont été cruciales à l'aboutissement de ce doctorat. De la même manière, j'aimerais remercier les cliniciens, notamment les Drs Edith Filion, Marie-Pierre Campeau, Toni Vu, Félix-Phuc Nguyen-Tan et Louise Lambert qui ont facilité l'implémentation des études cliniques, le recrutement de patients et qui ont offert leur support au quotidien. De plus, j'aimerais remercier les collaborateurs en radiologie et médecine nucléaire, notamment les Drs Carl Chartrand Lefebvre, Laurent Létourneau-Guillon et Martin Lord, qui ont généreusement offert leur expertise et ont été indispensables à assurer la validité des méthodes proposées.

Bien entendu il y a aussi la famille. Merci à mes parents pour leur amour inconditionnel et les

incomptables sacrifices, notamment leur courageux et altruiste parcours migratoire avec pour seul objectif d'offrir à leur enfants un avenir meilleur. Merci à mon fiancé pour sa patience inébranlable, ses encouragements au quotidien et son sens de l'humour imbattable.

Enfin, je voudrai souligner les sources de financement reçus pour la réalisation de ce projet, qui incluent : une bourse d'étude des Fonds de Recherche Santé Québec, une bourse de projet pilote du Réseau de Bio-Imagerie du Québec, les bourses de Support Professoral du département de Radiologie, Radio-oncologie et Médecine nucléaire de l'Université de Montréal, ainsi qu'une bourse de recherche de l'industrie de Varian Medical Systems®.

6 LISTE DES SIGLES ET ABBRÉVIATIONS

4D-CT:	Four-dimensional computed tomography
99mTc-MAA:	99m-Technetium macro-aggregated albumin
CI:	Confidence Interval
COPD:	Chronic obstructive pulmonary disease
CK:	CyberKnife®
CT:	Computed Tomography
DECT:	Tomodensitométrie à double énergie
DSCT:	Tomodensitométrie à double source
DIBH:	Deep-inspiration breath-hold
DLCO:	Diffusing capacity of the lungs for carbon monoxide
DVH:	Dose-volume histograms
ECG:	Electrocardiogramme
FAZA:	Fluoroazomycin arabinoside
FEV1:	Forced expiratory volume in 1 second
FDG:	Fluorodeoxyglucose
FMISO:	Fluoromisonidazole
FVC:	Forced vital capacity
FL:	Functional lung
HR:	Hazard ratio
IC:	Iodine concentration
IHC:	Immunohistochemistry

ITV:	Internal target volume
IMRT:	Intensity-modulated radiotherapy
LAD:	Left anterior descending artery
LLL:	Left lower lobe
LMCA:	Left main coronary artery
LRR:	Loco-regional recurrence
LUL:	Left upper lobe
LV:	Left ventricle
M:	Mean
MLD:	Mean dose
MRI:	Magnetic resonance imaging
N:	Number
NaCl:	Sodium chloride
NSCLC:	Non small cell lung cancer
PET:	Positron emission tomography
PTV:	Planning target volume
QUANTEC:	Quantitative Analysis of Normal Tissue Effects in the Clinic
RUL:	Right upper lobe
RML:	Right middle lobe
RLL:	Right lower lobe
SABR:	Stereotactic ablative radiotherapy
SCLC:	Small cell lung cancer
SPECT:	Single Photon Emission Computed Tomography

TPS:	Treatment planning system
V5:	Percent lung volume receiving 5 Gy
V20:	Percent lung volume receiving 20 Gy
WL:	Whole lung
WH:	Whole heart

7 INTRODUCTION GÉNÉRALE

7.1 LA RADIOTHÉRAPIE PERSONNALISÉE

L’objectif global de la radiothérapie est d’administrer la dose prescrite à la tumeur tout en réduisant la dose aux organes sains environnants. Dans les 2 dernières décennies, l’introduction de techniques comme la radiothérapie par modulation d’intensité (IMRT), la radiothérapie stéréotaxique et la radiothérapie guidée par l'imagerie ont permis d’augmenter significativement la précision des traitements (1, 2). Dans le contexte de l’utilisation grandissante d’imagerie multi-modalités pour la planification des traitements, il existe un intérêt croissant pour le concept d’une « radiothérapie personnalisée » visant à élargir l’indice thérapeutique (3). L’une des potentielles approches de « personnalisation » des traitements de radiothérapie consiste à intégrer non seulement l’information anatomique, mais également l’information fonctionnelle lors de la planification des traitements (4). Parmi ces applications, on compte par exemple le rôle de bio- marqueurs d’imagerie (résonnance magnétique, tomodensitométrie de perfusion ou tomodensitométrie par émission de positron) pour déterminer le volume cible à traiter ou prédire le comportement des tumeurs et le pronostic des patients (5-7). On compte également l’utilisation de bio-marqueurs pour évaluer la fonction des tissus sains environnants et estimer plus judicieusement la réserve de chaque patient pour minimiser les dommages radio-induits (8-10). D’autres applications comptent l’évaluation individualisée du mouvement tumoral ou des tissus sains, induits par exemple par la respiration, le péristaltisme, le mouvement aléatoire des organes ou les contractions cardiaques, dans le but d’utiliser des marges individualisés permettant de traiter la cible en mouvement, tout en protégeant maximalement les organes environnants (11-13). L'utilisation de plusieurs de ces applications en clinique demeure expérimentale. Ces diverses stratégies ont pour objectif global l'amélioration du contrôle tumoral, la réduction des complications post-radiques et la préservation de la qualité de vie des patients traités.

7.2 PRINCIPES GÉNÉRAUX DU DECT

L'imagerie par tomodensitométrie à double énergie (DECT) est basée sur le principe que l'utilisation des rayons X à 2 énergies différentes donne lieu à une atténuation spécifique à un matériau donné (14, 15). Cette caractéristique permet de distinguer et de mesurer la quantité des différentes substances comme l'iode ou le calcium du reste des tissus mous (16).

Aux énergies utilisées en imagerie, l'effet photoélectrique et l'effet Compton sont les 2 composantes les plus importantes d'atténuation des rayons X passant par un matériau donné (17). La composante d'atténuation de l'effet photoélectrique est fortement dépendante du numéro atomique Z du matériau traversé et inversement proportionnelle à l'énergie du faisceau. L'effet photoélectrique survient lorsqu'un photon incident a suffisamment d'énergie pour causer l'éjection d'un électron de la couche K (la couche la plus profonde) d'un atome. Les chances que l'effet photoélectrique se produise augmentent avec le rapprochement de l'énergie du photon incident de celle de l'énergie de liaison de la couche K (17, 18). Le coefficient d'extinction K d'une substance fait référence au pic d'atténuation observé à un niveau d'énergie juste au dessus de celui de l'énergie de liaison de la couche K - en raison de l'augmentation drastique de l'absorption photoélectrique à ce niveau d'énergie. Le coefficient d'extinction varie pour chaque matériau et est plus élevé avec l'augmentation des numéros atomiques (17).

Alors qu'avec un CT à simple énergie, la différentiation des différents matériaux n'est basée que sur leur atténuation à cette énergie spécifique (quantifiée en Unité Hounsfield) (19), le DECT permet la différentiation de matériau par l'interdépendance entre l'effet photoélectrique, l'énergie et la variabilité des coefficients d'extinction K pour chaque élément. L'acquisition de 2 séries d'images à différentes énergies permet donc de mesurer la différence d'atténuation entres les acquisitions de faible et haute énergie et ainsi de décomposer la matière en caractérisant les éléments qui la composent. Il devient ainsi possible de séparer par exemple l'iode, le calcium ou le Xénon du reste des tissus mous, en dérivant le contenu de chaque voxel (équivalent 3D du pixel, le voxel correspondant à la plus petite entité distinguable sur une imagerie tridimensionnelle) (16).

Il existe plusieurs types de DECT qui diffèrent dans la technique d'acquisition des séries de haute et faible énergie. Les images peuvent être acquises par l'utilisation de 2 sources de rayons X à 2 énergies différentes (dit, double-source) ou par l'utilisation d'une seule source (soit par alternance rapide de kV ou par utilisation d'un détecteur à 2 couches) (18). Dans le cadre de notre projet, nous utilisons une tomodensitométrie à double-source (DSCT ; *SOMATOM® Definition Flash, Siemens Healthineers*).

7.3 PRINCIPES GÉNÉRAUX DU DSCT

Bien que la tomodensitométrie à double source (DSCT) permette l'acquisition d'images à des énergies différentes et de bénéficier de l'information relative à l'atténuation différentielle, le

DSCT a été initialement développé pour l’imagerie cardiaque. En effet, les 2 tubes à rayon X disposés à 90° degrés l’un par rapport à l’autre, associés à leurs détecteurs correspondants, permettent une augmentation de la vitesse d’acquisition d’image et ainsi une résolution temporelle supérieure (20, 21) avec, dans le cas du DSCT utilisé dans le cadre de ce projet (*SOMATOM® Definition Flash, Siemens Healthineers*) un temps de rotation de 0.28 seconde et une résolution temporelle de 75 milisecondes. Le principal défi de l'imagerie cardiaque non invasive est celui de la visualisation précise des structures cardiaques, notamment des petites structures comme les artères coronaires et la paroi vasculaire, qui sont sujets à des artéfacts de mouvements liés à la contraction cardiaque. Les études initiales en imagerie diagnostique ont montré que l’acquisition de DSCT synchronisé à l’électrocardiogramme (ECG) permettait d’imager le cœur en mouvement indépendamment de la fréquence ou du rythme cardiaque, de visualiser les artères coronaires ainsi que d’évaluer l’étendue de leur mouvement, sans artéfacts de mouvement (20, 22-28). Le signal de l’ECG du patient est surveillé pendant l’examen et l’acquisition est déclenchée à une phase prédéfinie du cycle cardiaque. Bien que ceci n’ait pas été évalué en radiothérapie préalablement, l’utilisation du DSCT pour évaluer le déplacement du cœur et des sous-structures du cœur de la diastole à la systole aurait plusieurs implications pertinentes pour la personnalisation des traitements. Ces applications incluent notamment de déterminer des marges de traitements personnalisées dans les cas d’une irradiation thoracique où le coeur est un organe à risque (par exemple en radiothérapie du sein, poumon, ou autre structures thoracique), ou de faciliter le traitement de pathologies cardiaques en permettant une visualisation appropriée des structures cardiaques et de leur marge de mouvement. Enfin, à l’image de ce qui est fait en imagerie 4D respiratoire (29, 30), le DSCT pourrait permettre de déterminer de façon individualisée la fenêtre d’irradiation optimale pendant le cycle cardiaque, et ainsi élargir l'indice thérapeutique et minimiser les toxicités cardiaques liées à la radiothérapie.

7.4 HYPOTHÈSE ET RATIONNELLE DU PROJET

Actuellement, le flux de travail standard des traitements de radiothérapie débute par l'acquisition d'une tomodensitométrie dite *de planification*. Cette tomodensitométrie est utilisée pour préparer les traitements de radiothérapie, pour définir les volumes cibles, pour définir les organes sains à éviter et pour faire le calcul dosimétrique. Dans le contexte de la radiothérapie, le DECT/DSCT a l'avantage de pouvoir être facilement intégré dans le flux de travail des traitements tout en ajoutant l'information de la caractérisation tissulaire (en mode DECT) ou de l'évaluation du mouvement cardiaque (en mode DSCT). Contrairement aux autres multi-modalités d'imagerie souvent intégrées à la planification des traitements de radiothérapies comme l'IRM ou le PET scan par exemple, le DECT/DSCT à l'avantage particulier qu'il ne constitue pas un examen supplémentaire, mais qu'il peut simplement servir de tomodensitométrie de planification. Ainsi, l'information fournie par le DECT/DSCT a l'avantage particulier d'être exactement en position de traitement et donc de ne pas nécessiter l'étape supplémentaire de fusion. En plus de faciliter le flux de travail, ce dernier point a aussi l'avantage d'une meilleure précision anatomique, comparativement a une imprécision de plusieurs millimètres associée à l'étape de fusion du scan de planification avec un autre modalité comme l'IRM par exemple (31).

L'hypothèse centrale de notre projet est que l'utilisation du DECT/DSCT comme tomodensitométrie de planification dans le flux de travail de la radiothérapie, peut jouer un rôle important dans l'individualisation des traitements de radiothérapie pour la réduction de la dose aux organes à risques, de même que pour la prédiction de la réponse tumorale. Dans ce cadre, nous avons procédé à l'évaluation de cette technologie dans 3 contextes cliniques pertinents à la planification de la radiothérapie :

a) Première approche: Le DECT pour l'évaluation de la fonction pulmonaire (publication 1)

La première approche évaluée est celle du rôle de l'imagerie à double-énergie pour l'évaluation de la fonction des tissus sains en radiothérapie pulmonaire (conventionnelle et stéréotaxique). Lors d'une irradiation thoracique, les contraintes de dose utilisées pour les poumons dans le but de minimiser le risque de toxicités ont pouvoir de prédiction variable, avec des taux de pneumonite estimés variant entre 5 and 40%, dépendamment des techniques, des doses et du volume pulmonaire irradié (32). Les contraintes de dose utilisées en clinique sont exprimées sous forme de dose moyenne aux poumons et/ou d'histogramme dose-volume. Un problème important de ces contraintes est qu'elles considèrent que chaque voxel pulmonaire contribue également à la fonction des poumons; elles ne prennent donc pas en compte la fonction pulmonaire souvent asymétrique d'une majorité de patients atteints de maladie pulmonaire obstructive chronique. Dans le cadre de cette première étude, nous avons émis l'hypothèse que la caractérisation tissulaire et la quantification précise de l'iode dans le parenchyme pulmonaire au DECT permettraient d'établir une corrélation anatomo-fonctionnelle précise, qui pourrait être utilisée lors la planification des traitements afin de préserver le parenchyme fonctionnel. L'objectif de cette étude prospective est de quantifier la fonction pulmonaire basée sur la cartographie d'iode dérivée du DECT chez les patients traités pour un cancer pulmonaire ainsi que d'évaluer l'impact dosimétrique de l'intégration de ces cartes d'iode en planification de radiothérapie. Étant donné que la littérature actuelle sur les toxicités pulmonaires démontre une relation linéaire entre la réduction de dose aux poumons et les risques de pneumonites post-radiques, le potentiel clinique d'une telle méthode est celui de réduire les risques de toxicités.

b) Deuxième approche: Le DSCT pour évaluer le mouvement cardiaque (publications 2 et 3)

Dans un deuxième temps, explorant le fait que le DSCT offre la possibilité d'évaluer le mouvement cardiaque et de visualiser les coronaires et le myocarde, nous avons évalué le rôle du DSCT pour une évaluation personnalisée du mouvement cardiaque lors de la planification des traitements de radiothérapie. Le coeur étant fréquemment inclus dans les champs tangentiels d'une radiothérapie du sein gauche, il a été démontré que le risque de maladies ischémiques est augmenté suite à une irradiation du sein gauche (33). Dans une cohorte prospective de 10 patientes traitées par radiothérapie limitée au sein gauche, nous avons évalué 2 questions cliniques. Dans une première étude, nous avons quantifié le potentiel bénéfice dosimétrique d'une irradiation du sein gauche avec synchronisation cardiaque, permettant une épargne des sous-structures cardiaques. Plus précisément, nous avons évalué la variation de dose aux différents segments de l'artère antérieure descendante gauche, à l'artère coronarienne gauche, au ventricule gauche et au cœur pendant le cycle cardiaque (de la systole à la diastole). En utilisant la même cohorte de patientes dans une seconde étude, nous avons évalué l'amplitude de déplacement de l'antrum veines pulmonaires lors du battement cardiaque dans le but de déterminer un volume cible personnalisé dans la nouvelle avenue du traitement par radiothérapie stéréotaxique d'arythmies cardiaques réfractaires.

c) Troisième approche: Le DECT pour évaluer la perfusion tumorale (publication 4)

Comme deuxième approche, nous avons évalué le rôle du DECT pour évaluer la perfusion tumorale dans les cancers de la tête et du cou. Nous avons émis l'hypothèse que suite à l'acquisition d'un DECT injecté en phase artérielle, la concentration tumorale d'iode dérivée du DECT serait représentative de la perfusion tumorale. Une concentration d'iode plus élevée serait indicative d'une augmentation du volume sanguin et d'une hyperperméabilité capillaire représentant une néoangiogenèse augmentée. Dans une cohorte prospective de 25 patients avec des cancers du larynx supraglottique ou de l'hypopharynx, nous avons investigué le rôle des données statistiques quantitatives dérivées des cartes d'iodes tumorales du DECT pour prédire les récidives locoregionales.

8 PREMIER ARTICLE SCIENTIFIQUE

Phase I-II Study of Dual-Energy Computed Tomography (DECT) for Assessment of Pulmonary Function in Radiotherapy Planning

Houda Bahig, MD[1], Marie-Pierre Campeau, MD[1], Andréanne Lapointe MSc[1], Stephane Bedwani PhD[1], David Roberge MD[1], Jacques de Guise PhD[2], Danis Blais MSc, [1] Toni Vu MD[1], Louise Lambert MD[1], Carl Chartrand-Lefebvre MD MSc[3], Martin Lord MD[4], Edith Filion MD[1]

[1] Radiation Oncology department, Centre Hospitalier de l'Université de Montréal, Montreal, Quebec, Canada

[2] Imaging and Orthopaedics Research Laboratory (LIO), École de Technologie Supérieure, Centre de Recherche du Centre Hospitalier de l'Université de Montréal (CRCHUM), Montreal, Quebec, Canada

[3] Radiology departement, Centre Hospitalier de l'Université de Montréal, Montreal, Quebec, Canada

[4] Nuclear medicine department, Centre Hospitalier de l'Université de Montréal, Montreal, Quebec, Canada

Keywords: *Dual energy CT, Lung, Thoracic radiotherapy, SBRT, IMRT, functional imaging, iodine contrast, tissue characterization, dosimetry, radiation pneumonitis.*

Publication:
Int J Radiat Oncol Biol Phys. 2017 Oct 1;99(2):334-343. doi: 10.1016/j.ijrobp.2017.05.051. Epub 2017 Jun 7.

CONTRIBUTIONS: Rédaction du protocole de recherche, coordination et gestion de l'implémentation du protocole de recherche en clinique, récole et analyse des données, interprétation des données, rédaction du manuscrit.

8.1 ABSTRACT

Purpose: To quantify lung function based on a dual energy computed tomography (DECT)-derived iodine map in patients treated with radiotherapy for lung cancer, and to assess the dosimetric impact of its integration in radiotherapy planning.

Methods: Patients treated with stereotactic ablative radiotherapy (SABR) for early stage or intensity-modulated radiotherapy (IMRT) for locally advanced lung cancer were prospectively enrolled in this study. A DECT in treatment position was obtained at time of treatment planning. The relative contribution of each voxel to the total lung function was based on iodine distribution. The composition of each voxel was determined based on a two-material decomposition. DECT-derived lobar function was compared to Single Photon Emission Computed Tomography / Computed Tomography (SPECT/CT). A functional map was integrated in treatment planning system using 6 sub-volumes of increasing iodine distribution levels. Percent lung volume receiving 5Gy (V5), V20 and mean dose (MLD) to whole lungs (anatomical) vs. functional lungs were compared.

Results: 25 patients, including 18 patients with lung cancer treated with SABR and 7 patients with IMRT (locally advanced), were included. Eighty-four percent had chronic obstructive pulmonary disease. Median forced expiratory volume in 1 second was 62% of predicted (29-113%) and median diffusing capacity of the lung for carbon monoxide was 56% (39-91%). There was a strong linear correlation between DECT and SPECT/CT-derived lobar function (Pearson's coefficient correlation r= 0.89, p<0.00001). Mean differences in V5, V20 and MLD between anatomical and functional lung volumes were 16% (0-48%, p=0.03), 5% (1-15%, p=0.12) and 15% (1-43%, p=0.047), respectively.

Conclusion: Lobar function derived from DECT iodine map correlates well with SPECT/CT and its integration in lung treatment planning is associated with significant differences in V5 and MLD to functional lungs. Future work will involve integration of weighted functional volume in the treatment planning system, along with integration of iodine map for functional lung-sparing IMRT.

8.2 INTRODUCTION

The goal of lung cancer radiotherapy is to administer the prescribed dose to the tumor while minimizing the dose to the surrounding healthy lungs and other organs at risk. Radiation-induced pulmonary toxicities include a wide spectrum of events ranging from subclinical radiological changes to fatal complications of respiratory failure (34). Rates of clinical radiation pneumonitis (RP) after radiotherapy for lung cancer vary between 5 and 50% in the literature (35). In lung stereotactic ablative radiotherapy (SABR) as well as in conventional radiotherapy, several dose parameters are used to predict the risk of RP, the most commonly used being: mean lung dose (MLD) (32) as well as volume receiving 5 Gy (V5), 20 Gy (V20), 30 Gy (V30) and 60 Gy (V60) (36, 37). However, these parameters were shown to have a highly variable predictive power for RP risk estimation. This was hypothesised to be due to heterogeneities in patient-related (comorbidities/smoking habits) and treatment-related factors, which significantly decrease the sensitivity of these parameters (35, 37). Nonetheless, data from the Quantitative Analysis of Normal Tissue Effects in the Clinic (QUANTEC) (32) suggest that there is no threshold below which RP risk is null and highlights the importance of lung-sparing strategies.

More than half of lung cancer patients have concomitant pulmonary disease (38), and therefore have reduced and inhomogeneous lung function. Marks et al. (39) showed that exclusion of patients with severe chronic obstructive pulmonary disease (COPD) from the QUANTEC analysis was associated with markedly increased sensitivity of lung dose-volume histograms (DVH). This suggested that functional lung volume information may be more useful than anatomical lung volume for these patients. In the context of both 3D conformal radiotherapy and intensity modulated radiotherapy (IMRT), functional lung avoidance has been proposed in several feasibility studies (40). While Single Photon Emission Computed Tomography (SPECT) perfusion scintigraphy is the most studied method for evaluation of relative pulmonary function (41), in recent years, several alternative methods have emerged, including the use of hyperpolarized gas magnetic resonance imaging (MRI) (42), four-dimensional (4D) CT ventilation maps (43) (44) (45) and 4D positron emission tomography(PET)/CT (46). These methods have diverse potential advantages in comparison to SPECT/CT, including avoidance of ionizing radiation and improvement of anatomical precision.

Dual-energy computed tomography (DECT) is an advanced imaging technique, recently introduced in radiation oncology. Based on the principle that the use of two different X-ray energies results in an attenuation specific to a given material, this technique has the potential to provide better tissue characterization (15). This characteristic of the DECT allows for precise voxel-to-voxel determination of iodine partial electronic density, which can be used to derive a regional blood volume map (16). Our hypothesis is that a DECT-iodine map of the lungs derived from a contrast-injected CT at time of planning would provide precise lung anatomical and functional information. This information can be used at time of treatment planning for a better estimation of delivered dose to functional lung. Compared to previously developed methods, the proposed technique has the advantage of deriving lung function directly from the treatment planning CT, therefore simplifying workflow, at no additional ionising radiation cost. The purpose of the current study was to quantify relative lung function using DECT-iodine map and correlate these results with SPECT/CT (current standard). The secondary objective was to compare whole (anatomical) lung to functional lung dosimetry in patients treated for lung cancer.

8.3 MATERIAL & METHODS

Patient population

Patients were prospectively enrolled in this study from September 2014 to June 2016. Eligibility criteria included: (1) a clinical diagnosis of lung cancer; (2) Eastern Cooperative Oncology Group performance status 0-2; (3) planned curative radiotherapy. Exclusion criteria were: previous radiotherapy, iodine allergy or other contra-indications to iodine injection. Patients with locally advanced lung cancer treated with concurrent or sequential chemotherapy could be included in this study. Baseline work-up included: thoracic computed tomography (CT) scan, bronchoscopy, 18-fluoro-2-deoxy-d-glucose positron emission tomographic (FDG-PET) scan, pulmonary function tests and, when available, histological confirmation. In selected early stage cases where histological confirmation could not be obtained, tumor progression on CT and increased FDG-PET uptake were used to establish the clinical diagnosis of malignancy. All cases were discussed in the context of a multidisciplinary tumor board. The protocol and patient consent form were reviewed and approved by our institutional ethics committee and all patients signed a consent form.

Planning CT, DECT and SPECT/CT

The dual-source DECT available in our department (SOMATOM Definition Flash; Siemens Healthineers) was used for planning purposes. Planning CT was acquired in supine position, with the arms along the sides. Immobilisation at the time of treatment planning was individualized based on treatment technique and involved a custom vacuum cushion or a double vacuum immobilization device (BodyFix, Elekta, Stockholm, Sweden). All patients had a 2 mm slice thickness single-energy non-contrast four-dimensional (4D) supine planning CT-scan in free breathing. A 3D contrast enhanced DECT in suspended breathing (end-expiration) was subsequently obtained in treatment position, using an angiography protocol for optimal visualisation of lung perfusion (47). Iopamidol contrast bolus was injected (Isovue 370 mg/mL) in the antecubital vein at a rate of 4 mL / seconds over 16 seconds (total of 64 mL). Immediately after, a 24 mL saline solution with 50% contrast concentration and a 40 mL saline solution were sequentially injected at a rate of 4 mL / sec. DECT was acquired in distal arterial phase, 7 seconds after contrast bolus tracking in the pulmonary trunk (47), with acquisition from inferior to superior direction to limit artefacts caused by contrast accumulation in the superior vena cava and supraclavicular veins. Two sets of spiral CT data were simultaneously acquired with the following parameters: slice thickness of 2 mm, pitch of 0.55, rotation time of 0.28 seconds, collimation of 64 x 0.6 mm and X-ray tube potentials of 100 kVp and 140Sn kVp (Sn= additional tin filtration), a matrix of 512 × 512 pixels, a field of view of 50 cm and a voxel size of 1 x 1 x 1 mm^3. A Q30 filter kernel was used for image reconstruction. Care Dose (Siemens Healthineers) technology was used for modulation of tube current in order to maintain constant image quality. All patients also underwent pre-treatment 99m-Technetium macro-aggregated albumin (99mTc-MAA) SPECT/CT. All studies were performed on a SPECT/CT camera (Discovery NM/CT 670, GE Healthcare) after intravenous administration of 99mTc-MAA (mean dose of 292 Megabecquerel). The SPECT was acquired in supine position with the arms elevated over the head in order to limit artefact at the thorax (48) and in free breathing, with the following parameters: 20% energy window centered at 140 keV, 60 projections/360°, matrix 128 x 128 and voxel size 3.45 x 3.45 x 3.45 mm^3. SPECT and CT were subsequently fused using rigid co-registration. A low-dose non-enhanced CT was acquired immediately before the perfusion SPECT acquisition, in same position as SPECT and in free breathing. Low dose CT parameters were as follows: slice thickness of 1.25 mm, pitch of 1.375, rotation time of 0.5 s, collimation of 16 x 0.625 mm and X ray tube potential of 120 kVp.

Radiotherapy

Patients with early stage lung cancer were treated with either: (1) CyberKnife (CK) near-real time tumor tracking (Synchrony or Xsight Lung, VSI 2013-2014, Accuray, Sunnyvale, CA), or (2) linac-based volumetric arc modulated radiotherapy (RapidArc®, Varian Medical Systems, Palo Alto, CA) using an internal target volume (ITV). Multiplan Treatment planning system (TPS) (Accuray, Sunnyvale, CA) with Monte Carlo calculation algorithm was used for CK plans whereas Eclipse TPS (Varian Medical Systems, Palo Alto, CA) with Analytical Anisotropic Algorithm was used for volumetric arc modulated radiotherapy. Patients with locally advanced disease were treated on a Varian iX linear accelerator and were planned on Eclipse TPS system using Analytical Anisotropic Algorithm. Patients underwent standard treatment planning with optimization on whole lung volume. All patients were treated in free breathing; motion management involved either tumor tracking for patients treated with robotic SBRT or use of an internal target volume based on 4DCT motion analysis for all other patients. For lower lobe tumors with > 1 cm motion treated with an internal target volume, abdominal compression was used as tolerated by the patient. For dosimetric purposes, whole lung volume was defined as total lung minus planning treatment volume. Dose limits to lungs and other organs at risk were as per RTOG 0236 and RTOG 0813 constraints in SABR, and as per RTOG 0617 in IMRT.

Iodine map vs. SPECT/CT

A radiation oncologist (HB) proceeded to manual segmentation of right upper lobe (RUL), right middle lobe (RML), right lower lobe (RLL), left upper lobe (LUL) and left lower lobe (LLL) on both DECT and SPECT/CT, for each patient (Figure 1). Using an in-house script (Matlab — MathWorks, Natick, MA), iodine concentration was extracted by determining the iodine partial electron density from each voxel of the lungs, using a two-material decomposition method (contrast agent and lung tissue) (49). Lung perfusion was hypothesized to be linearly correlated to iodine content in the lung parenchyma. Larger blood vessels were automatically removed using an upper threshold of -250 Hounsfield units, in order to isolate lung parenchyma. Total lung function was defined as the sum of iodine content (in mg/mL) of all the voxels within the lung parenchyma (50). Relative function of each lung lobe was defined as the sum of iodine content of each voxel in the given lobe divided by the iodine content of the whole lung parenchyma. Similarly, for SPECT maps, relative function of each lobe was defined as the sum of radioactive count per voxel within the given lobe relative to total lung parenchyma count.

Whole lung vs. functional lung dosimetry

Treatment planning data from all patients were digitally transferred to the TPS (Varian Medical Systems, Palo Alto, CA). Because our clinical treatment planning systems do not support weighted volumes, functional lung volume was imported under 6 functional sub-volumes; for each patient, the range from minimum to maximum iodine concentration was subdivided into 6 equal intervals of iodine concentration within the map (Figure 2). For the entire cohort, mean iodine concentration was 0.2 mg/mL (0.2-0.3), 0.9 mg/mL (0.7-1.1), 1.5 mg/mL (1-1.9), 2.1 mg/mL (1.3-2.5), 2.7 mg/mL (1.7-3.3) and 4.2 mg/mL (3.3-7.6), for sub-volumes 1 to 6. Each of these sub-volumes was considered a structure (organ at risk) with a weighted contribution to whole lung function. Delivered radiation plans (optimised on anatomical lungs) were retrospectively applied to functional sub-volumes. Dose-volume histograms of each sub-volume were added according to their weight, to obtain total functional V5, V20 and MLD. Standard whole lung V5, V20 and MLD derived from anatomical lungs were also assessed.

Statistics

Pearson coefficient was used to correlate relative function of individual lung lobes derived from SPECT/CT vs. DECT iodine maps. To detect a strong correlation between the 2 methods ($r \geq 0.6$), at a threshold of 5% (for a bilateral test) and with a power of 80%, 24 patients were necessary. Whole lung dosimetry was compared to functional dosimetry using nonparametric Wilcoxon signed rank test for paired sample, with p values $p<0.05$ considered statistically significant, from two-sided tests. SPSS 24 (IBM, Armonk, NY) was used for statistical analysis.

8.4 RESULTS

Patients and treatments characteristics

Patients and treatment characteristics are summarized in **Table 1**. In total, 25 patients were prospectively enrolled. Among these, 72% presented early stage lung cancer (TNM stage IA-IB), whereas the remaining 28% had stage IIIA disease. In addition, 68% had non-small cell lung cancer histology, and 1 patient was treated for limited stage small cell lung cancer. Histological confirmation could not be obtained for 7 patients with early stage disease because of poor lung function or a technically difficult biopsy. Eighty-four percent of patients had a prior diagnosis of chronic obstructive lung disease. For the whole group, median percent forced expiratory volume in 1 second (FEV1), absolute FEV1, percent forced vital capacity (FVC), absolute FVC, and diffusing capacity of the lungs for carbon monoxide (DLCO) were 60% (19-131%), 1.2 L (0.4-3.9 L), 76% (45-130), 2.3 L (1.4-4.4) and 56% (39-91%) of predicted, respectively. Mean volume CT dose index for DECT acquisition was 20.2 mGy (4.4-28.8 mGy). All patients with locally advanced disease treated with IMRT received concurrent chemotherapy. SABR and IMRT median dose and fractions were 60 Gy in 3 fractions and 66 Gy in 33 fractions, respectively. Patient and treatment characteristics are summarized in **Table 1.**

DECT-iodine map vs. SPECT/CT for lung function assessment

Mean iodine concentration in whole lungs volume was 1.7 mg/mL (1.1-2.3 mg/mL). Median relative functions for each lung lobe, derived from DECT-iodine map and SPECT/CT, are detailed in **Table 2**. **Figure 3** shows an example of DECT-iodine map and the corresponding SPECT/CT in a patient with COPD and severe functional asymmetry. As shown in **Figure 4**, a strong correlation was found between lobar function derived from DECT-iodine map vs. SPECT/CT (r= 0.89, p<0.00001). There were only weak correlations between mean iodine value of the overall lung parenchyma and percent FEV1 (r= 0.38), absolute FEV1 (L) (r=0.49), percent FVC (r= 0.28), absolute FVC (L) (r= 0.064) and DLCO (r= 0.47).

Whole lung vs. functional lung dosimetry

Table 2 summarizes whole lung vs. functional lung dosimetry (mean MLD, V5 and V20) for the entire cohort, as well as for SABR and IMRT patients specifically. Looking at differences between whole vs. functional lung V5, we find a mean relative variation of +/-16% (0-102%) and a mean absolute variation of +/- 3% (0-10%), p=0.047. Similarly, for mean relative MLD variation was +/-14% (1-58%) and mean absolute MLD variation was 1 Gy (0.0-5.4), p=0.03. Lastly, mean relative V20 variation was 6% (1-28%) and mean absolute V20 variation was 1% (0-9%), p=0.087. Relative variations in MLD, V5 and V20 between whole lung vs. functional lung dosimetries for each patient are shown in **Figure 5**. **Figure 3** shows an example of a patient treated with SABR where whole lung dosimetry significantly underestimated dose to functional lung (whole lung V5 of 10% vs. functional lung V5 of 20%).

More specifically per treatment technique, mean absolute variation of MLD was 1.5 Gy (0.1-5.4 Gy) in the IMRT group vs. 0.5 Gy (0.0-1.7 Gy) in the SABR group (p= 0.046). Mean absolute variation in V20 was 3% (0-9%) in the IMRT group vs. 1% (0-3%) in the SABR group (p=0.048). Mean absolute V5 variation was the same in patients treated with IMRT and SABR (3% (0-10%)).

8.5 DISCUSSION

Although current clinical evidence for the use of DECT in radiotherapy is limited, potential applications in radiotherapy planning are numerous and include more precise dose calculation (51-53), metal artefact reduction (54) as well as improved tumor delineation and normal tissue characterization (15, 55-57). This study is the first report on the use of functional DECT imaging in radiotherapy planning. Single-energy CT differentiates materials based on their attenuation at a specific energy (quantified in Hounsfield Unit). The acquisition of 2 series of images at different energies (usually 80-100 kV and 120-140 kV) exploits the principle of variable energy-dependant photoelectric effect and allows to determine material-specific difference in attenuation between low and high energy acquisitions (15). With precise material decomposition, it becomes possible to distinguish and quantify different substances such as iodine from the remaining soft tissues on DECT imaging (16). In the current study, a thoracic DECT in treatment position was used to extract the iodine fraction of each lung voxel, serving as a surrogate for regional blood volume, in order to derive split lung function.

Quantitative radionuclide pulmonary perfusion scintigraphy has been widely studied in the context of pre-operative assessment of parenchymal lung disease (58, 59) and remains the standard for evaluation of relative lung function (60-62). Because the combination of SPECT with low dose CT provides better spatial resolution and 3D anatomical information, SPECT/CT was chosen as the standard for the evaluation of lung function in the context of this study. We showed that DECT-iodine maps were strongly correlated with SPECT/CT for lung function assessment. This is in concordance with several studies showing that iodine distribution from DECT could be used to detect perfusion defects in the context of pulmonary embolisms (63-67) and parenchymal lung disease (68, 69). Pansini et al. (68) used DECT-iodine maps in 57 patients, including 37 patients with emphysema; their study showed that areas of decreased iodine distribution significantly matched areas of emphysema and that the severity of perfusion alteration was correlated with severity of parenchymal destruction. To date, the role of DECT-iodine maps for assessment of pre-operative lung function has been investigated in only one study (70). In that study, Chae et al. compared pre- and post-operative DECT and perfusion scintigraphy for prediction of post-operative pulmonary function tests (70). Their group reported a 15% vs. 18% error in post-operative estimation of FEV1 with DECT vs. scintigraphy, respectively, suggesting that DECT may have a higher accuracy.

Integration of functional information in lung radiotherapy planning has the potential to better predict lung toxicity as well as to spare most functional lung areas. Use of SPECT/CT-derived function has previously been extensively reported in lung radiotherapy (40, 71, 72). In recent years, several alternative lung function assessment methods including hyperpolarized gas MRI (73-76), 4DCT-based ventilation (43, 44, 77), thin section quantitative CT (78) or 4D PET/CT (46) have also been reported in the context of small feasibility studies. Although direct comparison between these studies is limited by the use of widely different methodologies, these studies have reported variable improvements of lung dosimetry parameters with the use of functional-avoidance (46, 74, 79-84). In our study, while no functional-avoidance optimisation was performed, dosimetric assessment of standard radiation plan showed that integration of iodine map led to significant differences in V5 and mean dose to anatomic vs. functional lung in both SABR and IMRT. The inaccuracy (over or under-estimation) of actual dose to functional parenchyma could explain, at least partly, the variable predictive power of current whole lung dosimetric parameters (32). Importantly, the use of functional information has so far never been evaluated in lung SABR. In our study, although absolute dose variations between functional and anatomical dosimetry were larger in the IMRT group, we report that significant variations in V5 and MLD also occur in SABR, suggesting that functional information integration is also important in these patients. In fact, the large number of radiation field entries and the increased conformity of SABR treatments, along with a pre-selection of non-operable or borderline operable patients with poorer lung function, makes function-sparing SABR particularly appealing.

The clinical benefit of the integration of functional information in IMRT (for locally advanced disease) as well as in SABR (for early stage disease) remains to be demonstrated. In a recent literature review that included 6 clinical studies integrating perfusion SPECT in lung radiotherapy planning, use of functional dosimetry was most beneficial in patients with emphysema or large areas of perfusion deficit and functional dose-volume histograms appeared to improve RP risk estimation (85). An important prospective study by Farr et al. involving 58 lung cancer patients treated with IMRT showed that SPECT-based functional MLD, V5, V10, V20 and V30 provided superior RP risk estimation compared to the standard whole lung dosimetric counterparts (86). Similarly, Kimura et al. looked specifically at functional MLD and V20 and reported a strong correlation with development of grade 2 ≥ RP (87). Currently, at least 4 clinical trials assessing the clinical impact of functional information in lung radiotherapy are on-going: 1) a double blind randomized trial evaluating hyperpolarized gas MRI (NCT02002052); 2) a single blind randomized trial using 4DCT (NCT03077854); 3) a feasibility trial on the use of 4DCT ventilation in treatment planning

(NCT02528942) and; 4) a phase II trial investigating SPECT/CT-based functional avoidance for toxicity prediction (NCT02773238).

The use of DECT-iodine map is particularly attractive in radiotherapy as it offers several advantages. First, DECT-iodine map can be derived from a contrast-injected scan in treatment position, and therefore provides perfect fusion with precise anatomical and functional correlation. As contrast-injected scans are routinely obtained at time of radiotherapy planning, notably for central or node-positive tumors, integration of DECT-iodine mapping would be straightforward in the current workflow as it obviates the need for an additional exam in nuclear medicine, which would also increase unnecessary radiation dose. It is estimated that up to 70% of patients with lung cancer have concurrent chronic obstructive lung disease (88) and therefore would have some excepted degree of parenchymal asymmetry. DECT scanners being slowly adopted in radiation oncology (most notably in proton centers), the DECT-iodine map has the potential to allow global acquisition of functional information in any patient undergoing thoracic radiotherapy; systematic, individualized plan optimization could then be performed by sparing of the most contributing lung areas. However, an evident downside of this method is the necessary use of iodine contrast, which limits its use in any patients with contra-indications to contrast agent.

This preliminary study on the role of DECT for assessment of lung function in radiotherapy planning has several limitations but should be seen as a first step towards the clinical implementation of this innovative, dose neutral and easily implementable method in the global process of radiotherapy planning. First, as the primary goal was to assess the validity of DECT-based functional information and feasibility of iodine-map integration in planning, this study did not involve planning re-optimization based on lung function. Further clinical data is needed to define if there is a threshold of iodine below which parenchyma needs not to be spared at all. Our use of discrete functional sub-volumes in the treatment planning system decreases the voxel-to-voxel precision of the initial iodine-map. The development of methods allowing the use of weighted volumes in clinically approved TPS is needed for the best use of function-sparing optimization. As current TPS are not conceived for optimization of low doses, early integration could involve selecting beam angles or arcs to pass through less functional lung. Another limitation is the current lack of 4D functional information accounting for respiratory motion. In fact, dose calculation is typically achieved on the average 4DCT whereas DECT was obtained in end-expiratory position. While this likely decreased the precision of the registration, end-expiratory position represents the worst-case scenario for lung dosimetry and is routinely used in our institution for whole lung volume delineation. In addition, the added use of 4DCT could potentially allow for ventilation information. Despite these limitations, this study represents an important step towards the promising clinical use of a simple, low-cost and dose-neutral method for lung function assessment in radiotherapy planning.

8.6 CONCLUSION

We have reported innovative and promising integration of functional DECT imaging in radiotherapy. DECT-iodine maps strongly correlate with standard SPECT/CT for evaluation of differential lung function. The use of functional imaging reveals significant variation in functional dosimetric parameters as compared to standard anatomical dosimetry in SABR and IMRT plans. These discrepancies may partially explain the suboptimal predictive power of standard anatomical DVH parameters and future work will involve integration of weighted functional volumes in the planning process. Such integration should lead to better sparing of lung function in pulmonary radiotherapy.

8.7 TABLES ET FIGURES

Table 1- Characteristics of patients with lung cancer enrolled in the study

Patients characteristics		
Median age (years)		69 (53-81)
Gender (n ; %)		
	Female	14 (56%)
	Male	11 (44%)
Histology (n ; %)		
	NSCLC	17 (68%)
	SCLC	1
	N/A	7 (28%)
TNM stage (n ; %)		
	IA	16 (64%)
	IB	2 (8%)
	IIIA	7 (28%)
Localisation (n ; %)		
	Inferior lobe	7 (28%)
	Middle lobe	4 (16%)

	Superior lobe	14 (56%)
Pulmonary function		
	Median FEV1 (%)	60 (19-131)
	Median FEV1 (L)	1.2 (0.4-3.9)
	Median FVC (%)	76% (45-130)
	Median FVC (L)	2.3 (1.4-4.4)
	Median DLCO (%)	56 (39-91)
COPD (n ; %)		21 (84%)
SPECT/CT function		
	Left lung (%)	45 (21-63)
	Right lung (%)	55 (37-79)
Median time between SPECT/CT and planning CT (days)		11 (1-60)
	Treatment characteristics	
SABR (n ; %)		18 (72%)
	ITV technique	15 (84%)
	Tumor tracking	3 (16%)
	Median dose (Gy, range)	60 (50-60)
	Median fractions (n, range)	3 (3-5)
	Median PTV (cm^3)	30 (5-53)
IMRT (n ; %)		7 (28%)
	Median dose (Gy, range)	66 (40-66)
	Median fractions (n, range)	33 (15-33)
	Median PTV (cm^3, range)	250 (6-1012)
Concurrent chemotherapy (n ; %)		7 (28%)

NSCLC= Non small cell lung cancer; SCLC= Small cell lung cancer; N/A= not available; FEV1= Forced expiratory volume in 1 second; FVC= Forced vital capacity; DLCO= Diffusing capacity for carbon monoxide; COPD= Chronic obstructive lung disease; SPECT/CT= Single photon emission computed tomography; SABR=

Stereotactic ablative radiotherapy; IMRT= Intensity modulated radiotherapy; Gy= Gray; ITV= Internal target volume; PTV= Planning target volume; n= number.

Table 2- DECT vs. SPECT/CT- derived lobar function and summary of WL vs. FL dosimetry

Median lobar function				
	DECT iodine map		**SPECT/CT**	
Lobe	Median	Range	Median	Range
RUL	19%	2-32%	22%	7-30%
RML	9%	3-15%	10%	5-13%
RLL	27%	18-44%	25%	18-42%
LUL	23%	7-36%	26%	10-33%
LLL	22%	1-42%	20%	4-32%

Mean lung dosimetry						
	WL	**FL**	**WL**	**FL**	**WL**	**FL**
	All patients (n= 25)		SABR (n=18)		IMRT (n=7)	
MLD (Gy ; range)	5.9 (1.6-17.3)	5.5 (1.1-18.0)	3.3 (1.6-7.5)	5.5 (1.1-18)	12.8 (6.4-17.3)	11.9 (6.3-18.0)
V5 (%; range)	22 (7-60)	21 (5-58)	14 (7-28)	15 (5-25)	42 (26-60)	40 (31-58)
V20 (%; range)	9 (1-29)	8 (1-31)	4 (1-14)	4 (1-12)	21 (13-29)	20 (12-31)

RUL= Right upper lobe; RML= Right middle lobe; RLL= Right lower lobe; LUL= Left upper lobe; LLL= left lower lobe; WL = Whole lung; FL = Functional lung; n= number of patients; MLD=mean lung dose; Gy= Gray; V5= percent lung volume receiving 5 Gy or more; V20=percent lung volume receiving 20 Gy or more; SABR= stereotactic body radiotherapy; IMRT = intensity modulated radiotherapy.

Figure 1- Manual segmentation of lung lobes on DECT and SPECT/CT

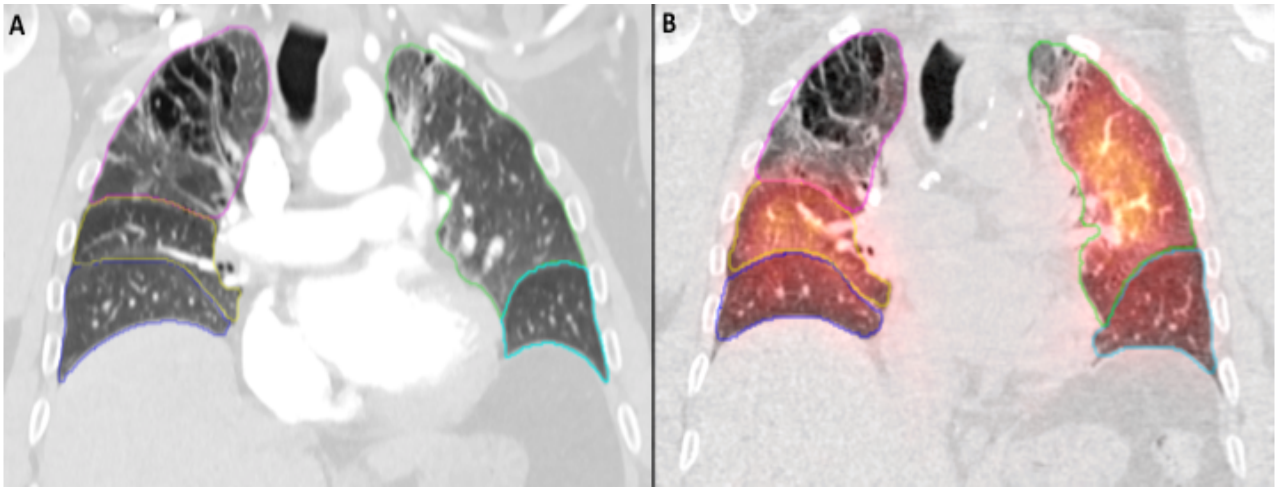

Legend:

Coronal slice showing manual segmentation of lung lobes on (A) DECT and (B) SPECT/CT. Magenta= right superior lobe; yellow= right middle lobe; blue= right inferior lobe; green= left superior lobe; cyan= left inferior lobe.

Figure 2- Coronal slice showing 6 functional lung sub-volumes with increasing iodine content.

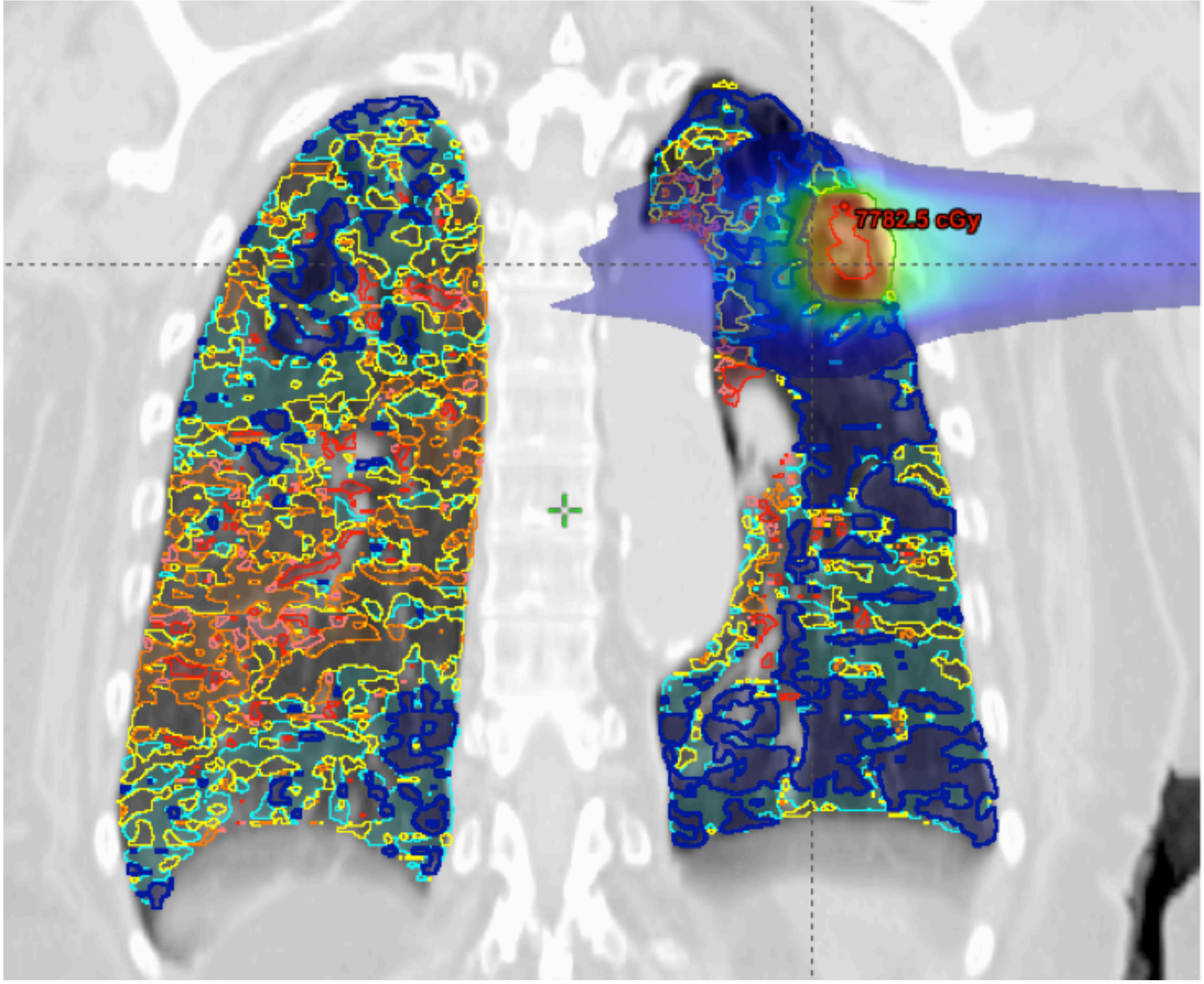

Legend:

Dark blue = least functioning lung; red = most functioning lung; light blue, yellow, orange and pink represent intermediate regions with increasing lung function. PTV (dark green), GTV (red) as well as 5 Gy dose distribution also shown.

Figure 3- DECT-iodine and SPECT/CT maps

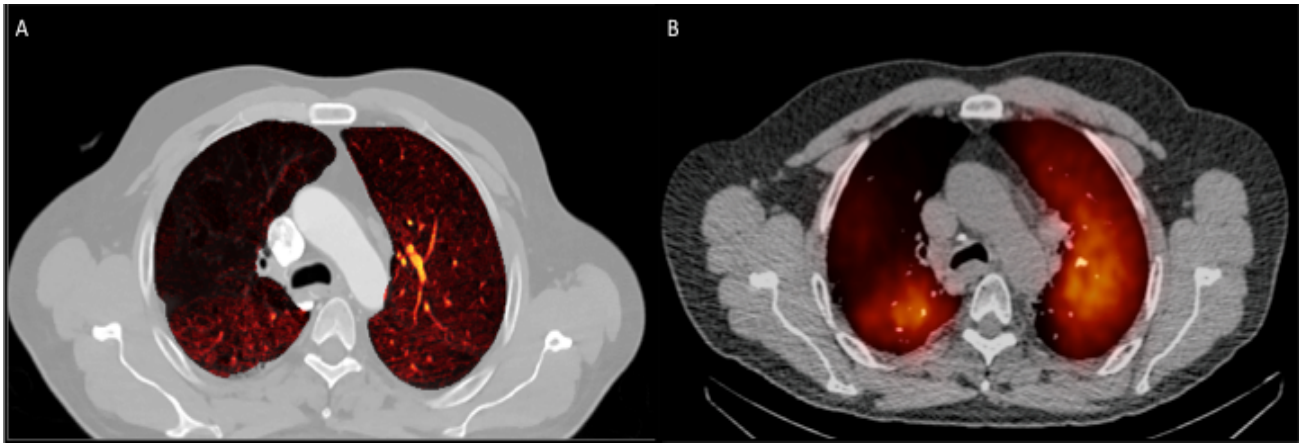

Legend:

Example of a DECT-iodine map (A), and the corresponding SPECT/CT map (B) in a patient with known COPD showing a large perfusion deficit in the superior lobe of the right lung.

Figure 4- Linear correlation between DECT-iodine map and SPECT/CT lobar function

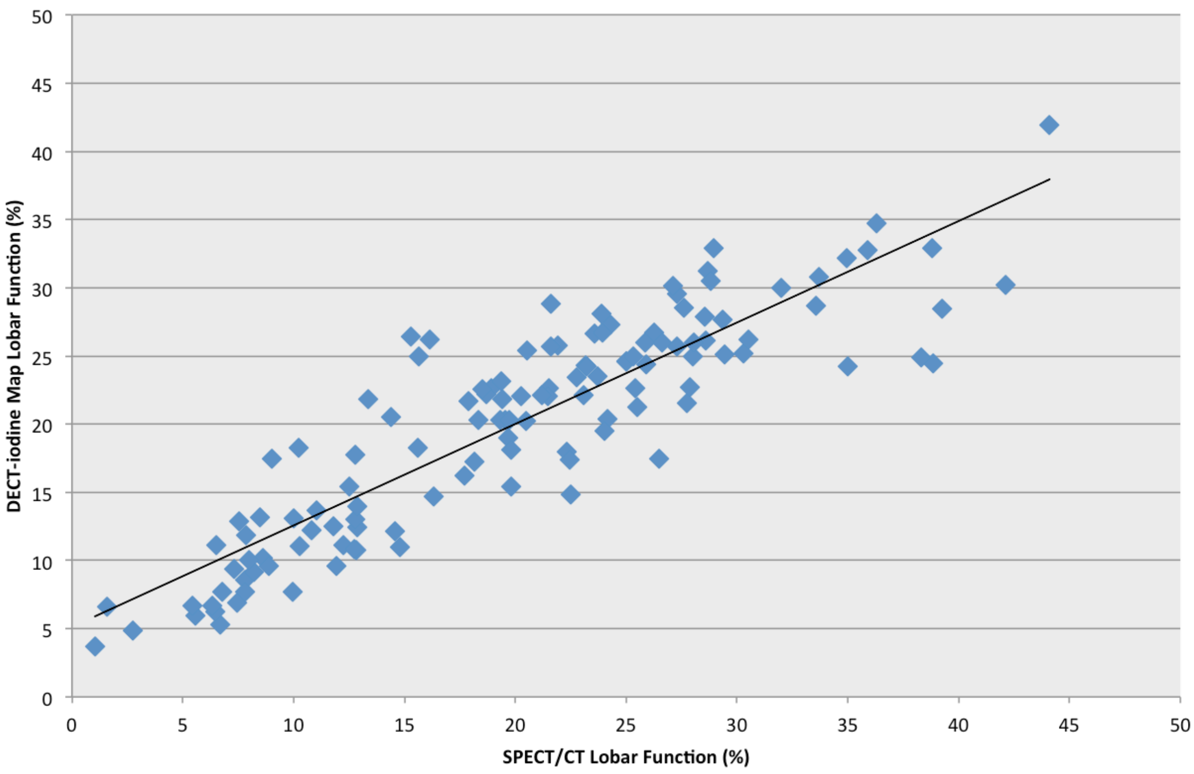

Figure 5- Relative variations in MLD, V5 and V20 between WL vs. FL dosimetries.

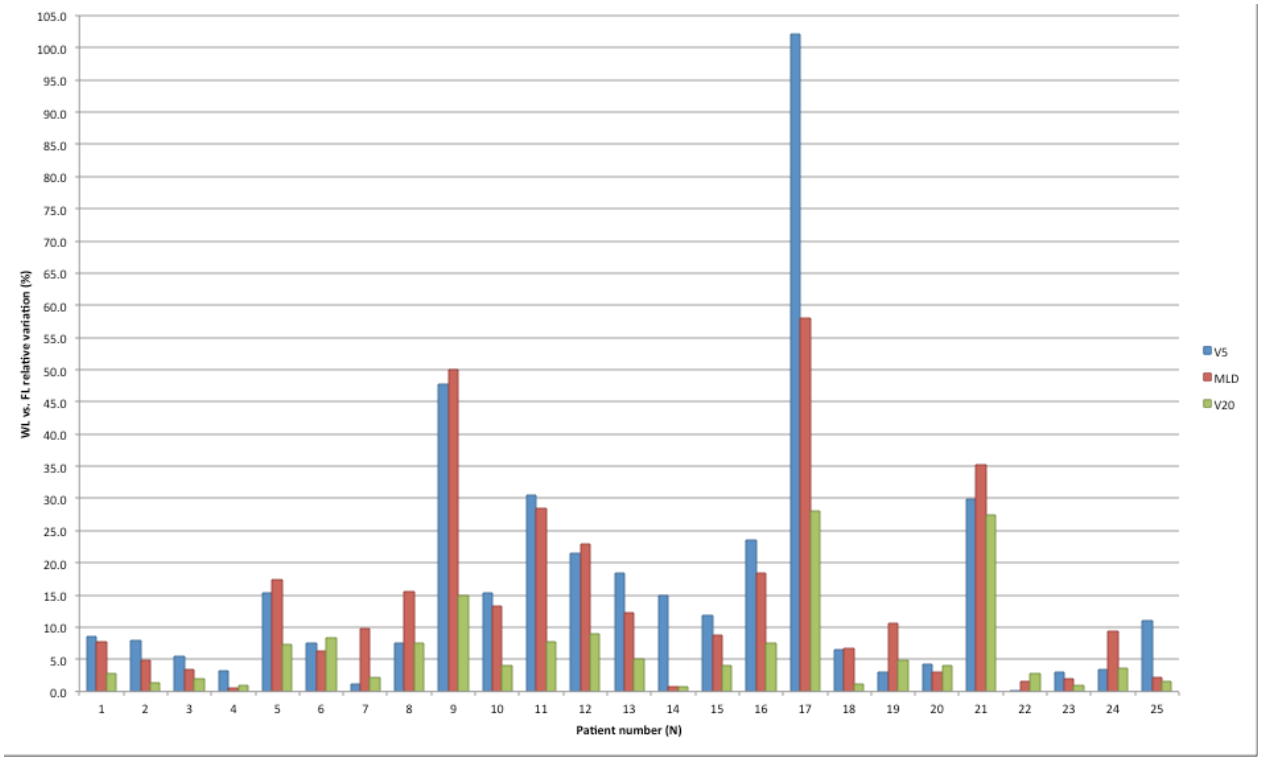

9 DEUXIÈME ARTICLE SCIENTIFIQUE

In a Heartbeat: An Assessment of Dynamic Dose Variation to Cardiac Structures using Dual Source Computed Tomography

Houda Bahig[1,2], Jacques de Guise[2], Toni Vu[1,2], Danis Blais[1], Carl Chartrand-Lefebvre[2,3], Nhu Tram Nguyen[4], Sophie Lavertu[1,2], Jean-Pierre Guay[1,2], David Roberge[1,2]

[1] *Radiation Oncology Department, Centre Hospitalier de l'Université de Montréal, Montreal, QC. Canada*

[2] *Centre de recherche du Centre Hospitalier de l'Université de Montréal, Montreal, QC. Canada*

[3] *Radiology Department, Centre Hospitalier de l'Université de Montréal, Montreal, QC. Canada*

[4] *Radiation Oncology Department, Juravinski Hospital and Cancer Centre, Hamilton, ON. Canada*

Key Words: Left breast, Tangential irradiation, Coronary arteries, Dual-source computed tomography, Left anterior descending artery, Cardiac dose, Cardiac-gated imaging.

Publication:
Int J Radiat Oncol Biol Phys. 2018 Jan 31. pii: S0360-3016(18)30115-9. doi: 10.1016/ j.ijrobp. 2018.01.049. PMID: 29559290

CONTRIBUTIONS: Rédaction du protocole de recherche, coordination et gestion de l'implémentation du protocole de recherche en clinique, récole et analyse des données, interprétation des données, rédaction du manuscrit.

9.1 ABSTRACT

Purpose: To assess radiation dose variation to the left anterior descending artery (LAD), left main coronary artery (LMCA), left ventricle (LV) and whole heart (WH) during the cardiac cycle using dual source computed tomography (DSCT).

Methods: This prospective study included patients with left breast cancer planned for tangential radiotherapy. An electrocardiogram-synchronized contrast-injected DSCT was obtained in treatment position, in deep-inspiration breath-hold (DIBH), using retrospective sequential acquisition. WH, LV, LMCA as well as proximal, middle and distal LAD segments were contoured on each phase of the cardiac cycle. Maximum, minimum and mean Hausdorff distance between each structure and the tangential fields was assessed in ventricular systole vs. diastole. Four-dimensional dose-volume histograms were used to compare systolic vs. diastolic dosimetries.

Results: Ten patients were enrolled. Average maximum, minimum and mean Hausdorff distance variation from systole to diastole was ≤4 mm for LV and LMCA, and ≤3 mm for the heart and LAD segments. WH maximum dose and volume receiving 5Gy were decreased in systole vs. diastole (42.9 Gy vs. 44.5 Gy, p=0.03 and 21.7 cm^3 vs. 27.7 cm^3, p=0.01), but mean dose remained similar throughout the cycle. Maximum and mean dose to distal LAD was 21.2 Gy vs. 26.6 Gy (p=0.005) and 8.6 Gy vs. 13.2 Gy (p=0.006), in systole vs. diastole, respectively. Maximum and mean dose to middle LAD was 18.4 Gy vs. 25.1 Gy (p=0.005) and 8.5 Gy vs. 10.2 Gy, in systole vs. diastole (p=0.005). Maximum dose to LV was lower in systole vs. diastole (21.5 Gy vs. 26.7 Gy, p=0.005).

Conclusion: Beyond DIBH, systolic irradiation would be associated with decrease in dose to LAD, LV and WH. In addition to potential use in planning for cardiac gating, DSCT imaging can be used to help define a planning organ at risk volume for clinically important cardiac sub-structures.

9.2 INTRODUCTION

Although it is well established that adjuvant breast radiotherapy after partial mastectomy improves local control and reduces absolute risk of mortality from breast cancer by 5% at 15 years (89), radiation-induced ischemic heart disease remains a concerning competing cause of mortality in long term survivors (90-93). In a landmark population-based study assessing patients previously irradiated for breast cancer, risk of major coronary event was found to increase linearly with mean dose to the heart (relative risk increased by 7% with each Gray) (90). Risk of cardiac toxicities is thought to be higher in left breast radiotherapy, where tangential fields will commonly include part of the left ventricle (LV) and left anterior descending artery (LAD) (94-96). In the last decade, several cardiac sparing radiotherapy techniques have contributed to significantly reduce cardiac dose and include use of intensity-modulated radiotherapy (97-99) or helical tomotherapy (98, 100), deep inspiration breath-hold techniques (89, 101-104), proton therapy (105, 106) and prone treatment (99, 107, 108),

As per the Quantitative Analyses of Normal Tissue Effects in the Clinic, robust correlations between dose and/or volume parameters and cardiac toxicities are lacking. While current dose constraints only use the whole heart (WH) as organ at risk to spare, studies suggest that the radiosensitivity of the LAD is different from that of the myocardium (109, 110). In left breast irradiation, high rates of middle and distal LAD stenosis, corresponding to the area in close proximity to the tangential fields, have been described (110, 111). In addition, dosimetric studies have reported that fulfillment of WH dose constraints does not exclude hotspots above 50 Gy in the middle and distal LAD (112). In this context, many agree that the LAD should be considered a separate organ at risk from the WH and that there is an urgent need to better understand radiation dose-effect to the LAD.

Recent studies have underlined the importance of improved LAD segmentation to increase the consistency of dose reporting (113, 114). Proper LAD dose assessment remains limited by its inconsistent delineation, which is affected by significant cardiac and respiratory motion artefacts (114, 115). Using routine free-breathing treatment planning computed tomography (CT), the LAD is reliably visualised in only a third of patients, regardless of the use of iodinated contrast (113, 116), suggesting that advanced imaging is needed to increase LAD delineation accuracy (114). Dual source computed tomography (DSCT) is an advanced imaging technique allowing prospective electrocardiogram (ECG)-gated imaging of the heart during cardiac contraction; assessment of extent of motion and precise visualisation of the coronary artery segments, free from motion artifacts, can therefore be achieved (20, 27). While the extent of displacement arising from intrinsic cardiac contraction has previously been evaluated using cardiac-gated magnetic resonance imaging (117) and coronary angiography with retrospective ECG gating (118), the impact on dose to cardiac structures was not reported. In this study, we use cardiac DSCT at time of treatment planning, in treatment position, for optimal visualisation of the WH, LV and the LMCA-LAD throughout the cardiac cycle in patients irradiated for left breast cancer. The purpose of the study was to assess dose variation to LMCA-LAD, left ventricle (LV) and heart during the cardiac cycle relative to tangential fields, using DSCT technology.

9.3 MATERIAL AND METHODS

Study population

Female patients planned for adjuvant whole breast irradiation at our institution were prospectively enrolled in this study from June 2015 to June 2016. Eligibility criteria included: (1) pathological confirmation of left breast invasive cancer or carcinoma in-situ; (2) status post partial mastectomy; (3) Eastern Cooperative Oncology Group performance status 0-2; (4) planned for adjuvant tangential whole breast radiotherapy. All patients had pre-treatment baseline ECG to confirm sinus rhythm. Patients with contra-indications to iodine injection were excluded. The protocol and patient consent form were reviewed and approved by our institutional ethics committee.

Radiotherapy planning and cardiac DSCT

All patients underwent a standard non-contrast planning CT immediately followed by a cardiac DSCT (SOMATOM Definition Flash; Siemens Healthineers, Erlangen, Germany). Both planning CT and cardiac DSCT were acquired in supine position, with arms up, using a breast board and a vaclock for immobilization purposes. Contrast-injected cardiac DSCT involved a iopamidol bolus (370 mg iodine / mL, Isovue 370; Bracco Imaging, Milan, Italy) injected at a rate of 4 ml/sec using the following protocol: 60 ml of contrast over 15 seconds followed by injection of a blend of 10 ml of contrast material along with 10 ml of sodium chloride (NaCl) 0.9% over 5 seconds, followed by 40 ml of NaCl 0.9% over 10 seconds. Cardiac DSCT was acquired in DIBH and synchronized to the patient's electrocardiogram. A retrospective sequential acquisition over 8 phases of the R-R interval of the electrocardiogram (phases 20%, 30%, 40%, 50%, 60%, 70%, 80% and 90%) was triggered after contrast bolus tracking at the level of the ascending aorta. The R-R interval corresponds to the time between the R wave of one heartbeat and the R wave of the preceding heartbeat and represents a complete cardiac cycle. Maximum systole is expected between phases 20 % and 30%, and maximum diastole is expected between phases 70 and 80%. DIBH was reproduced using the Abches system (APEX Medical, Tokyo, Japan), a self-control respiratory monitoring device that provides breathing feedback to patients (119). DSCT acquisition parameters were as follows: slice thickness of 2 mm, rotation time of 0.28 seconds, collimation of 128 x 0.6 mm and X-ray tube potentials of 120kV, matrix 512 × 512 pixels, field of view 33 cm and voxel size of 0.6 x 0.6 x2 mm^3. Images were reconstructed using medium soft tissue convolution kernel (I36f) and level 3 sinogram affirmed iterative reconstruction (120). No beta-blockers or nitrates were used prior to scanning.

As per our institution protocol, only patients with > 10 cm^3 of heart volume in the tangential fields were treated in DIBH. However, for the purpose of the study, all radiation treatment plans were calculated in DIBH using a prescription dose of 50 Gy in 25 fractions, regardless of heart volume in the tangential fields. As the field of view of the cardiac scan is limited to 35 cm, the missing anatomy was filled in with the planning CT (the image sets were registered based on CT coordinates). The CT thus created by joining the DIBH-planning CT and cardiac DSCT was used for dose calculation. The planning CTs were acquired in DIBH > 10 cm^3 of the heart volume would have been within the tangents; the other planning scans were acquired in free breathing. Dose calculation was performed on the 50% phase of the cardiac DSCT. All cases were planned using two conformal 6 MV tangential fields and multi-leaf collimator-optimized field-in-field to avoid hotspots exceeding 110 %. Analytical Anisotropic Algorithm on Eclipse treatment planning system (Varian Medical Systems, Palo Alto, CA) was used for dose calculation. Tumor bed boosts were excluded from the current analysis.

Cardiac structures delineation and dose assessment

For each patient, dose distribution, along with the 8 phases of the cardiac DSCT were transferred to a MIM Maestro workstation (MIM Software Inc., Cleveland, OH). The heart, left ventricle (LV), left main coronary artery (LMCA), proximal LAD, middle LAD and distal LAD were contoured on all 8 phases of the cardiac CT, using previously described guidelines (121), a window level of 50 and a window width of 500 Hounsfield units. **Figure 6** shows an example of multiphase contouring of the WH, LV and distal LAD shown on one of 8 cardiac DSCT phase. The proximal LAD was contoured from the bifurcation of the LMCA to the origin of the first diagonal branch (D1); the middle LAD was contoured from the origin of the first diagonal branch to proximal half of the distance between D1 origin and the heart apex; the distal segment included the distal half of the distance between D1 origin and heart apex (122-124). The 50% isodose line, typically representative of the field position in tangential field setup, was converted into an RT structure for Hausdorff distance calculatiom. Maximum, minimum and mean Hausdorff distance between each structure and the 50% isodose line of the tangential fields was calculated for the extreme phases of ventricular systole and diastole. Using 4D dose-volume histogram (DVH), maximum and mean dose to LMCA-LAD, WH and LV in maximum ventricular systole, maximum ventricular diastole, as well as in each phase of the cardiac cycle were assessed. For WH and LV, volume receiving 5 Gy (V5), and V20 were also compared. Cumulative dose to WH, LV, middle LAD and distal LAD over the entire cardiac cycle (using the 8 phases) was calculated to obtain an estimation of overall cardiac structure dose in DIBH. Wilcoxon signed rank test for paired samples was used to compare doses to cardiac structures in ventricular systole vs. diastole, as well an in ventricular systole vs. cumulated dose of entire cardiac cycle, with p values $p<0.05$ considered statistically significant, from two-sided tests. SPSS 24 (IBM, Armonk, NY) was used for statistical analysis.

9.4 RESULTS

Patients and cardiac DSCT characteristics

Ten female patients with left breast adjuvant radiotherapy were enrolled. This included 2 patients with ductal carcinoma in situ, and 8 patients with T1a-cN0 disease as per American Joint Committee on Cancer 7th Edition. Median age was 60 years (56-71). Baseline ECG showed sinus rhythm in all patients. One patient was taking an angiotensin II receptor blocker for treatment of hypertension; no other patients were on antiarrhythmic medications. As per DSCT characteristics, mean scan heart rate was 74 beats per minute (bpm) (67-83 bpm). Mean volume CT dose index was 60.7 mGy (42.3-73.0 mGy), mean dose length product was 1072 mGy-cm (729-1554 mGy-cm), and effective dose was 15 mSv (10-22 mSv). Coronary artery opacification was adequate in all cases, without significant artefacts.

Hausdorff distance variation between cardiac structures and tangential fields

Hausdorff distances as well as volume variation with cardiac contraction are presented in **Table 3.** WH and LV had a mean volume expansion of 57.3 cm^3 (34.2-99.7 cm^3) and 50.4 cm^3 (28.0-79.6 cm^3) from systole to diastole; the coronary arteries did not present any statistical difference in volume with cardiac contraction. As can be expected, the maximum, minimum and mean distances between the tangential fields and WH, LV and all three segments of the LAD were decreased in diastole compared to systole; however, maximum, minimum and mean distances between the tangential fields and the LMCA was increased in diastole. For all cardiac structures, minimum and mean Hausdorff distance variations were ≤3 mm and ≤4 mm, respectively.

Dose variations for cardiac structures along the cardiac cycle

Table 4 summarizes dose variation to WH, LV, LAD segments and LMCA between extreme systole vs. extreme diastole, as well as between extreme systole vs. cumulated dose over the entire cardiac cycle. **Figure 7** shows an example of 4D dose volume histogram showing systolic and diastolic dosimetries. Maximum dose and V5 to WH were lower in systole compared to diastole (42.9 Gy vs. 44.5 Gy, p=0.03 and 21.7 cm^3 vs. 27.7 cm^3, p=0.01). Mean dose to WH was not statistically different with cardiac contraction. Maximum dose to LV was lower in systole vs. diastole (21.5 Gy vs. 26.7 Gy, p = 0.002). Maximum and mean dose to distal LAD was 21.2 Gy vs. 26.6 Gy (p=0.005) and 8.6 Gy vs. 13.2 Gy (p=0.006), in systole vs. diastole, respectively. Maximum and mean dose to middle LAD was 18.4 Gy vs. 25.1 Gy (p=0.005) and 8.5 Gy vs. 10.2 Gy, in systole vs. diastole (p=0.005). There was no difference in dose to proximal LAD. Although there was a statistically significant difference for mean dose to LMCA, the difference was small and unlikely to be clinically significant. When comparing extreme systole to cumulated dose over the entire cardiac cycle, maximum dose (p=0.04) and V5 (p=0.02) to WH, maximum LV dose (p=0.005), maximum (p=0.04) and mean dose (p=0.01) to distal LAD and maximum (p=0.007) and mean dose (p=0.01) to middle

LAD remained statistically lower (**Table 4**). **Table 5** presents dose to WH, LV, middle and distal LAD through phases 10% to 90% of the cardiac cycle. Systolic phases are situated between 20-40%, suggesting that systolic cardiac gating could have a potential efficiency of approximately 0.25.

Linear correlations between mean Hausdorff distance (cardiac structure to tangential fields) and amplitude of dose variation from systole to diastole showed weak negative correlations, with largest dose variation in patients with cardiac structures approaching the field edge (**Figure 8**).

9.5 DISCUSSION

To our knowledge, this is the first study reporting the use of cardiac DSCT in radiotherapy treatment planning for assessment of cardiac motion and precise delineation of the LAD-LMCA structures. In addition, although the extent of LAD displacement with cardiac contraction was previously reported, this is also the first study describing the dosimetric impact of cardiac motion in patients with left tangential breast irradiation. Cardiac DSCT has the advantage of providing multiphase imaging throughout the cardiac cycle with high temporal resolution (125), therefore suppressing motion-induced blurring and improving visualisation of small tortuous vessels. Under breath-hold conditions, use of cardiac DSCT allowed for assessment of dose variation from ventricular systole to diastole and estimation of cumulated dose over the entire cardiac cycle in patients treated for left breast cancer. This study represents an important step toward improved understanding of radiation dose effect to the LAD and, although tangential irradiation was chosen as a proof of concept, this method can be applied to loco-regional breast irradiation and, more generally, to thoracic radiotherapy.

Ventricular systole was associated with a 5-7 Gy decrease in maximum dose to the middle LAD, distal LAD and LV, as well as 2 and 4 Gy decrease in mean dose to the middle and distal LAD, respectively. Although V5 and maximum dose to the WH was lower in systole, mean dose to WH was generally unchanged throughout the cardiac cycle. Interestingly, the distance between the LMCA and the tangential fields was increased in diastole, a finding that is consistent with previously described counter-clockwise rotational torque occurring at the apex of the heart (counter-clockwise direction) vs. at the base (clockwise) with myocardial contraction (126). This resulted in mild LMCA dose increment in systole that is clinically insignificant in the context of tangential fields; however this difference is likely to be more pronounced in loco-regional radiotherapy involving the internal mammary chain. Using cardiac-gated magnetic resonance imaging, White et al. assessed displacement of a region of interest comprising the LAD; their group reported an average displacement within 1 mm in the 3 axes (117). Closer to our study, Wang et al. (118) assessed LAD and heart displacements with cardiac contraction relative to tangential fields in 20 patients undergoing left breast cancer radiotherapy in DIBH. Using CT-based coronary angiography with retrospective ECG-gating, negligible heart displacement near the tangential fields was reported but mean LAD displacement was 2 mm, consistent with our findings. In addition, in up 30% of patients, LAD displacement exceeded 5 mm (118).

The currently supported mechanisms of long-term radiation-induced cardiac toxicity involve on one hand microangiopathy leading to focal myocardial fibrosis and, on the other hand, macroangiopathy of the coronary arteries leading to accelerated atherosclerosis (94, 127).

Radiation dose effects to the heart remain however inconsistent throughout the studies (128). This is partly explained by the challenging delineation of various cardiac sub-regions (the coronaries, in particular) with standard CT imaging, which precludes consistent dose reporting. The LAD is a particularly crucial structure supplying beyond 40% of the blood flow to the myocardial muscle and is often included in the tangential fields of left breast irradiation (129). In a Swedish cohort of 199 patients with previous breast irradiation, patients with left breast cancer were at higher risk of middle and distal LAD stenosis, consistent with our finding of highest doses to these specific segments (110). Similarly, Correa et al. (111) reported up to 60% rate of cardiac abnormalities on cardiac stress test at a median time of 12 years post conventional left breast radiotherapy; 70% of these abnormalities were within the LAD territory. While current dose constraints in the clinic focus on whole heart, high doses in the middle and distal segments of the LAD strongly support the need to consider the LAD as a separate organ at risk and to determine safe threshold dose (130). This is particularly important given that it has been shown that fulfillment of whole heart dose constraints does not exclude high hotspots to the LAD (95, 112, 114).

The small and tortuous anatomy of the coronary vessels as well as the artefacts caused by both respiratory and cardiac motion make delineation of the LAD-LMCA challenging, with LAD being visualised in only 30% of patients with current planning CT technique (113, 116). Yet consistency in coronary arteries delineation is essential to the development of normal tissue complication probability models and development of LAD-sparing treatment planning techniques. To address the need for consistent dose reporting, Feng et al. (121) developed a contouring heart atlas of various cardiac sub-regions, including the coronaries, in breath-hold condition. Although the lack of cardiac gating for the development of this atlas may not have significantly affected the larger structures, the magnitude of error for the smaller structures such as the coronaries may be more important. While respiratory motion can be accounted for using DIBH, gating or 4D-CT motion assessment, cardiac contraction remains a challenge and requires advanced imaging technique. Using multiphasic cardiac DSCT, an internal LAD volume, including the position of the LAD in the various positions of the cardiac cycle, can easily be obtained and used for plan optimisation. Alternatively, the availability of cardiac position in extreme diastole can provide worst-case scenario for determination of safe proximity of the treatment field edge. Considering the observed dose sparing of cardiac structures in systole, future strategies for the development of cardiac-gated radiotherapy, in which the multiphase DSCT would help select an optimal gating window, deserves investigation.

In this study, dose variation with cardiac contraction was assessed assuming perfect reproducibility of DIBH position between the planning CT and daily repositioning during treatment. Previous studies have however reported large inter-fraction set-up errors in reproducibility of DIBH (131, 132), but breathing feedback, as used in this study, was shown to significantly decrease this variability (133). In addition, our results suggest that patients with smaller distance between cardiac structures and tangential fields may have the largest benefit from systolic irradiation; however, only 4 patients in this study presented > 10 cm^3 of heart volume in the tangential fields and were selected for actual DIBH treatment. The dose variation during the cardiac cycle in our patients may therefore be underestimated compared to patients with closer proximity of the heart and tangential fields. Importantly, dose variations observed could be influenced by inter-observer contouring variability. In a recent study by Wennstig et al.(130) evaluating inter-observer variation for delineation of LMCA-LAD arteries on planning CT scans, good reliability was reported between radiation oncologists, with intra-class correlation coefficient varying between 0.76 and 0.98, suggesting that dose variations in these structures were mostly related to inter-patient variation rather than variation between radiation oncologists contouring. In a study by Duane et al.(134) assessing inter-observer variation for cardiac structures delineation, inter-observer separation was reported to be between 1.5–2.2 mm for the left ventricle and between 1.3–5.1 mm for the coronary arteries. We feel that such variations would be less in our DSCTs which provide better visualization of cardiac structures. For consistency of delineation we used the validated heart atlas by Feng et al.(121). We also have no reason to believe that such variations would have systematically influenced our results, as our results show a consistent sparing of the LAD in systole for all 10 patients. An additional limitation is the increased radiation dose associated with cardiac DSCT; however, with available dose reduction techniques, ECG-gated cardiac CT patient dose exposure has significantly decreased in recent years (135, 136). Moreover, in the context of clinical application for treatment optimisation, this is to be weighted against the benefit of improved LAD-sparing. In the context of this feasibility study, we opted for multiphase acquisition throughout the cardiac cycle, but one way to decrease ionising radiation would be through acquisition of only the most extreme phases of systole and diastole. While we found that maximum dose to LAD, LV and WH as well as mean dose to LAD were significantly reduced in systole, the potential clinical impact of such a reduction, as well as the feasibility of future application in cardiac gated irradiation, notably in the context of flattening filter free beams, remain to be investigated. Finally, the clinical application of this method is limited by the restricted availability of ECG-gated CT. However, in recent years, the growing interest for dual energy CT technology in radiotherapy planning (137) has led to the acquisition of ECG-gated/dual-energy CT technology in several institutions. Results from our study suggests that systolic cardiac gating could have a potential efficiency of approximately 0.25, but selection of gating window should be individualized, weighting patient-specific dose sparing vs. treatment time.

9.6 CONCLUSION

DSCT allows for high temporal resolution cardiac imaging that can be explored in radiotherapy planning for assessment of cardiac motion and improved delineation of coronary arteries. Beyond DIBH, systolic irradiation would be associated with dose sparing of the middle and distal LAD, LV and WH. Determination of precise internal organ at risk volume through this technique can: (1) improve consistency of dose reporting and therefore improve understanding thresholds for development of cardiac toxicities and (2) be used to provides useful information on safe proximity to the treatment field edge by providing worst case scenario dose. The potential clinical impact of cardiac dose reduction in systole, as well as the feasibility of cardiac gated irradiation, need to be further investigated.

9.7 TABLES ET FIGURES

Table 3- Variation of cardiac structures volume along the cardiac cycle and Hausdorff between cardiac structures and tangential fields

	Systole		**Diastole**		**Difference**	
	Mean	**Range**	**Mean**	**Range**	**Mean**	**Range**
WH						
Volume (cm^3)	687.4	538.4-826.3	744.7	646.4-907.6	57.3	34.2-99.7
Max Hausdorff D (cm)	13.2	10.9-16.8	12.9	10.8-16.5	**0.3**	**0.1-0.5**
Min Hausdorff D (cm)	0.1	0.0-1.1	0.1	0.0-0.9	**0.0**	**0.0-0.3**
Mean Hausdorff D (cm)	5.4	4.8-6.2	5.3	4.0-6.7	**0.1**	**0.0-0.2**
LV						
Volume (cm^3)	164.2	129.0-268.0	214.6	169.0-298.0	50.4	28.0-79.6
Max Hausdorff D (cm)	13.1	10.3-16.9	12.7	9.8-16.5	**0.4**	**0.1-0.6**
Min Hausdorff D (cm)	0.3	0.0-1.5	0.2	0.0-1.3	**0.1**	**0.0-0.2**
Mean Hausdorff D (cm)	5.9	5.1-7.4	5.7	4.8-7.1	**0.2**	**0.1-0.4**
LAD$_{Prox}$						
Volume (cm^3)	0.4	0.2-0.8	0.4	0.2-0.9	0.0	0.0-0.2
Max Hausdorff D (cm)	15.0	12.7-19.3	14.8	12.7-19.8	**0.2**	**0.0-0.7**
Min Hausdorff D (cm)	2.0	0.3-3.8	1.7	0.1-3.3	**0.3**	**0.0-0.9**
Mean Hausdorff D (cm)	8.7	7.2-9.9	8.5	7.0-9.8	**0.2**	**0.0-0.5**
LAD$_{,Mid}$						
Volume (cm^3)	0.4	0.2-0.6	0.5	0.3-0.7	0.1	0.0-0.2
Max Hausdorff D (cm)	15.0	12.8-19.4	14.7	11.8-19.4	**0.3**	**0.0-1.0**
Min Hausdorff D (cm)	0.5	0.0-1.8	0.4	0.0-1.6	**0.1**	**0.0-0.3**
Mean Hausdorff D (cm)	7.3	6.3-8.9	7.2	6.2-8.8	**0.1**	**0.0-0.3**
LAD$_{Dist}$						
Volume (cm^3)	0.5	0.3-0.9	0.5	0.3-0.9	0.0	0.0-0.2
Max Hausdorff D (cm)	17.3	14.0-22.0	17.0	13.8-21.8	**0.3**	**0.0-0.7**
Min Hausdorff D (cm)	0.4	0.0-1.8	0.3	0.0-1.6	**0.1**	**0.0-0.3**
Mean Hausdorff D (cm)	7.8	6.7-9.4	7.7	6.5-9.3	**0.1**	**0.0-0.3**
LMCA						
Volume (cm^3)	0.2	0.1-0.4	0.2	0.1-0.4	0.0	0.0-0.1
Max Hausdorff D (cm)	15.8	13.5-20.3	16.1	9.1-13.0	**-0.3**	**0.0-(-0.8)**
Min Hausdorff D (cm)	4.8	3.3-6.8	5.1	4.0-7.4	**-0.3**	**0.1-(-0.7)**
Mean Hausdorff D (cm)	10.7	9.1-13.0	11.1	9.5-13.8	**-0.4**	**0.0-(-0.8)**

WH= Whole heart; LV= Left ventricle; LAD$_{dist}$=distal left anterior descending artery; LAD$_{mid}$= middle left anterior descending artery LAD$_{prox}$= proximal left anterior descending artery; D= distance.

Table 4- Dose variation for WH, LV, and LMCA-LAD with along the cardiac cycle

	Systole		Diastole			Cumulated dose (8 phases)		
	Mean	*Range*	*Mean*	*Range*	*p*	*Mean*	*Range*	*p*
WH								
Max; Gy	**42.9**	**7.0-52.4**	**44.5**	**7.9-52.6**	**0.03**	**43.9**	**7.4-52.0**	**0.04**
Mean; Gy	1.4	0.7-2.4	1.5	0.7-2.9	NS	1.5	0.7-2.9	NS
V20; cm^3 (%)	6.3 (1%)	0.0-23.7 (0-4%)	8.3 (1%)	0.0-27.0 (0-4%)	NS	7.8 (1%)	0-25.9 (0-4%)	NS
V5; cm^3 (%)	**21.7 (3%)**	**2.0-59.1 (0-8%)**	**27.7 (5%)**	**2.0-63.0 (0-8%)**	**0.01**	**26.0 (4%)**	**2.0-56.2 (0-8%)**	**0.02**
LV								
Max; Gy	**21.5**	**6.1-45.7**	**26.7**	**5.1-47.1**	**0.002**	**24.8**	**4.9-45.8**	**0.005**
Mean; Gy	1.6	1.0-3.2	1.8	1.0-3.2	NS	1.8	1-3.2	NS
V20; cm^3 (%)	0.6 (0.4%)	0.0-3.7 (0-3%)	1.3 (1%)	0.0-5.7 (0-3%)	NS	1.0 (1%)	0.0-4.4 (0-3%)	NS
V5; cm^3 (%)	4.2 (2.8%)	0.0-13.0 (0-6%)	7.4 (4%)	0.0-22.1 (0-11%)	NS	6.5 (4%)	0.0-16.0 (0-10%)	NS
LAD$_{\text{Prox}}$								
Max; Gy	4.6	1.4-16.6	4.6	1.7-14.0	NS	4.6	1.6-14.8	NS
Mean; Gy	2.1	1.1-4.3	2	1.0-5.5	NS	2	1.0-5.1	NS
LAD$_{\text{Mid}}$								
Max; Gy	**18.4**	**2.1-45.8**	**25.1**	**2.4-46.5**	**0.005**	**22.9**	**2.2-46.1**	**0.007**
Mean; Gy	**8.5**	**1.7-32.9**	**10.2**	**1.9-32.7**	**0.005**	**9.9**	**1.8-31.4**	**0.01**
LAD$_{\text{Dist}}$								
Max; Gy	**21.2**	**2.9-47.8**	**26.6**	**3.1-49.9**	**0.005**	**24.5**	**2.9-48.0**	**0.04**
Mean; Gy	**8.6**	**1.8-34.3**	**13.2**	**2.0-36.6**	**0.006**	**12**	**2.1-36.0**	**0.01**
LMCA								
Max; Gy	1.1	0.8-1.6	1	0.8-1.3	NS	1	0.8-1.4	NS
Mean; Gy	0.9	0.6-1.2	0.8	0.6-1.0	0.03	0.8	0.6-1.0	NS

WH= Whole heart; LV= Left ventricle; LAD$_{dist}$=distal left anterior descending artery; LAD$_{mid}$= middle left anterior descending artery LAD$_{prox}$= proximal left anterior descending artery; D= distance.

Table 5- Mean dose to WH, LV, middle and distal LAD in each phase of the cardiac cycle

		Cardiac cycle phase							
		20%	**30%**	**40%**	**50%**	**60%**	**70%**	**80%**	**90%**	**Cumulated dose**
WH	**Max (Gy)**	42.9	42.9	43.9	44.0	44.3	44.3	44.5	44.5	43.9
	V5 (cc)	21.8	21.7	22.9	25.2	26.4	26.5	26.7	26.7	24.8
LV	**Max (Gy)**	21.5	21.5	23.8	25.4	26.1	26.5	26.7	26.7	24.8
LAD-M	**Max (Gy)**	18.4	18.9	22.2	23.8	24.6	25.0	25.0	25.1	22.9
	Mean (Gy)	8.5	9.5	9.9	10.1	10.2	10.2	10.2	10.2	9.9
LAD-D	**Max (Gy)**	21.2	21.2	24.6	25.0	25.1	25.5	26.5	26.6	24.5
	Mean (Gy)	10.1	8.6	12.3	12.5	13.0	13.1	13.1	13.2	12.0

Figure 6- Contours of the WH, LV and distal LAD

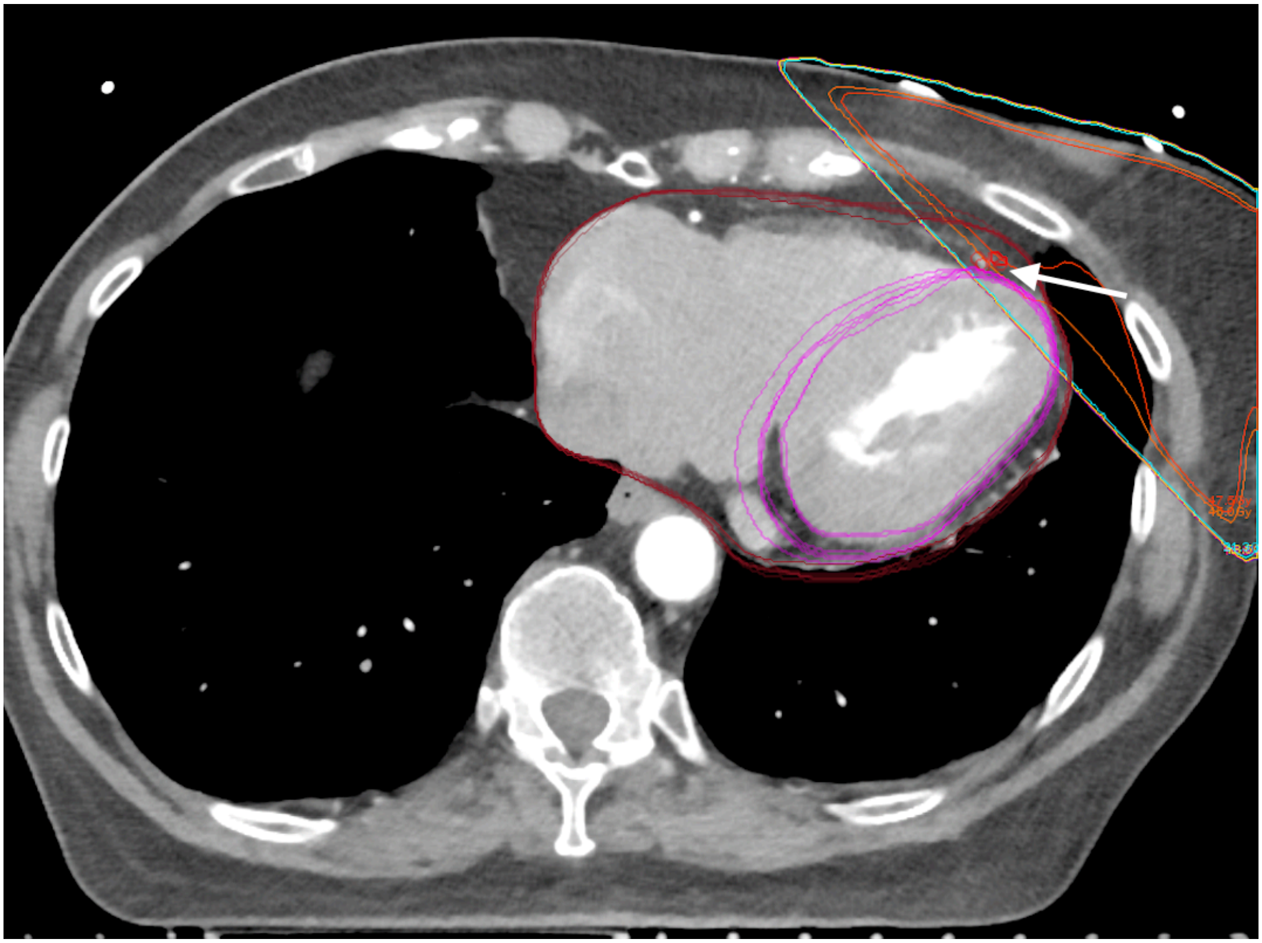

Legend:

Contours of the WH (dark red), LV (pink) and distal LAD (bright red; white arrow) on an axial cardiac DSCT slice, at 80 % of the R-R interval; dose distribution from tangential fields is also displayed (bright red= 95% isodose line; orange= 90% isodose line).

Figure 7 - Example of 4D dose volume histogram showing maximum systolic and diastolic doses to LAD segments

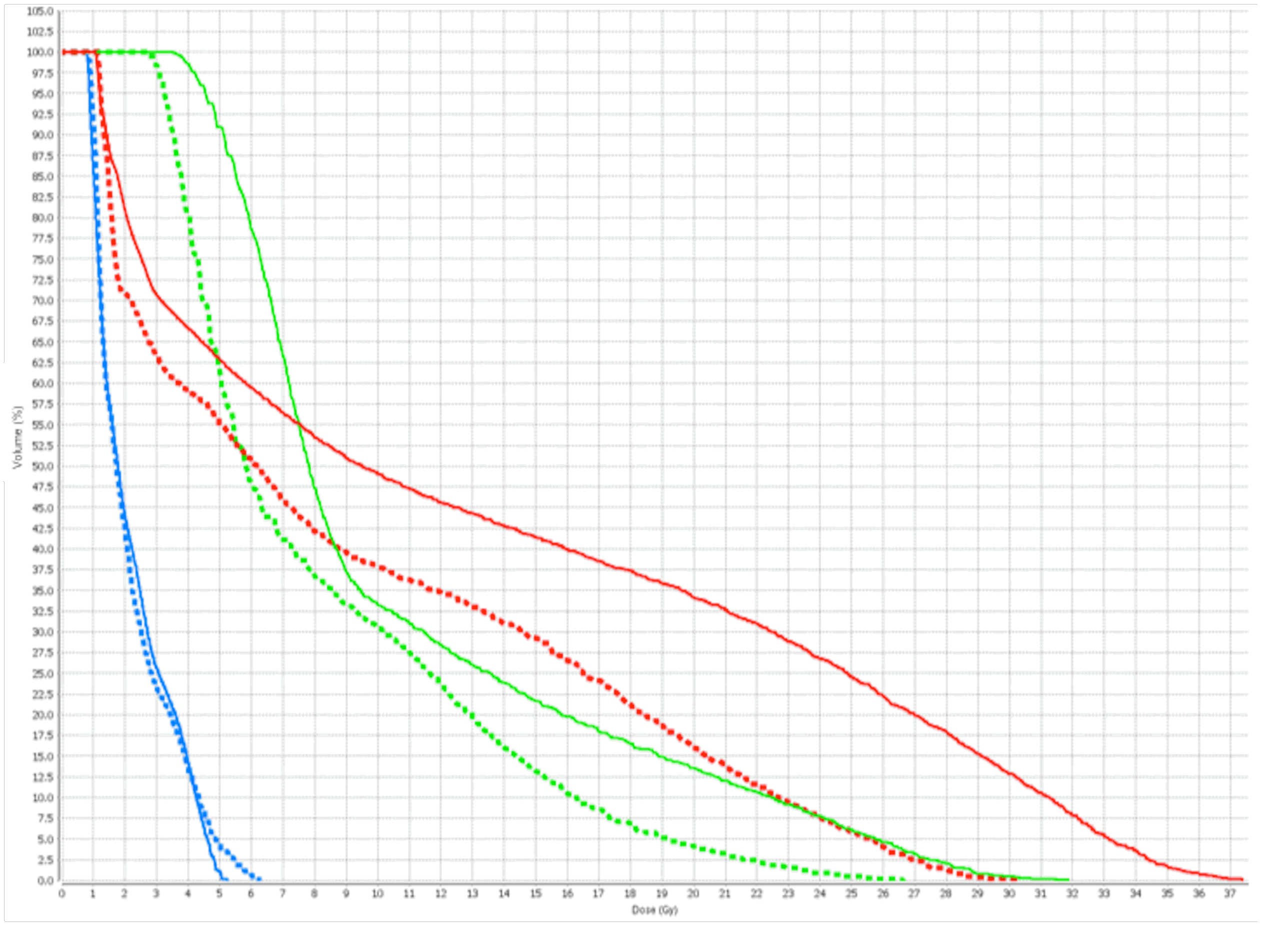

Legend:

Red= distal LAD; green= middle LAD, blue = proximal LAD. Solid line = diastole; dotted line = systole

Figure 8- Correlation between mean Hausdorff distance to tangential fields and dose variation with cardiac cycle for WH, LV, middle and distal LAD.

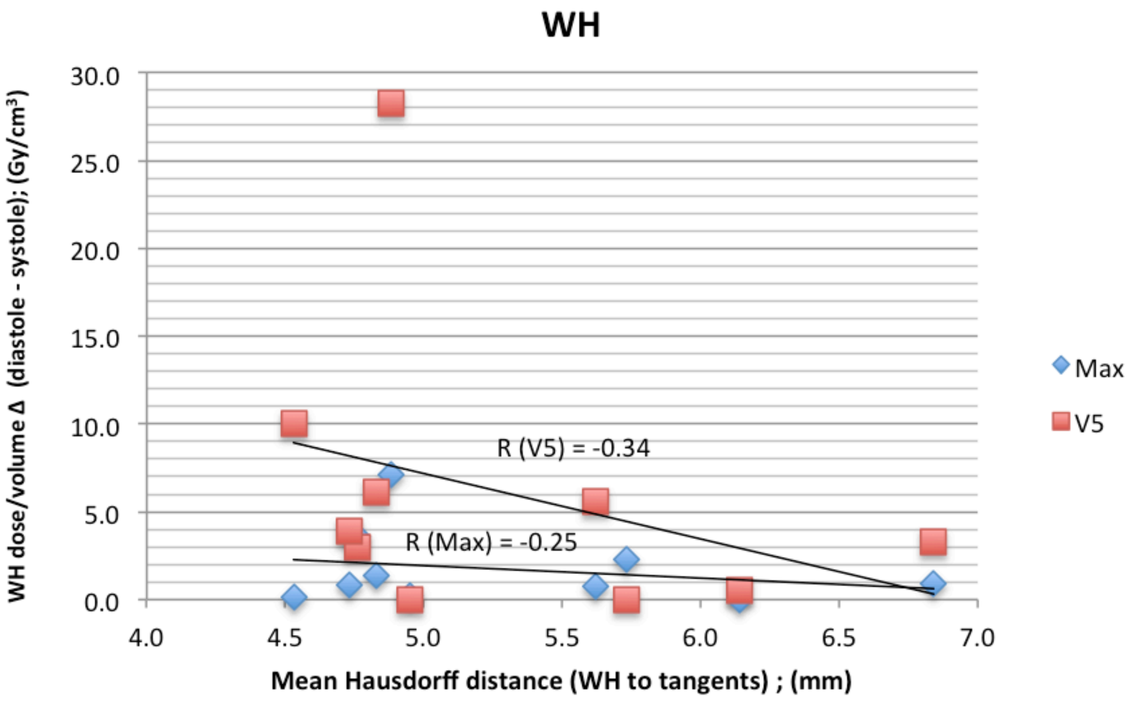

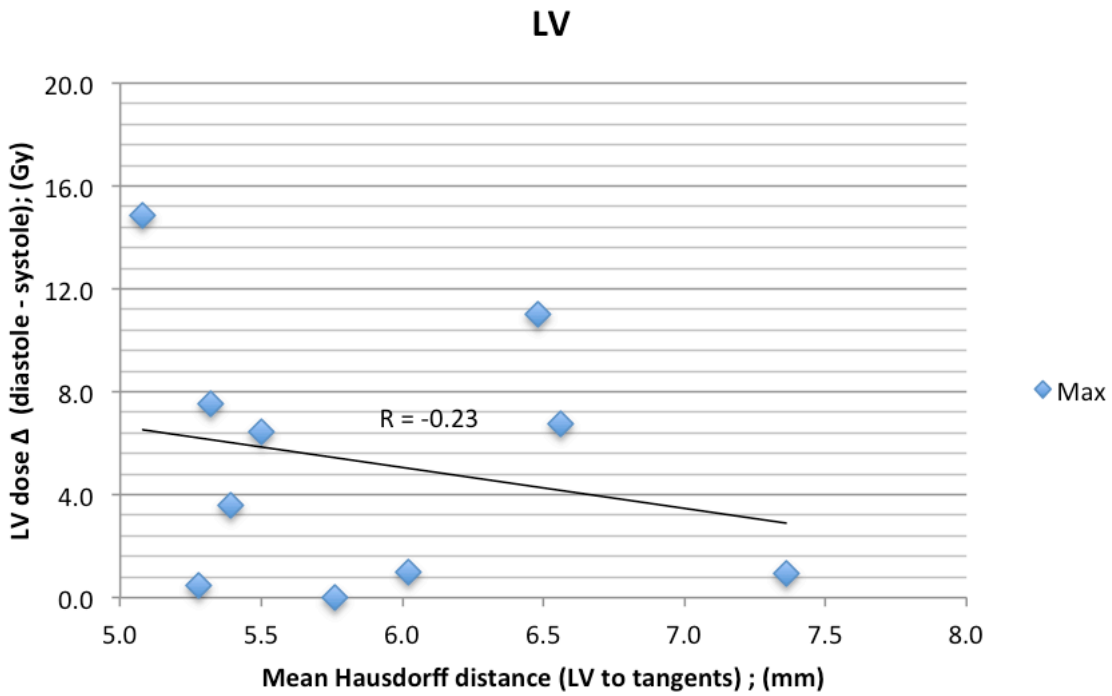

Figure 8 ***(Continued)*** Correlation between mean Hausdorff distance to tangential fields and dose variation with cardiac cycle for WH, LV, middle and distal LAD.

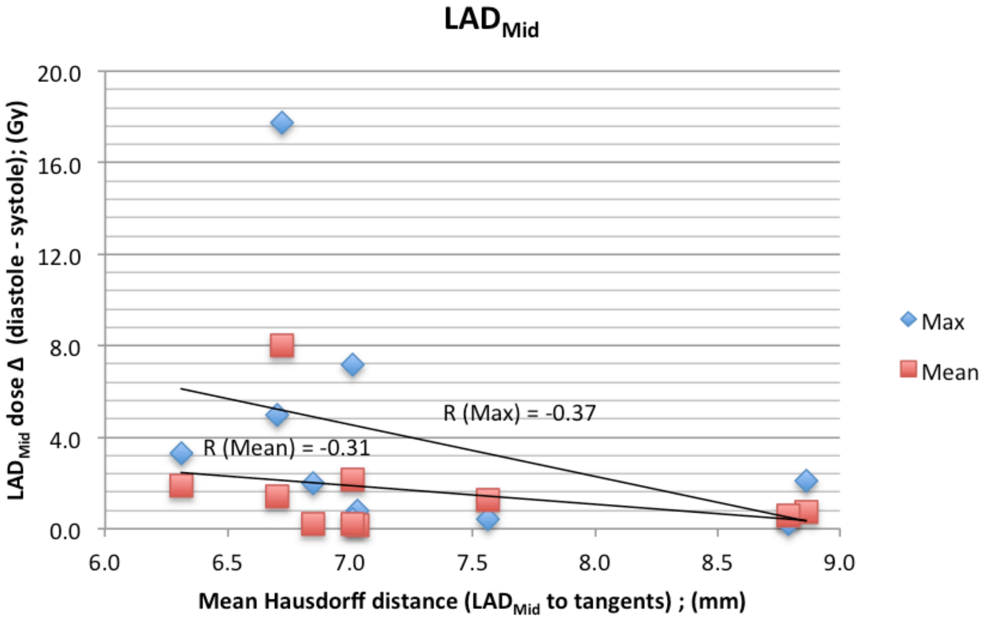

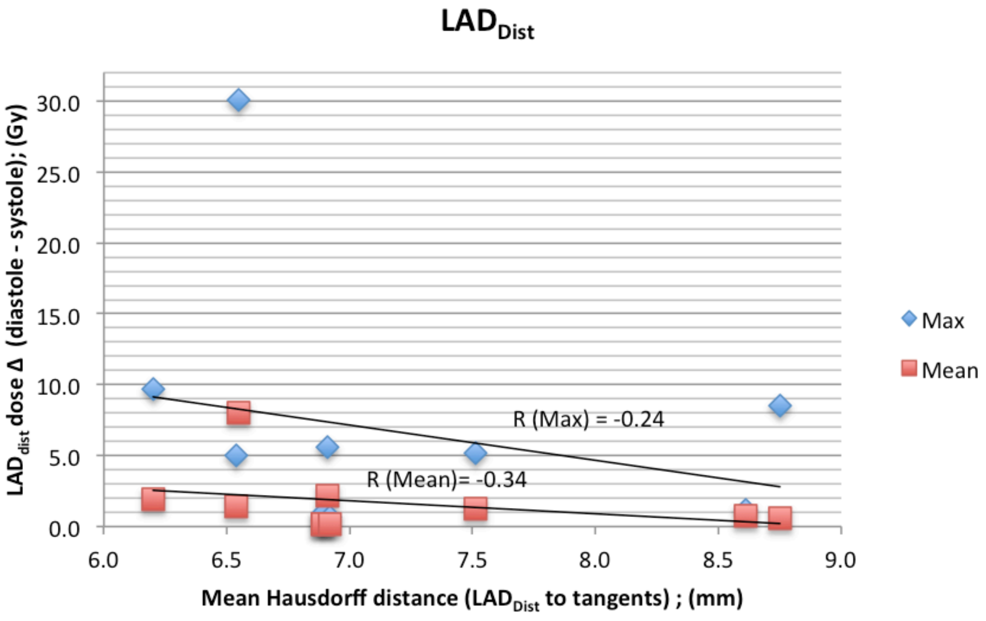

Legend:

Max= maximum dose; Mean = mean dose, V5= volume receiving 5Gy ; WH= whole heart; LV= left ventricle; LADmid= middle LAD; LADdist= distal LAD

10 TROISIÈME ARTICLE SCIENTIFIQUE

Analysis of Pulmonary Vein Antrums Motion with Cardiac Contraction Using Dual Source Computed Tomography

Houda Bahig[1,2], Jacques de Guise[2], Toni Vu[1,2], Danis Blais[1], Carl Chartrand-Lefebvre[2,3], Nhu Tram Nguyen[4], Sophie Lavertu[1,2], Jean-Pierre Guay[1,2], David Roberge[1,2]

[1] *Radiation Oncology Department, Centre Hospitalier de l'Université de Montréal, Montreal, QC. Canada*

[2] *Centre de recherche du Centre Hospitalier de l'Université de Montréal, Montreal, QC. Canada*

[3] *Radiology Department, Centre Hospitalier de l'Université de Montréal, Montreal, QC. Canada*

[4] *Radiation Oncology Department, Juravinski Hospital and Cancer Centre, Hamilton, ON. Canada*

Key Words: Left breast, Tangential irradiation, Coronary arteries, Dual-source computed tomography, Left anterior descending artery, Cardiac dose, Cardiac-gated imaging.

Publication:
Cureus. 2016 Jul 26;8(7):e712. doi: 10.7759/cureus.712. PMID: 27610284

CONTRIBUTIONS: Rédaction du protocole de recherche, coordination et gestion de l'implémentation du protocole de recherche en clinique, récole et analyse des données, interprétation des données, rédaction du manuscrit.

10.1 ABSTRACT

Purpose: The purpose of the study was to determine the extent of displacement of the pulmonary vein antrums resulting from the intrinsic motion of the heart using 4D cardiac dual source computed tomography.

Methods: 10 female patients were enrolled in this prospective planning study. In breath-hold, a contrast-injected cardiac 4 dimensional CT synchronized to the electrocardiogram was obtained using a prospective sequential acquisition method including the extreme phases of systole and diastole. Right and left atrial fibrillation target volumes (CTVR and CTVL) were defined, with each target volume containing the antral regions of the superior and inferior pulmonary veins. Four points of interest were used as surrogates for the right superior and inferior pulmonary vein antrum (RSPVA and RIPVA) and the left superior and inferior pulmonary vein antrum (LSPVA and LIPVA). On our 4D post-processing workstation (MIM Maestro™, MIM Software Inc.), maximum displacement of each point of interest from diastole to systole was measured in the medio-lateral (ML), antero-posterior (AP) and supero-inferior (SI) directions.

Results: Median age of enrolled patients was 60 years (56-71). Within the CTVR, the mean displacements of the superior and inferior surrogates were 3 mm vs. 1 mm (p=0.002), 2 mm vs. 0 mm (p= 0.001) and 3 mm vs. 0 mm (p=0.00001), in the ML, AP and SI directions, respectively. On the left, mean absolute displacements of the LSPVA vs. LIPVA were similar at 4 mm vs. 1 mm (p=0.0008), 2 mm vs. 0 mm (p= 0.001) and 3 mm vs. 1 mm (p=0.00001) in the ML, AP and SI directions.

<u>Conclusion:</u> When isolated from breathing, cardiac contraction is associated with minimal inferior pulmonary veins motion and modest (1-6 mm) motion of the superior veins. Target deformation was thus of a magnitude similar or greater than target motion, limiting the potential gains of cardiac tracking. Optimal strategies for cardiac radiosurgery should thus either incorporate the generation of an internal target or cardiac gating. In either case, cardiac 4D DSCT would allow for personalized margin definition.

10.2 INTRODUCTION

Atrial fibrillation (AF) is the most common type of cardiac arrhythmia, with an estimated prevalence of 4 million in the United States (138), and up to 70% of cases occurring in patients aged between 65 and 85 years old (139). Its consequences involve increased risk of death, increased thromboembolic events as well as decreased quality of life (138). AF is caused by aberrant electrical impulses from the pulmonary veins entering the left atrium, causing ineffective rapid contraction of the left atrium leading to an irregular heart rhythm and potential thrombus formation (140). Electrical isolation of the pulmonary veins through catheter ablation is a well-established treatment approach for atrial fibrillation that has been associated with up to 60% control of AF at 5 years (141). Pulmonary vein isolation by catheter ablation is an invasive procedure that is associated with up to 6% complications rate, including thromboembolic events, myocardial infarction, cardiac tamponade, oesophageal injury or even death (142, 143). A significant proportion of the elderly AF population (with frequent co-morbidities) are thus ineligible for the procedure.

Stereotactic radiosurgery (SRS) as a treatment for AF has been investigated in a limited number of studies. In fact, the ability to create a fibrotic cardiac lesion (144-147) and the potential to induce an electrophysiological effect has been suggested in animal studies (144, 148). SRS potential resides in offering a non-invasive alternative to older patients with significant comorbidities. When considering cardiac SRS, respiratory motion and cardiac contraction are the two sources of heart movement. Whereas several techniques such as breath hold, respiratory gating or near real-time tracking are used to take into account respiratory motion, cardiac contraction remains challenging. Respiratory tracking has been investigated using the Cyberknife system (Accuray Inc. Sunnyvale, USA) with placement of fiducial markers near the target volume (144-146) as well as, more recently, using real time cardiac magnetic resonance imaging (149). Ipsen et al. (149) conducted a dosimetric study in 1 human subject targeting all 4 pulmonary veins antrums. They showed that with use of larger safety margins, heart and esophagus dose constraints were exceeded and target volume coverage was compromised, therefore emphasizing the importance of minimizing unnecessary margins. Whether patients are treated under respiratory tracking method or using a breath-hold technique, a better understanding of the dynamics of cardiac displacement across the 4 pulmonary vein antrums is needed. In this study, we used a dual source computed tomography (DSCT) synchronized to the patient's electrocardiogram, in order to assess diastole-to-systole associated cardiac displacement (28). The purpose of the study was to determine the extent of displacement of each pulmonary vein antrum resulting from cardiac contraction, in order to generate individualized internal target volume margin accounting for cardiac deformation.

10.3 MATERIAL AND METHODS

Study population

Ten female consecutive patients with left breast cancer aged ≥ 18 years old and no known allergy to iodine contrast were prospectively enrolled in a study of cardiac DSCT radiotherapy simulation between July 2015 and March 2016. All patients had baseline electrocardiogram and biochemistry including creatinine level. The protocol and patient consent form were reviewed and approved by our institutional ethics committee.

Cardiac 4D DSCT

A contrast injected (Isovue 370) cardiac 4D DSCT synchronized to patients electrocardiogram (ECG) scan was acquired on a Somatotom Flash Definition (Siemens Healthare, Erlangen, Germany). Contrast injection was at a rate of 4ml/sec and consisted in 3 phases: a) 60 ml of contrast over the first 15 seconds, b) 10 ml of contrast and 10 ml of Sodium Chloride (NaCl) 0.9% over the following 5 seconds and, c) 40 ml of NaCl 0.9% over the final 10 seconds. With a rotation time of 0.28 second using a detector with 64×0.6 mm beam collimation, the acquisition time for the entire cardiac volume was <0.3 second at a temporal resolution of 75 millisecond (28). The cardiac 4D DSCT was obtained in supine position with arms up, using breast board and a vaclock as immobilization device. A prospective sequential acquisition method including 8 phases of the cardiac cycle (20%, 30%, 40%, 50%, 60%, 70%, 80% and 90%) including the extreme phases of systole and diastole was used. Cardiac 4D DSCT was acquired in breath-hold (either deep inspiration breath-hold or natural inspiration breath-hold reproduced using an Abches system (APEX Medical, Tokyo, Japan)).

Pulmonary vein motion assessment

Two clinical target volumes (CTV) were defined for isolation of all 4 pulmonary veins [12]: a right CTV (CTVR), which included the right superior and inferior pulmonary vein antrums (RSPVA and RIPVA) and a left CTV (CTVL), which included the left superior and inferior pulmonary vein antrums (LSPVA and LIPVA). Four regions of interest (ROI) were defined as a 5 mm surface on axial view at the most antero-superior intersection of each pulmonary vein with the left atrium. These ROI, which were representative of the RSPVA, RIPVA, LSPVA and LIPVA, were contoured on each of the 8 cardiac phases by a same observer, with particular care to ensure ROI was segmented at the same location in all phases. Maximal displacement of the centroid of each ROI was derived automatically in a MIM Maestro workstation (MIM Software Inc., Cleveland, OH) in the medio-lateral (ML), antero-posterior (AP) and supero-inferior (SI) directions.

Data were collected in an encrypted electronic database. Student T test was used to compare maximal displacements. Analyses were completed using the SPSS statistics package (IBM Corp. Released 2013. IBM SPSS Statistics for Windows, Version 22.0. Armonk, NY: IBM Corp).

10.4 RESULTS

Patients characteristics

10 female patients with a median age of 60 years (56-71), were included in this study. Baseline ECG showed sinus rhythm in all patients and none of the patients had a past medical history of AF, congestive heart failure or valvular disease. One patient (patient number 8), was on an angiotensin II receptor antagonist for hypertension. No patient presented anatomical variants such as a common pulmonary trunk or an accessory vein — all patients presented a total of 4 pulmonary veins. **Table 6** shows basic DSCT related parameters.

Motion analysis

Plots of maximum cardiac displacement of right superior vs. right inferior pulmonary antrums as well as left superior vs. left inferior pulmonary vein antrums are shown in **Figure 9**. Displacements shown represent motion of each structure in the ML, AP and SI directions, from diastole to systole, secondary to deformation of the CTVR and CTVL. These plots show that the magnitude as well as the direction of the displacements are different for the superior and inferior veins. **Figure 10** shows 5mm ROI on axial view at the most anterior intersection of the right superior pulmonary vein with the left atrium, representative of the RSPVA. Mean displacements of RSPVA, RIPVA, LSPVA and LIPVA are shown in **Table 7**. For the CTVR, mean absolute displacement of RSPVA vs. RIPVA was 3 ± 2 mm vs. 1 ± 1 mm (p=0.002), 2 ± 1 mm vs. 0 ± 0 mm (p= 0.001) and 3 ± 3 mm vs. 0 ± 1 mm (p=0.00001), in the ML, AP and SI directions, respectively. For the CTVL, mean absolute displacement of LSPVA vs. LIPVA was 4 ± 2 mm vs. 1 ± 1 mm (p=0.0008), 2 ± 1 mm vs. 0 ± 0 mm (p= 0.001) and 3 ± 2 mm vs. 1 ± 1 mm (p=0.00001) in the ML, AP and SI directions respectively.

10.5 DISCUSSION

In this study, we determined the extent of displacement of the pulmonary veins resulting from the contractile motion of the heart. Using a cardiac 4D-DSCT, we have shown that margins accounting for cardiac deformation can be individualized and that inferior pulmonary veins were significantly less mobile than their superior counterpart. We found that mean displacement of the superior pulmonary veins was typically 4 mm in the ML direction (reaching up to 8 mm in 1 patient), and 3 mm in the SI direction (reaching up to 7 mm in 1 patient). Mean displacement of the inferior veins was ≤ 1 mm in all directions. Our study was conducted in healthy individuals with no known AF. Cardiac anatomy remodelling in patients with AF has been described (150) and therefore it is possible that our reported pulmonary veins motion dynamics be different from that expected in patients with known AF. However, displacements reported are similar to results from a study by Rettman et al.(151). In that study, clips were placed within the pulmonary vein ostia and left atrial appendage of canine hearts; average displacement of 11 clips placed in 3 canine hearts was 2 mm, 2 mm and 1 in the ML, AP and SI directions, respectively. Importantly, no patient included in our study had a known diagnosis AF, which may limit the applicability of our findings to healthy individuals. AF is particularly challenging when it comes to cardiac imaging, as the rapid rates are associated with significant motion artefacts and impaired image quality. A distinctive feature of our study is the use of DSCT, which provides high temporal resolution, even in patients with AF rhythm (125).

Literature on the role of radiosurgery for the treatment of AF by pulmonary vein isolation remains preliminary. A study on mini swine using the Cyberheart system (Portola Valley, CA), where fiducials were implanted next to the target volume, demonstrated the feasibility of using stereotactic robotic radiosurgery to create cardiac fibrotic lesions as well as to induce a significant decrease in voltage at the pulmonary vein–left atrial junction at a dose of 25 Gy (144). In another animal study targeting the right pulmonary vein ostia, the use of in vivo thermoluminescent dosimeter near the right pulmonary vein, showed that the accuracy of the CyberKnife radiosurgery system within 5% of the predicted dose (146). Using an internal target volume method accounting for both respiratory and cardiac motion, Bode et al. (148) investigated the feasibility of lesion formation in a porcine model. Radiation doses between 23 and 40Gy were delivered to the right superior pulmonary, to which additional margins of 2-3 mm and 10-15 mm for cardiac and respiratory motion were added, respectively. At 6 months, right pulmonary vein voltage was reduced and pathological analysis revealed transmural scarring with doses beyond 30 Gy (148). However, reported toxicities included broncho-mediastinal fistula and AV node block (148). Importantly, treatment of all 4 pulmonary veins would have been associated with a significantly higher treatment volume and likely increased toxicity, highlighting the importance of minimizing internal target volume margins when possible. Using a target volume similar to our study, Ipsen et al. (149) conducted a planning study on 1 patient with AF where all four pulmonary vein antrums were targeted. Using incremental safety margin from 0 to 8 mm, the authors reported that increasing margins was associated with exceeding of heart and esophagus normal tissue tolerance and significant compromise on the target volume coverage.

The heart is subject to two sources of motion during treatment: respiratory motion as well as intrinsic cardiac contraction. If respiratory motion management is now commonplace through breath hold, tracking or gating, cardiac contraction remains a challenge. Delivering a dose that can create fibrosis in the pulmonary vein antrums without complications to surrounding healthy tissues requires maintaining high spatial dose gradients. In our study, we showed that cardiac contraction is associated with deformation of target structures, leading to different displacements of the superior and inferior pulmonary veins, that cannot be taken into account by simple tracking. Whether the patient respiratory motion is taken into by Cyberknife

System, real-time MRI or with breath-hold technique, individualizing assessment of cardiac motion would allow for selection of optimal margins for deformation. An alternative strategy would reside in the development of a cardiac-gated treatment synchronized to ECG signal (152), in which case the multiphase DSCT would help in choosing optimal gating window.

10.6 CONCLUSION

Cardiac contraction seems associated with a negligible inferior pulmonary veins displacement but superior pulmonary veins displacement averaging 4 mm. This difference results from cardiac deformation and highlights the potential limitations of cardiac tracking. In an internal target volume strategy accounting for cardiac deformation, cardiac 4D DSCT would allow for personalized assessment of the displacements of the superior and inferior pulmonary veins, and selection of optimal margin allowing best coverage of the target while avoiding unnecessary irradiation of healthy tissues.

10.7 TABLES ET FIGURES

Table 6- Basic DSCT related parameters

Scan related parameters	Mean	Range
Mean heart rate during scan (bpm)		
CTDIvol-32 cm (mGy)	60.7	42.3-73.0
DLP (mGy-cm)	1072	729-1554
Effective dose (mSv)	15	(10-22)
	N	**%**
DIBH	4	40%

*Bpm= beat per minute ; CTDIvol = volume CT dose index, DLP= dose length, product, mSv = milisievert ; Effective dose was estimated by the product of the DLP and a conversion coefficient for the chest (k= 0.014 mSv*mGy-1*cm-1); N= number of patients; DIBH= Deep inspiration breath-hold.*

Table 7- Mean displacements of RSPVA, RIPVA, LSPVA and LIPVA

	ML (mm)			**AP (mm)**			**SI (mm)**		
	Mean	SD	p	Mean	SD	p	Mean	SD	p
RSPVA	3	± 2	0.002	2	± 1	0.001	3	± 3	0.00001
RIPVA	1	± 1		0	± 0		0	± 1	
LSPVA	4	± 2	0.0008	2	± 1	0.001	3	± 2	0.00001
LIPVA	1	± 1		0	± 0		1	± 1	

RSPVA= Right superior pulmonary vein antrum; RIPVA= Right inferior pulmonary vein antrum; LSPVA= Left superior pulmonary vein antrum; LIPVA= Left superior pulmonary vein antrum; SD= Standard deviation ; ML= Medio-lateral; AP= antero-posterior; SI = supero-inferior.

Figure 9- Plots of maximum cardiac displacement of right superior vs. right inferior pulmonary antrums (A) as well as left superior vs. left inferior pulmonary vein antrums (B)

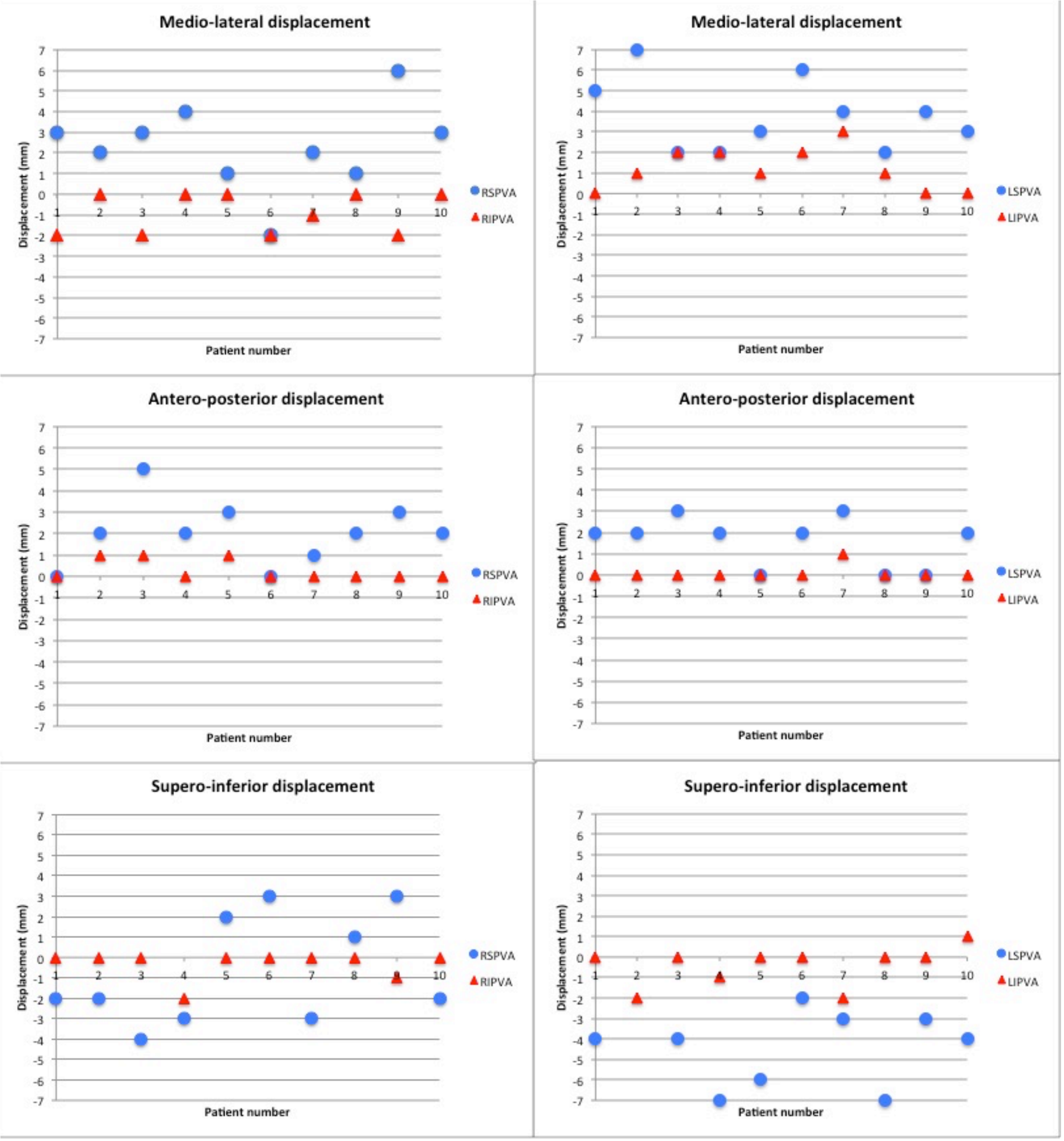

Figure 10- ROI representing the RSPVA defined as a 5 mm axial surface at the antero-superior intersection of the superior pulmonary vein with the left atrium

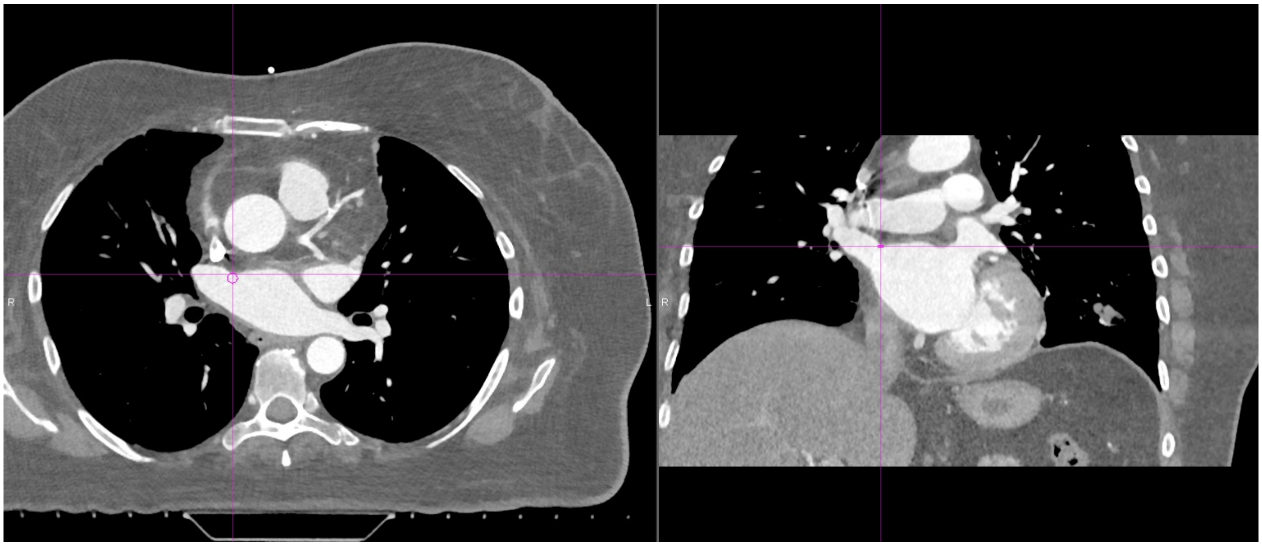

11 QUATRIÈME ARTICLE SCIENTIFIQUE

Use of Dual-Energy Computed Tomography for Prediction of Loco-regional Recurrence in Larynx and Hypopharynx Squamous Cell Carcinoma

Houda Bahig MD[1,4], Andréanne Lapointe PhD[1], Stéphane Bedwani PhD[1], Jacques de Guise PhD[2], Louise Lambert MD[1], Edith Filion MD[1], David Roberge MD[1], Laurent Létourneau-Guillon MD[3], Danis Blais MSc[1], Sweet Ping Ng MBBS[4], Phuc Félix Nguyen-Tan MD[1].

[1]Radiation Oncology Department, Centre Hospitalier de l'Université de Montréal, Montreal, QC.
[2]Centre de Recherche du CHUM, Centre Hospitalier de l'Université de Montréal, Montreal, QC.
[3]Radiology Department, Centre Hospitalier de l'Université de Montréal, Montreal, QC. Canada.
[4]Radiation Oncology Department, University of Texas MD Anderson Cancer Center, Houston, TX.

Key Words: Larynx cancer, Hypopharynx cancer, Dual-energy CT, Iodine, Perfusion, Locoregional control, histogram analysis, radiomics.

Accepted for publication: European Journal of Radiology. September 2018

CONTRIBUTIONS: Rédaction du protocole de recherche, coordination et gestion de l'implémentation du protocole de recherche en clinique, récole et analyse des données, interprétation des données, rédaction du manuscrit.

11.1 ABSTRACT

Purpose: To investigate the role of quantitative pre-treatment dual-energy computed tomography (DECT) for prediction of loco-regional recurrence (LRR) in patients with larynx/hypopharynx squamous cell cancer (L/H SCC).

Methods: Patients with L/H SCC treated with curative intent loco-regional radiotherapy and that underwent treatment planning with contrast-enhanced DECT of the neck were included. Primary and nodal gross tumor volumes (GTVp and GTVn) were contoured on both 100 kV and 140 kV acquisitions and contours were transferred into a Matlab® workspace. Using a two-material decomposition, GTV iodine concentration (IC) maps were obtained. Quantitative histogram statistics (maximum, mean, standard deviation, kurtosis and skewness) were retrieved from the IC maps. Cox regression analysis was conducted to determine potential predictive factors of LRR.

Results: Twenty-five patients, including 20 supraglottic and 5 pyriform sinus tumors were analysed. Stage I, II, III, IVa and IVb constituted 4% (1 patient), 24%, 36%, 28% and 8% of patients, respectively; 44% had concurrent chemo-radiotherapy and 28% had neodjuvant chemotherapy. Median follow-up was 21 months. Locoregional control at 1 and 2 years were 75% and 69%, respectively. For the entire cohort, GTVn volume (HR *1.177* [*1.001-1.392*], p=0.05), voxel-based maximum IC of GTVp (HR 1.099 [95% CI: 1.001-1.209], p=0.05) and IC standard deviation of GTVn (HR 9.300 [95% CI: 1.113-77.725] p=0.04) were predictive of LRR (Table 2). On subgroup analysis of patients treated with upfront radiotherapy +/- chemotherapy, both voxel-based maximum IC of GTVp (HR 1.127 [95% CI: 1.010-1.258], p=0.05) and IC kurtosis of GTVp (HR 1.088 [95% CI: 1.014-1.166], p=0.02) were predictive of LRR.

Conclusion: This exploratory study suggests that pre-radiotherapy DECT-derived IC quantitative analysis of tumoral volume is feasible and may help predict LRR in L/H SCC.

11.2 INTRODUCTION

In the last decades, treatment approaches for larynx and hypopharynx squamous cell carcinoma (L/H SCC) have shifted toward organ-preserving strategies, with the aim of limiting functional impairments associated with total laryngectomy/pharyngolaryngectomy and improving patients' quality of life (153, 154). While organ-preserving trials have provided strong evidence that well-selected patients with L/H SCC may benefit from organ-preservation strategies, there remains substantial controversy on the optimal management of these patients (155). In fact, while cancer outcomes of most head and neck cancer (HNC) subsites have significantly improved over the past decades (156), observational data suggest that 5-year survival rates of L/H SCC have decreased (157). In addition, despite improvement in radiotherapy techniques and systemic treatments, relapse rates in locally advanced L/H SCC after organ-preserving treatment remain high, with 5-year loco-regional recurrence (LRR) reaching 30-40% (158-161). For these reasons, better tumor characterisation through use of imaging biomarkers has the potential to provide insightful information for outcome prediction and treatment selection in L/H SCC. Various functional imaging modalities assessing tumor metabolism, hypoxia, cellularity and perfusion have been investigated in HNC. These modalities notably comprise the use of positron emission tomography (PET), including 18F-fluorodeoxyglucose (FDG-PET) (162-166), 18F-fluoromisonidazole-PET (FMISO-PET) (164, 167) or 18-F-fluoroazomycin arabinoside-PET (FAZA-PET) (168); use of magnetic resonance imaging (MRI), including diffusion weighted imaging (169-171) or dynamic contrast-enhance MRI (168, 169, 172); as well as use of CT perfusion imaging (173, 174). Assessment of tumor perfusion in HNC is considered a useful tool for non-invasive evaluation of intra-tumoral microvessel density and for characterisation of tumor angiogenesis (175, 176).

Dual-energy computed tomography (DECT) is an advanced form of CT in which image acquisition is performed at 2 different energies. This technology allows tissue characterisation through material decomposition and precise voxel-to-voxel determination of iodine concentration, which can be used to derive a regional blood volume map (16, 177, 178). As previously proposed in single energy CT studies (179), we hypothesized that higher tumor iodine content was indicative of increased blood volume and capillary hyperpermeability associated with neoangiogenesis. The role of DECT-derived quantitative imaging to predict oncological outcomes in HNC has never been previously investigated. Yet the rich quantitative information provided by DECT offers a unique opportunity for functional biomarker analysis. The purpose of this study was to investigate the role of DECT-derived quantitative histogram analysis of pre-treatment for prediction of LRR in patients with L/H SCC.

11.3 MATERIAL AND METHODS

Patient population

Patients with larynx or hypopharynx cancer treated with radiotherapy and enrolled between January 2015 and August 2016 in one of 2 prospective studies at the Centre Hospitalier de l’Université de Montréal involving acquisition of pre-treatment planning DECT were included in this study. Inclusion criteria were: (1) histological diagnosis of SCC of the larynx or hypopharynx; (2) curative intent locoregional radiotherapy +/- concurrent chemotherapy; (3) pre-treatment contrast-enhanced planning DECT of the neck. Patients that received induction chemotherapy and had residual disease at time of radiotherapy were included. Patients with early stage (T1-T2N0) glottic cancers were excluded. All cases were discussed in the context of a multidisciplinary tumor board. The protocols and patient consent forms were reviewed and approved by our institutional ethics committee.

DECT and radiotherapy planning

All patients had a 1.5 mm slice thickness planning dual-energy computed tomography (SOMATOM Definition Flash; Siemens Healthineers) from the vertex to the carina with and without intravenous contrast injection in supine position. Immobilisation device included a thermoplastic mask of the head and shoulders fixed to the treatment table. Iohexol contrast bolus was injected (Omnipaque 240 mg/ml) in the antecubital vein at a rate of 2.2 ml/second for a total of 45-50 ml. Immediately after, 40 ml saline solution was sequentially injected at a rate of 2.2 ml/second. DECT was acquired 5 seconds after contrast bolus tracking in the ascending aorta. Two sets of spiral CT data were simultaneously acquired with the following parameters: slice thickness of 2 mm, pitch of 0.55, rotation time of 0.28 seconds, collimation of 64 x 0.6 mm and X-ray tube potentials of 100 kVp and 140Sn kVp (Sn= additional tin filtration), a matrix of 512 × 512 pixels, a field of view of 50 cm and a voxel size of 1 × 1 × 1 mm^3. A Q30 filter kernel was used for image reconstruction. Tube current modulation was used in for individual radiation dose optimization. When available, planning positron tomography (PET)-CT and magnetic resonance imaging were fused with planning CT.

Patients were treated with volumetric arc modulated radiotherapy (RapidArc®, Varian

Medical Systems, Palo Alto, CA) using 6-MV photons. Patients undergoing definitive radiotherapy +/- concurrent chemotherapy were treated to a dose to 70 Gy in 35 fractions to the gross disease, 60 Gy in 30 fractions to high risk nodal region and 50 Gy in 25 fractions to low risk nodal region, given in 5 daily fractions per week. Treatment plans were normalised so that the prescription dose covered at least 95% of the PTV volume. Eclipse TPS (Varian Medical Systems, Palo Alto, CA) with Analytical Anisotropic Algorithm was used for dose calculation.

DECT-derived iodine concentration map and histogram analysis

Primary gross tumor volume (GTVp) and nodal gross tumor volume (GTVn) were retrospectively contoured by a radiation oncologist (HB) on the 100 kV CT series on a MIM Maestro workstation (MIM Software Inc., Cleveland, OH), contours were subsequently transferred to the 140 kV series. Using an in-house script (Matlab — MathWorks, Natick, MA), iodine concentration (in mg/ml) was extracted from GTVp and GTVn structures by determining the iodine partial electron density from each voxel, using a two-material decomposition method previously described by our group (49) and based on principal component analysis called eigentissue decomposition (180). **Figure 11** shows an example of GTVp iodine concentration map for a patient with stage T2 supraglottic larynx cancer. Quantitative histogram analysis was performed to retrieve statistics from GTVp and GTVn iodine maps.

Follow-up and statistics

Patients had alternating follow-up by their otolaryngologist and radiation-oncologist every

2 months for the first 2 years, every 4 months for the following 3 years. Every patient had a follow-up CT scan 6–8 weeks after treatment and if symptoms and/or results on physical examination were suspicious for recurrence. LRR was detected on clinical examination and/or CT scan (± FDG-PET scan) and confirmed histologically. Follow-up duration was defined from the date of treatment completion to the date of last follow-up or death. Kaplan–Meier method was used for estimation of locoregional control and relapse free survival (RFS). Univariate Cox regression analysis was performed to determine predictors of LRR, with p values $p \leq 0.05$ considered statistically significant. Descriptive statistics retrieved from iodine concentration included maximum, mean, standard deviation, kurtosis and skewness. Clinical factors such as age, gender, tumor site, smoking status, stage, GTVp and GTVn volumes were also analyzed. SPSS 24 (IBM, Armonk, NY) was used for statistical analysis.

11.4 RESULTS

Patients and treatments characteristics

In total, 25 patients met inclusion criteria. Twenty-five patients, including 20 supraglottic and 5 pyriform sinus tumors were analysed; 76% were male. Median age was 65 years (43-79). Median GTVp was 7.9 cm^3 (range= 0.7-51.8 cm^3) and median GTVn was 7.0 cm^3 (range= 0.5-25.8 cm^3). Stage I, II, III, IVa and IVb constituted 4% (1 patient), 24%, 36%, 28% and 8% of patients, respectively. Forty-four percent had concurrent cisplatin and 28% had neoadjuvant chemotherapy consisting of docetaxel-cisplatin or paclitaxel-carboplatin. Patients and treatment characteristics are summarized in **Table 8.**

Treatment outcomes

The median follow-up time was 21 months (range: 9-34 months). Relapse patterns were as follow: 4 patients presented isolated local recurrence, 1 patient had synchronous local and regional recurrence, 1 patient had synchronous regional and distant recurrence, and 1 isolated distant metastasis. Actuarial LRR at 1 and 2 years was 75% and 69% (**Figure 12**). Actuarial RFS at 1 and 2 years was 70% and 64%% at 2 years (**Figure 13**).

Predictors of LRR

Table 9 presents univariate Cox regression analysis for risk of LRR for the entire cohort, while **Table 10** presents univariate Cox regression analysis for risk of LRR for the subgroup of patients treated with upfront radiation +/- concurrent chemotherapy. For the entire cohort, GTVn volume (HR *1.177* [*1.001-1.392*], p=0.05), voxel-based maximum IC of GTVp (HR 1.099 [95% Confidence Interval (CI): 1.001-1.209], p=0.05) and IC standard deviation of GTVn (HR 9.300 [95% CI: 1.113-77.725] p=0.04) were predictive of LRR (**Table 9**). On subgroup analysis of patients treated with upfront radiotherapy +/- chemotherapy, both voxel-based maximum IC of GTVp (HR 1.127 [95% CI: 1.010-1.258], p=0.05) and IC kurtosis of GTVp (HR 1.088 [95% CI: 1.014-1.166], p=0.02) were predictive of LRR (**Table 10**).

11.5 DISCUSSION

To our knowledge, this is the first study reporting on the potential role of DECT-derived quantitative imaging for outcome prediction in HNC. In this study, we describe a novel method allowing for volumetric extraction of iodine fraction from each voxel of the primary tumor and involved lymph nodes in L/H SCC. Iodine concentration was used as a surrogate for regional blood volume, with the working hypothesis that increased tumor angiogenesis would result in higher iodine contrast enhancement, as previously supported in single energy CT studies (179). In our pilot cohort of 25 patients, higher maximum IC of the primary tumor as well as higher volume and IC standard deviation of involved lymph nodes were predictive of LRR in L/H SCC. In the subgroup of patients treated with upfront radiation +/- concurrent chemotherapy, both higher maximum IC and higher IC kurtosis of the primary tumor were predictive of cancer relapse. While the prognostic value of nodal tumor volume has previously been reported (181), this preliminary study suggests that DECT-derived iodine map histogram metrics have the potential to provide easily accessible information that can be valuable for tumor characterization, outcome prediction, treatment selection and dose painting. Contrary to oropharynx cancer where prognostic factors such as p16 status have been widely recognized, there are limited markers that help us predict LRR in L/H cancers.

DECT is an advanced imaging technique allowing for acquisition of 2 series of CT images at different energies. Based on the principle of energy-dependant photoelectric effect, precise tissue characterization and quantification of different materials such as iodine can be achieved (16). DECT offers a unique opportunity for analysis of imaging biomarker; however, in current literature, its use for outcome prediction is generally unexplored. In one study focusing on assessment of iodine content of cervical neck nodes, Tawfik et al. (182) reported that lower mean iodine content derived from DECT could differentiate metastatic SCC from normal or inflammatory lymph nodes. Unlike our study, iodine content measurements were limited to a region of interest in the axial section and only mean and standard deviation values of iodine content were reported. In a study by Kuno et al. (183), the combination of weighted average and iodine overlay images was found to improve the diagnostic performance and inter-observer reproducibility of laryngeal cartilage invasion assessment from HNC SCC (183). In lung cancer, Schmidt-Binder et al. (184) reported a strong correlation between maximum standardized uptake value of 18- fluorodeoxyglucose positron emission tomography (18FDG-PET)/CT and maximum iodine-related attenuation on DECT for both primary tumours and involved thoracic lymph nodes of non-small cell lung cancer. The latter study suggests an association between metabolic activity and perfusion and is in concordance with our findings that maximum tumoral IC is associated with worse outcomes.

Perfusion imaging as a surrogate of angiogenesis and predictor of oncological outcomes has previously been largely studied in HNC but results have generally been conflicting (185-190). On one hand, several studies have reported an association between increased tumor perfusion and improved treatment response, supporting that poor tumor perfusion induces hypoxia and radioresistance (186, 191). On the other hand, other studies have supported a correlation between elevated perfusion, tumor recurrence and metastatic potential, suggesting that highly perfused tumors may present a more aggressive biology (190, 192). Pietch et al. (192) reported significantly higher pre-treatment CT-derived perfusion metrics (blow flow, blood volume and mean transit time) in recurrent HNC tumors. Similarly, using PET with oxygen-15-labeled water for assessment of blood flow, Lehtio et al. reported poor local control after radiotherapy and decreased survival in tumors with higher pre-treatment blood flow (190). These studies support the hypothesis that high perfusion may rather be a consequence of the neovascularization induced by hypoxia (187, 193-195). Discrepancies on the prognostic value of perfusion can be in part explained by the differences in imaging techniques and perfusion measurements in current studies, and on the other part, by the combination of various HNC tumors subsites which does not allow to account for the heterogeneous biology of individual tumours. Interestingly, a study by the Memorial Sloan Kettering Cancer Center recently reported on dual assessment of tumor hypoxia and perfusion in 120 HNC patients that underwent 18F-FMISO-PET. In this study, both positive and negative correlation between hypoxia and perfusion were observed for individual lesions (164), supporting that both scenarios are possible and likely vary based on tumor biology. In addition, an association between angiogenesis and glucose metabolism was also supported by positive correlation shown between maximum standardized uptake value on PET and perfusion in moderately large (stage T2–3) HNC tumors (196). Increasing level of evidence suggests that perhaps quantification of heterogeneity of tumors perfusion is key in understanding inter- and intra-tumour phenotypes as well as in predicting HNC outcomes (172, 197-199). This is also supported by findings from our study where higher IC kurtosis (representing peakedness of the shape of the probability distribution) of primary tumor and higher IC standard deviation (reflecting dispersion of the histogram) of involved lymph nodes were found to be potential biomarkers. To this effect, DECT-derived iodine map histogram metrics offer an opportunity for better quantification of tumour perfusion heterogeneity, as a window to individual phenotypes of HNC tumors. In addition, DECT-derived functional imaging may be of particular use in L/H SCC, where use of functional MRI remains limited by swallowing and breathing motion. Additional advantages of this method include reduced radiation dose compared to dynamic CT as well as easy implementation as part of radiotherapy planning workflow given the increased applications of DECT for improved precision of dose calculation (137).

Our study aimed at assessing the feasibility of using DECT-derived IC maps for clinical outcome prediction. This study is limited by its small sample size as well as by its heterogeneous cohort of patients. In fact, although our cohort has the advantage of focusing on L/H SCC exclusively, patients with mixed cancer stages and mixed treatment modalities were included. As it is possible that induction chemotherapy induced iodine map alteration that may have affected the validity of our results, we proceeded to a subgroup analysis of patients treated with upfront radiotherapy +/- chemotherapy, with similar findings in regards to maximum GTVp IC, in addition to GTVp kurtosis of iodine map. In addition, another important limitation of our study is that only voxel-based maximum iodine concentration was associated with risk of LRR, but not 99 iodine concentration percentile. Voxel-based maximum iodine concentration value is more vulnerable to noise compared to use of a larger region of interest such as 99 iodine concentration percentile. Preliminary findings of our study warrant further validation in a larger cohort. Due to the small sample size and exploratory nature of the study, only a univariate analysis of potential predictive factors of LRR was conducted.

11.6 CONCLUSION

In conclusion, we demonstrated feasibility of pre-radiotherapy DECT-derived IC quantitative analysis, as a potential surrogate of microvessel density and heterogeneity of perfusion. The described method is a promising tool for outcome prediction in L/H SCC. Maximum IC and IC kurtosis of primary tumor, as well as IC standard deviation of involved lymph node are readily available imaging biomarkers that can be derived from pre-treatment diagnostic or planning DECT and that may help predict LRR in L/H SCC. Validation of the predictive value of these biomarkers in a larger cohort of patients is required.

11.7 TABLES ET FIGURES

Table 8- Patients and tumors' characteristics

Age; median (range)		65 (43-79)
Gender		
	Female	6 (24%)
	Male	19 (76%)
Subsite		
	Larynx	20 (80%)
	Hypopharynx	5 (20%)
Active Smoker		
	Yes	7 (28%)
	No	18 (72%)
T stage		
	T1	16%
	T2	44%
	T3	40%
N stage		
	N0	11 (44%)
	N1	5 (20%)
	N2	7 (28%)
	N3	2 (8%)
GTVp volume; cm^3 (median; range)		7.9 (0.7-51.8)
GTVn volume (N=14); cm^3 (median; range)		7.0 (0.5-25.8)

Concurrent chemotherapy	13 (52%)
Neoadjuvant chemotherapy	7 (28%)

IHC= Immunohistochemistry; GTVp= Primary gross tumor volume; GTVn= nodal gross tumor volume

Table 9- Univariate Cox regression analysis of all variables for risk of LRR for entire cohort

			HR (95% CI)	**p**
	LRR	**No LRR**		
Clinical features				
Male (vs. Female) (%)	71%	72%	0.881 (0.171-4.549)	0.8
Age; M (y)	60	64	0.975 (0.910-1.044)	0.4
Active smoker (vs. Non smoker) (%)	43%	22%	2.435 (0.542-10.938)	0.4
T3 (vs. T1-2) (%)	29%	44%	0.744 (0.327-1.695)	0.6
N+ (vs. N0) (%)	57%	56%	1.276 (0.283-5.743)	0.8
Hypopharynx (vs. Larynx) (%)	29%	28%	1.258 (0.537-2.945)	0.6
Volume GTVp; M (cm^3)	11.5	6.5	1.035 (0.981-1.091)	0.2
Volume GTVn; M (cm^3)	***11.4***	***5.2***	***1.177 (1.001-1.392)***	***0.05***
GTVp histogram analysis				
IC max; M (mg/ml)	***21.0***	***16.1***	***1.099 (1.001-1.209)***	***0.05***
IC max 99 percentile; M (mg/ml)	8.5	8.2	1.01 (0.780-1.307)	0.9
IC mean; M (mg/ml)	1.9	1.6	1.977 (0.708-5.226)	0.2
IC SD; M (mg/ml)	2.1	1.9	1.367 (0.440-4.248)	0.6
IC skewness; M (mg/ml)	2.0	2.1	0.993 (0.562-1.756)	0.9
IC kurtosis; M (mg/ml)	17.8	13.2	1.009 (0.980-1.039)	0.5
GTVn histogram analysis (N=14)				
IC max; M (mg/ml)	10.5	7.6	1.226 (0.908-1.655)	0.2
IC max 99 percentile; M (mg/ml)	6.6	4.1	1.526 (0.997-2.336)	0.06
IC mean; M (mg/ml)	1.5	1.8	0.967 (0.512-1.827)	0.9
IC SD; M (mg/ml)	***1.6***	***1.1***	***9.300 (1.113-77.725)***	***0.04***
IC skewness; M (mg/ml)	1.2	0.9	1.461 (0.278-7.694)	0.7
IC kurtosis; M (mg/ml)	4.4	4.7	0.907 (0.481-1.712)	0.8

HR= Hazard ratio; CI= confidence interval; LRR= loco-regional recurrence; M= mean; IC = iodine concentration; N= number

Table 10- Cox regression analysis for risk of LRR for subgroup of patients treated with upfront radiation +/- chemotherapy (N=17)

			HR (95% CI)	**p**
	LRR	**No LRR**		
Clinical features				
Male (vs. Female); (%)	57%	58%	0.907 (0.388-2.123)	0.8
Age; M (y)	59	63	0.978 (0.912-1.049)	0.5
Active smoker (vs. Non smoker) (%)	50%	17%	5.010 (0.901-27.863)	0.06
T3 (vs. T1-2); (%)	17%	33%	0.602 (0.205-1.772)	0.4
N+ (vs. N0) (%)	50%	42%	1.168 (0.233-5.857)	0.8
Hypopharynx (vs. Larynx) (%)	17%	17%	1.053 (0.359-3.089)	0.9
Volume GTVp; M (cm^3)	12.7	6.8	1.022 (0.970-1.076)	0.4
Volume GTVn; M (cm^3)	13.8	3.9	1.159 (0.983-1.1366)	0.08
GTVp histogram analysis				
IC max; M (mg/ml)	***23.0***	***16.1***	***1.127 (1.010 1.258)***	***0.03***
IC max 99 percentile; M (mg/ml)	9.2	6.1	1.160 (0.876-1.538)	0.3
IC mean; M (mg/ml)	2.0	1.8	1.736 (0.504-5.978)	0.4
IC SD; M (mg/ml)	2.3	1.6	*1.120 (0.348 3.612)*	*0.8*
IC skewness; M (mg/ml)	2.1	1.6	1.640 (0.705 3.815)	0.2
IC kurtosis; M (mg/ml)	***19.4***	***8.1***	***1.088 (1.014 1.166)***	***0.02***
GTVn histogram analysis (N=9)				
IC max; M (mg/ml)	14.3	8.3	1.264 (0.865-1.846)	0.2
IC max 99 percentile; M (mg/ml)	6.9	4.5	1.397 (0.875-2.085)	0.2
IC mean; M (mg/ml)	1.6	2.6	0.775 (0.311-1.930)	0.8
IC SD; M (mg/ml)	1.8	1.1	3.682 (0.775-17.499)	0.1
IC skewness; M (mg/ml)	1.2	0.6	5.358 (0.078-366.072)	0.4
IC kurtosis; M (mg/ml)	4.3	4.1	1.244 (0.335-4.622)	0.7

HR= Hazard ratio; CI= confidence interval; LRR= loco-regional recurrence; M= mean; IC = iodine concentration; N= number.

Figure 11- Weighted average axial DECT from patient with T2 supraglottic SCC.

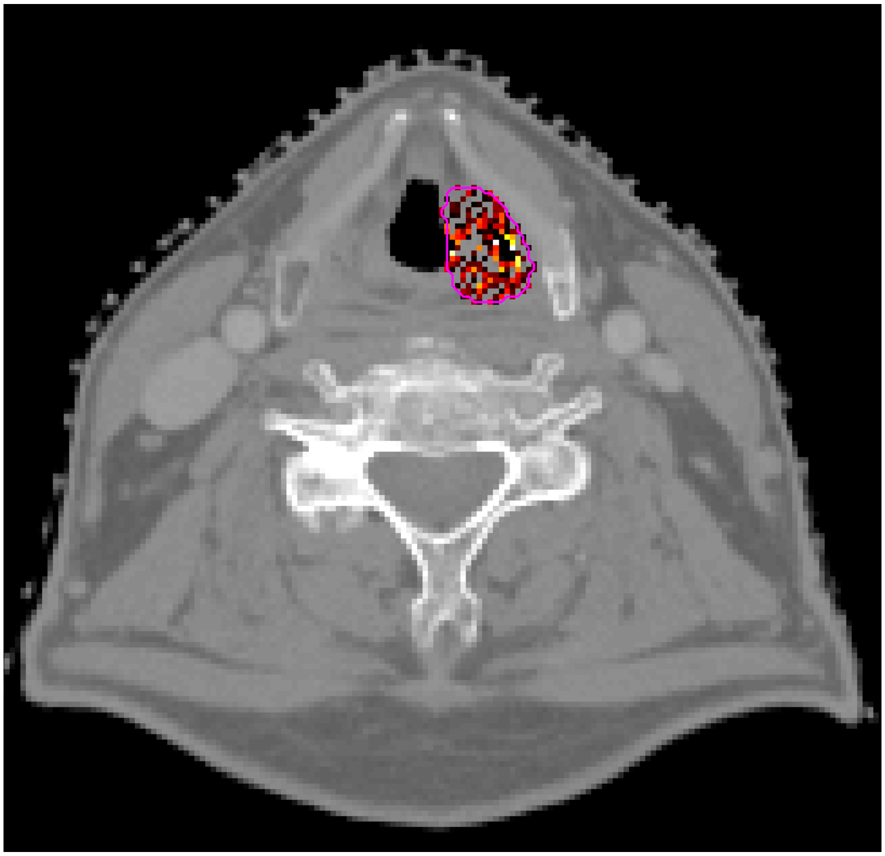

Legend:

Pink contour: Gross tumor volume from stage T2 supraglottic larynx SCC. Iodine concentration map within GTV is shown, with increasing levels of iodine concentration from light yellow to black.

Figure 12- Kaplan Meier curves of loco-regional control (LRC) as a function of time

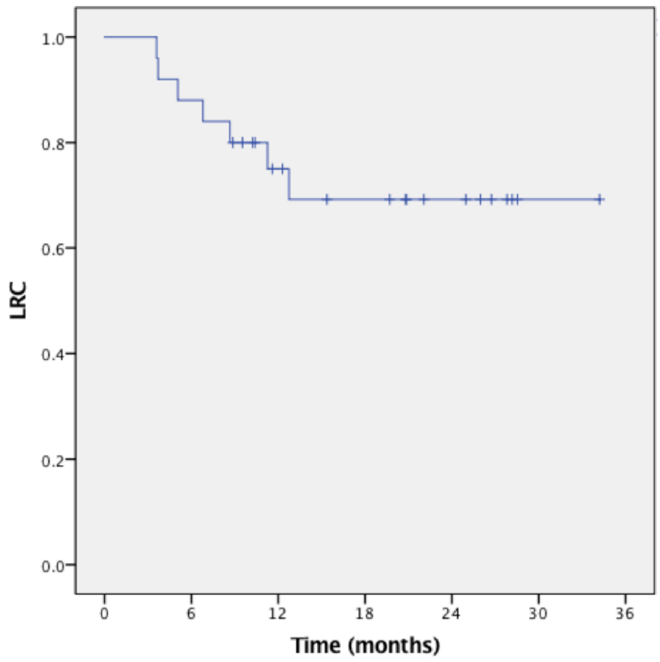

Figure 13- Kaplan Meier curves of relapse-free survival as a function of time

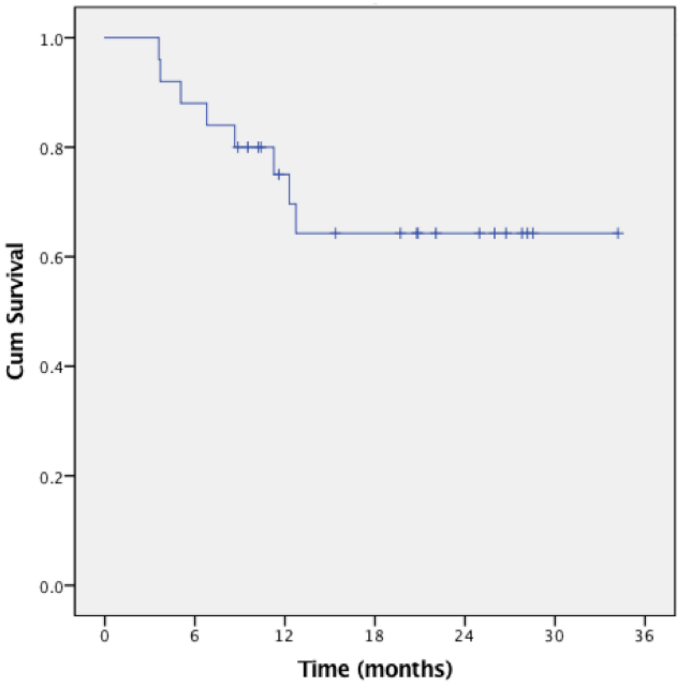

12 DISCUSSION GENERALE

Les potentielles applications du DECT/DSCT en radio-oncologie sont nombreuses. Étant donné la relative simplicité de l'intégration de cette modalité en planification de radiothérapie, l'intérêt clinique est grandissant, mais les évidences cliniques demeurent embryonnaires. Nos travaux sont en effet parmi les premiers à évaluer le rôle du DECT/DSCT en radiothérapie. Nous avons démontré le potentiel de cette technologie à divers niveaux en vue de personnaliser la planification des traitements radiothérapie, notamment pour : l'évaluation de la fonction des tissus sains, l'évaluation du mouvement cardiaque, ainsi que pour la prédiction des récidives tumorales. Ci-dessous, nous discutons des rôles que cette technologie peut jouer dans le flux de travail de la planification de radiothérapie, ainsi que de ses limitations potentielles.

12.1 CARACTÉRISATION DES TISSUS SAINS

La possibilité de distinguer et de quantifier les différents matériaux rend l'utilisation du DECT particulièrement intéressante pour l'évaluation fonctionnelle des tissus sains. L'évaluation fonctionnelle des tissus sains en planification de radiothérapie peut être utilisée soit pour minimiser les toxicités induites par la radiation, soit simplement pour mieux prédire les toxicités dans le but d'une prise en charge plus efficace.

a) Le parenchyme pulmonaire

Le DECT peut évaluer la fonction du parenchyme pulmonaire en mesurant la perfusion (Iode) tel que démontré dans le cadre de notre étude, ou en mesurant la ventilation (xénon inhalé) (200). Tel que discuté au *Chapitre 8*, en radiologie diagnostique, plusieurs études ont démontrées que la distribution d’iode du DECT pouvait être utilisée pour détecter des défauts de perfusion dans le contexte d’embolies pulmonaires (63-67) ainsi que de maladies parenchymateuses (68, 69). Après inhalation par le patient de 30% de xénon par un système d’inhalation (201, 202), le DECT permet également la quantification des anomalies de ventilation à travers l’atténuation caractéristique du Xénon dans le poumon, le plus souvent déterminée suite à une caractérisation à 3 matériaux (air, Xénon, parenchyme pulmonaire) (202-204). Il est intéressant de noter que le bénéfice ajouté de la ventilation pour l’évaluation de la fonction pulmonaire demeure sujet de controverse. Thieme et al. (200) a utilisé le DECT en combinant la perfusion (Iode) et ventilation (Xenon) chez 8 patients pour l’évaluation fonctionnelle des poumons chez des patients aux soins intensifs pour lesquels des détériorations de l’échange gazeux était attendues. Cette étude a démontré la faisabilité technique d’une évaluation exhaustive de la perfusion, de la ventilation, de même que de la structure du parenchyme. Les auteurs ont conclu que l’utilisation combinée de ventilation/perfusion avait le potentiel de mieux caractériser et différentier les atteintes parenchymateuses fonctionnelles (fibrose, emphysème, exsudat inflammatoire ou autre) (205), et leur sévérité (206). Toutefois, la faisabilité de l’intégration de la ventilation/perfusion en planification de radiothérapie demeurera à évaluer dans des travaux futurs qui balanceront le bénéfice ajouté avec la complexité augmentée de l’interprétation et de l’optimisation des plans de radiothérapie utilisant l’information combinée. L’avantage les plus évident de l’utilisation de la perfusion tel que proposé dans notre étude est celui d’une simplification du flux de travail, en omettant un examen supplémentaire, puisque les patients ont généralement un scan avec injection de contraste iodé au moment de la planification. Ainsi, le scan planification peut être acquis en mode DECT et la carte d’iode contenant l’information fonctionnelle peut alors être dérivée « gratuitement », c’est à dire sans dose d’irradiation, coût, risque ou déplacement additionnel.

b) Autres tissus sains

L’extraction de l’information fonctionnelle à partir de la carte d’iode d’un organe sain, avec l’hypothèse sous-jacente que la perfusion est corrélée à la fonction, peut théoriquement être étendue à de multiples autres organes en radiothérapie. A titre d’exemples, des corrélations entre la fonction et la perfusion (utilisant d’autres modalités d’imagerie comme l’IRM ou le CT dynamique) ont été proposées pour l’évaluation de la fonction des glandes salivaires, du foie ou des reins (10, 207-209). Cela dit, le dynamisme du passage du contraste iodé dans différents organes peut constituer une limitation lors de l’obtention d’une carte d’iode « statique » dérivant l’information fonctionnelle. En effet, l’une des pistes initialement explorée dans le cadre de nos travaux était celle de l’évaluation de la fonction rénale différentielle en planification de radiothérapie abdominale, afin de guider l’orientation des faisceaux de radiothérapie et éviter les zones rénales les plus fonctionnelles. En se basant sur des études antérieures utilisant le CT à simple énergie ou en scintigraphie (210-213), l’hypothèse testée était que la quantité de contraste qui s'accumule dans le parenchyme lors de la phase médullaire du néphrogramme serait directement proportionnelle au débit de filtration glomérulaire du rein et permettrait donc d’extraire sa contribution relative. Toutefois, une limitation importante de cette méthode, en lien avec le haut dynamisme du contraste dans le système urinaire, est la grande variabilité inter-patients de la filtration du contraste iodé. Cette variabilité étant multifactorielle (poids du patient, fonction intrinsèque des reins), la précision de nos prédictions était nécessairement limitée. En effet, notre expérience a révélé que l’acquisition à une phase spécifique du néphrogramme était difficile à obtenir, malgré l’utilisation d’un « bolus tracking ». Dans une majorité de cas, une acquisition trop précoce ou tardive a nuit significativement à l’interprétation des résultats. Dans le cas des reins, l’alternative de l’utilisation d’un CT dynamique pourrait être plus appropriée. Dans le cas du CT dynamique, après injection intraveineuse de contraste iodé, des acquisitions à intervalles réguliers sur une durée d’environ 2 minutes permettent de générer une courbe signal-temps et ainsi de dériver la fonction rénale absolue (en plus de l’information relative) (214-216). Le CT dynamique est toutefois limité par la dose de radiation beaucoup plus importante de cette méthode. Les défis rencontrés lors de la transposition de la méthode de carte d’iode fonctionnelle des poumons vers le rein supportent que la validité de la carte d’iode statique, de même que le protocole d’imagerie (débit du contraste, temps optimal d’acquisition), devraient être évalués individuellement pour chaque organe dans des études futures.

En plus de la quantification du contraste iodé, le DECT a également le potentiel de permettre une meilleure évaluation de la minéralisation osseuse à travers une caractérisation de l’architecture et de la distribution de la densité osseuse, ce qui peut aider à évaluer les fractures de compression ou la présence de nécrose post-radique (217-219). En radiologie diagnostique, quelques études publiées antérieurement ont montré que le DECT permettait de détecter avec succès l'oedème de la moelle osseuse après un traumatisme osseux aigu, et aidait à différentier les fractures aigues des fractures chroniques (220, 221). Dans une étude animale récente, Poort et al. a rapporté que l’évaluation de l’oedème de moelle osseuse au DECT était utile pour diagnostiquer l'ostéoradionécrose de la mandibule (222). Dans cette étude, le DECT s’est avéré performant pour la détection des changements osseux structurels incluant les ruptures corticales et l’oedème (222).

12.2 CARACTÉRISATION TUMORALE

Le rôle du DECT pour la caractérisation tumorale est prometteur et l’étude présentée au *Chapitre 11* démontre un exemple d’application qui peut être exportée à d’autres sites tumoraux. Il a été vastement reporté que la vascularisation tumorale peut prédire la réponse au traitement ou les contrôles tumoraux dans divers sites tumoraux (184, 223-225). Similaire à l’étude présentée dans le cadre de nos travaux, une étude observationnelle est actuellement en cours à l’Université d’Ottawa (NCT02279459). Dans cette étude, le groupe de l’Université d’Ottawa évalue la densité microvasculaire des tumeurs ORL sur DECT en prétraitement ainsi qu’à 2 semaines en cours de radiothérapie et prévoie corréler la vascularisation tumorale observée au DECT avec les taux de réponse à la radiothérapie.

En radiologie diagnostique, plusieurs travaux ont rapporté le bénéfice des cartographies d’iode ainsi que des reconstructions monoénergétiques de faible énergie au DECT pour la détection, la délimitation et la stadification de tumeurs hépatiques, thoraciques, rénales, pancréatiques ou ORL (226-230). Les caractéristiques des courbes d'atténuation de tumeurs sur différentes reconstructions mono-énergétiques ont également été utilisées pour différencier des lésions bénignes des lésions malignes (184, 223-225). Des études ont notamment montrées une meilleure évaluation de l’envahissement cartilagineux dans les cancers de la sphère ORL (183), de l’atteinte ganglionnaire dans le cancer de l’estomac (231) et de la profondeur d’envahissement des tumeurs rectales (232). La délinéation tumorale est particulièrement utile pour les lésions se situant au sein de tissus mous et pour lesquelles l’évaluation des bordures peut être plus difficile. De plus, en présence de métal, par exemple dans le contexte d’implants métalliques en radiothérapie de la colonne ou de prothèses dentaires en radiothérapie ORL, d’importants artéfacts peuvent nuire à la délinéation tumorale et des organes à risque, en plus d’induire des erreurs de calcul de dose. Dans ces cas particuliers, la délinéation des volumes pourrait être améliorée par une réduction des artefacts métalliques en utilisant des images virtuelles monochromatiques à haute énergie, moins affectées par les artéfacts de durcissement de faisceaux (233).

12.3 IMAGERIE CARDIAQUE

Le cœur constitue un organe à risque critique pour plusieurs cancers traités par radiothérapie, parmi lesquels on compte les cancers du sein, poumon, œsophage ou médiastin (i.e. lymphome, thymome). Le constant mouvement du coeur et la petite taille des artères coronariennes présentent un défi considérable pour la définition de ces structures à risque en radiothérapie. La quantification du mouvement des sous-structures cardiaques sans artéfacts de mouvement est d’autant plus importante dans le contexte de l’intérêt émergent pour le traitement non-invasif des arythmies cardiaques par radio-ablation (234). En cardiologie, en plus de l'évaluation anatomique des artères coronariennes pour une angiographie non-invasive en mode DSCT (235), l’imagerie par DECT permet également l’évaluation de la perfusion myocardique, sous le même principe de caractérisation tissulaire exploré dans le cadre du *Chapitre 8* (236). En effet, il a été démontré que le DECT permettait de cartographier la distribution de l'iode dans le myocarde comme marqueur quantitatif de la perfusion et du volume sanguin (237). Dans le contexte de la radiothérapie, au delà des applications décrites aux *Chapitres 9 et 10* en lien avec l'évaluation du mouvement, des travaux futures impliquant une évaluation morphologique et fonctionnelle étendue du myocarde et des coronaires par DECT/DSCT seraient pertinents afin de mieux comprendre les relations qu'il existe entre les doses reçues par les sous-structures du coeur et les complications subaiguës et tardives induites par la radiation.

12.4 LIMITATIONS DU DECT/DSCT

Quoique prometteuse, la technologie du DECT/DSCT a toutefois plusieurs limitations. En ce qui concerne les cartographies d'iode, des artéfacts en lien avec un durcissement de faisceau dans les régions à haute concentration d'iode ont été observés et peuvent nuire à l'analyse et interprétation de l'image (238). Il demeure donc toujours important d'interpréter ces cartographies d'iode conjointement avec les images virtuelles monochromatiques de faible énergie pour s'assurer de la cohérence anatomique. De plus, il a préalablement été décrit que l'exactitude de séparation des matériaux pouvait être affectée par la qualité bruitée des images de faible kV- ce qui est d'autant plus accentué chez les patients souffrant d'obésité (239). La taille du champ de vision *(field of view)* sur lequel les données de l'énergie à faible kV sont obtenues est limité à 33 cm dans la nouvelle génération du DECT à double source- ce qui peut empêcher l'évaluation adéquate des patients à large diamètre corporel, en particulier pour les images de la région abdominale (240). De plus, dans le contexte émergent de l'utilisation du DECT pour dériver des biomarqueurs en imagerie fonctionnelle, il existe un important besoin de standardiser les protocoles d'acquisition dans le but d'établir des métriques comparables entre institutions (ex : quantité de contraste injecté, temps d'acquisition, énergies kV) (241). Tel que préalablement discuté, dans le contexte spécifique de notre projet, la cartographie du flux sanguin régional est obtenue par DECT statique ; nous n'avons donc pas l'information du dynamisme du contraste dans le temps qui peut également être indicateur de fonction. L'obtention de DECT dynamique, bien que possible, serait toutefois associée à une augmentation significative de la dose de radiation.

Du point de vue organisationnel, l'implémentation du DECT/DSCT est associée à une augmentation du nombre de séries d'images à sauvegarder dans les systèmes d'archivage d'imagerie (*PACS, Picture Archiving and Communication System*), une augmentation du temps d'interprétation par les radiologistes, ainsi qu'à un besoin de formation du personnel (technologues, radiologues, radio-oncologues) pour l'acquisition et l'interprétation d'images (242). Enfin, dans le contexte du rôle grandissant de l'IRM anatomique et fonctionnelle pour la caractérisation tissulaire et l'évaluation du mouvement, le rôle futur du DECT/DSCT pourrait se voir diminuer considérant l'avantage compétitif de l'IRM de ne pas exposer les patients aux rayonnements ionisants. Bien que l'utilisation de l'IRM demeure plus complexe à intégrer dans le flux de travail de la radiothérapie, dans le contexte des développements de récents mais encore expérimentaux visant à utiliser l'IRM exclusive pour remplacer l'actuel CT de planification pour le calcul de dose en radiothérapie (243), les avantages de l'utilisation du DECT/DSCT pourraient devenir marginaux dans le futur.

Les travaux futurs de notre équipe impliqueront 4 volets : 1- Une évaluation sériée des changements fonctionnels post-radiques dans le but de générer des modèles prédictifs de toxicités ; 2- Une implémentation de la technologie à grande échelle pour évaluer le bénéfice clinique de son utilisation; 3- Une évaluation comparative avec les approches alternatives d'imagerie fonctionnelle, incluant les coûts-bénéfices.

D'une part, une étude clinique évaluant l'impact du DECT en cancer pulmonaire demeure encore en cours de recrutement et se concentre maintenant sur l'évaluation sériée des changements fonctionnels post-radiques dans le parenchyme pulmonaire. En effet, s'il est essentiel d'évaluer la fonction des organes à risque avant le début de la radiothérapie, la compréhension et la prédiction des atteintes fonctionnelles post-radiques est tout aussi fondamentale pour éclairer les prises de décision prétraitement, et pour permettre une prise en charge plus efficace des séquelles post-radiques. Ce volet sera crucial à la compréhension précise des relations qu'il existe entre la dose de radiothérapie reçue et l'atteinte fonctionnelle anticipée. De plus, l'utilisation du DECT étant dose-neutre, son utilisation a été implémentée à large échelle à tous les patients recevant une radiothérapie pulmonaire ou ORL au sein de notre département de radio-oncologie. Cette stratégie a pour objectif d'acquérir rapidement un large échantillon de données qui permettra une validation à grande échelle des trouvailles présentées dans ce mémoire. Finalement, il restera à déterminer comment la technologie du DECT/DSCT se compare aux technologies d'imagerie émergentes, notamment à l'IRM anatomique et fonctionnel (diffusion et perfusion), et aux radiotraceurs prometteurs utilisés en tomographie par émission de positrons. Alors que ces diverses technologies deviennent rapidement très accessibles en clinique, une comparaison de la performance de chacune de ces modalités, de même qu'une judicieuse estimation de leurs couts-bénéfices seront incontournables dans les années à venir.

13 CONCLUSION GÉNÉRALE

L'utilisation du DECT/DSCT offre de multiples possibilités d'améliorer la précision des traitements de radiothérapie tout en s'intégrant facilement dans le flux de travail actuel de la planification des traitements. Les résultats de nos travaux centrés sur 3 stratégies démontrent que le DECT/DSCT a le potentiel de jouer un rôle important à divers niveaux dans la personnalisation de la planification des traitements radiothérapie: 1) comme bio-marqueurs pour l'évaluation de la fonction des tissus sains; 2) pour la détermination personnalisée du mouvement cardiaque; et 3) comme bio-marqueurs pour la prédiction de l'agressivité tumoral. Dans les prochaines années, le rôle du DECT/DSCT continuera de croitre en radio-oncologie en raison de l'information supplémentaire qu'il offre, à aucun ou faible coût en terme d'irradiation supplémentaire, par rapport au CT à énergie simple. En effet, l'information fonctionnelle qu'il génère, sans nécessiter d'examen supplémentaire, facilitera la généralisation de son intégration à grande échelle en radiothérapie. Les applications proposées dans le cadre de ce projet ont été conduites dans le contexte d'étude de phase I-II ayant pour but de démontrer la faisabilité des méthodes proposées, et d'explorer les bénéfices cliniques ou dosimétriques de l'utilisation du DECT/DSCT en radiothérapie. Des évaluations à plus grande échelle, mesurant le bénéfice clinique de l'intégration de ces applications sur de larges échantillons de patients sont nécessaires et sont actuellement en cours. Finalement, l'accumulation de riches données quantitatives provenant du DECT/DSCT (que ce soit des cartographies d'iode, des reconstructions mono-énergétiques ou de l'imagerie cardiaque) sera une opportunité de générer des modèles prédictifs de toxicités ou de contrôle tumoraux dans le contexte des développements actuels en *radiomique* et en méthodes d'apprentissage profond (*deep learning*) en imagerie médicale.

14 BIBLIOGRAPHIE

1. Jaffray DA. Image-guided radiotherapy: from current concept to future perspectives. Nature reviews Clinical oncology. 2012;9(12):688-99.
2. Bucci MK, Bevan A, Roach M, 3rd. Advances in radiation therapy: conventional to 3D, to IMRT, to 4D, and beyond. CA: a cancer journal for clinicians. 2005;55(2):117-34.
3. Ree AH, Redalen KR. Personalized radiotherapy: concepts, biomarkers and trial design. The British journal of radiology. 2015;88(1051):20150009.
4. Lallemand F, Lakosi F, Hustinx R, Withofs N, Meunier P, Tshibanda L, et al. [Functional imaging and radiotherapy]. Revue medicale de Liege. 2014;69 Suppl 1:20-8.
5. Subesinghe M, Scarsbrook AF, Sourbron S, Wilson DJ, McDermott G, Speight R, et al. Alterations in anatomic and functional imaging parameters with repeated FDG PET-CT and MRI during radiotherapy for head and neck cancer: a pilot study. BMC cancer. 2015;15:137.
6. Petrillo A, Fusco R, Petrillo M, Granata V, Bianco F, Di Marzo M, et al. DCE-MRI time-intensity curve visual inspection to assess pathological response after neoadjuvant therapy in locally advanced rectal cancer. Japanese journal of radiology. 2018.
7. Verma V, Choi JI, Sawant A, Gullapalli RP, Chen W, Alavi A, et al. Use of PET and Other Functional Imaging to Guide Target Delineation in Radiation Oncology. Seminars in radiation oncology. 2018;28(3):171-7.
8. Zhang Y, Ou D, Gu Y, He X, Peng W. Evaluation of Salivary Gland Function Using Diffusion-Weighted Magnetic Resonance Imaging for Follow-Up of Radiation-Induced Xerostomia. Korean journal of radiology. 2018;19(4):758-66.
9. Faught AM, Olsen L, Schubert L, Rusthoven C, Castillo E, Castillo R, et al. Functional-guided radiotherapy using knowledge-based planning. Radiotherapy and oncology : journal of the European Society for Therapeutic Radiology and Oncology. 2018.
10. Bane O, Wagner M, Zhang JL, Dyvorne HA, Orton M, Rusinek H, et al. Assessment of renal function using intravoxel incoherent motion diffusion-weighted imaging and dynamic contrast-enhanced MRI. Journal of magnetic resonance imaging : JMRI. 2016;44(2):317-26.
11. Yoganathan SA, Maria Das KJ, Agarwal A, Kumar S. Magnitude, Impact, and Management of Respiration-induced Target Motion in Radiotherapy Treatment: A Comprehensive Review. Journal of medical physics. 2017;42(3):101-15.
12. Glitzner M, Crijns SP, de Senneville BD, Kontaxis C, Prins FM, Lagendijk JJ, et al. On-line MR imaging for dose validation of abdominal radiotherapy. Physics in medicine and biology. 2015;60(22):8869-83.
13. Schmidt ML, Hoffmann L, Knap MM, Rasmussen TR, Folkersen BH, Toftegaard J, et al. Cardiac and respiration induced motion of mediastinal lymph node targets in lung cancer patients throughout the radiotherapy treatment course. Radiotherapy and oncology : journal of the European Society for Therapeutic Radiology and Oncology. 2016;121(1):52-8.
14. Johnson TR. Dual-energy CT: general principles. AJR American journal of roentgenology. 2012;199(5 Suppl):S3-8.

15. Petersilka M, Bruder H, Krauss B, Stierstorfer K, Flohr TG. Technical principles of dual source CT. European journal of radiology. 2008;68(3):362-8.
16. Vrtiska TJ, Takahashi N, Fletcher JG, Hartman RP, Yu L, Kawashima A. Genitourinary applications of dual-energy CT. AJR American journal of roentgenology. 2010;194(6):1434-42.
17. Coursey CA, Nelson RC, Boll DT, Paulson EK, Ho LM, Neville AM, et al. Dual-energy multidetector CT: how does it work, what can it tell us, and when can we use it in abdominopelvic imaging? Radiographics : a review publication of the Radiological Society of North America, Inc. 2010;30(4):1037-55.
18. Kaza RK, Platt JF, Cohan RH, Caoili EM, Al-Hawary MM, Wasnik A. Dual-energy CT with single- and dual-source scanners: current applications in evaluating the genitourinary tract. Radiographics : a review publication of the Radiological Society of North America, Inc. 2012;32(2):353-69.
19. Johnson TR, Krauss B, Sedlmair M, Grasruck M, Bruder H, Morhard D, et al. Material differentiation by dual energy CT: initial experience. European radiology. 2007;17(6):1510-7.
20. Achenbach S, Ropers D, Kuettner A, Flohr T, Ohnesorge B, Bruder H, et al. Contrast-enhanced coronary artery visualization by dual-source computed tomography--initial experience. European journal of radiology. 2006;57(3):331-5.
21. Flohr TG, McCollough CH, Bruder H, Petersilka M, Gruber K, Suss C, et al. First performance evaluation of a dual-source CT (DSCT) system. European radiology. 2006;16(2):256-68.
22. Stolzmann P, Leschka S, Scheffel H, Krauss T, Desbiolles L, Plass A, et al. Dual-source CT in step-and-shoot mode: noninvasive coronary angiography with low radiation dose. Radiology. 2008;249(1):71-80.
23. Stolzmann P, Scheffel H, Schertler T, Frauenfelder T, Leschka S, Husmann L, et al. Radiation dose estimates in dual-source computed tomography coronary angiography. European radiology. 2008;18(3):592-9.
24. Schwarz F, Ruzsics B, Schoepf UJ, Bastarrika G, Chiaramida SA, Abro JA, et al. Dual-energy CT of the heart--principles and protocols. European journal of radiology. 2008;68(3):423-33.
25. Ruzsics B, Geyer LL, Silverman JR, Krazinski AW, Schoepf UJ. Dual Energy CT of the Heart: Current Status and Future Applications. Current Cardiovascular Imaging Reports. 2013;6(3):228-39.
26. Vliegenthart R, Pelgrim GJ, Ebersberger U, Rowe GW, Oudkerk M, Schoepf UJ. Dual-energy CT of the heart. AJR American journal of roentgenology. 2012;199(5 Suppl):S54-63.
27. Lei Z, Gu J, Fu Q, Shi H, Xu H, Han P, et al. The diagnostic evaluation of dual-source CT (DSCT) in the diagnosis of coronary artery stenoses. Pakistan journal of medical sciences. 2013;29(1):107-11.
28. Bruder HP, M. ; Mehldau, H. ; Heidinger, W. ; Allmendinger, T., et al. Flash imaging in dual source CT (DSCT). Proc SPIE 7258, Medical Imaging. 2009;Physics of Medical Imaging, 72580D (March 10, 2009).
29. Hugo GD, Rosu M. Advances in 4D radiation therapy for managing respiration: part I - 4D imaging. Zeitschrift fur medizinische Physik. 2012;22(4):258-71.
30. Brandner ED, Chetty IJ, Giaddui TG, Xiao Y, Huq MS. Motion management strategies and technical issues associated with stereotactic body radiotherapy of thoracic and upper abdominal tumors: A review from NRG oncology. Medical physics. 2017;44(6):2595-612.

31. Hanvey S, McJury M, Tho LM, Glegg M, Thomson M, Grose D, et al. The influence of MRI scan position on patients with oropharyngeal cancer undergoing radical radiotherapy. Radiation oncology (London, England). 2013;8:129.

32. Marks LB, Bentzen SM, Deasy JO, Kong FM, Bradley JD, Vogelius IS, et al. Radiation dose-volume effects in the lung. International journal of radiation oncology, biology, physics. 2010;76(3 Suppl):S70-6.

33. Early Breast Cancer Trialists' Collaborative G, Darby S, McGale P, Correa C, Taylor C, Arriagada R, et al. Effect of radiotherapy after breast-conserving surgery on 10-year recurrence and 15-year breast cancer death: meta-analysis of individual patient data for 10,801 women in 17 randomised trials. Lancet. 2011;378(9804):1707-16.

34. McDonald S, Rubin P, Phillips TL, Marks LB. Injury to the lung from cancer therapy: clinical syndromes, measurable endpoints, and potential scoring systems. International journal of radiation oncology, biology, physics. 1995;31(5):1187-203.

35. Rodrigues G, Lock M, D'Souza D, Yu E, Van Dyk J. Prediction of radiation pneumonitis by dose - volume histogram parameters in lung cancer--a systematic review. Radiotherapy and oncology : journal of the European Society for Therapeutic Radiology and Oncology. 2004;71(2):127-38.

36. Kim TH, Cho KH, Pyo HR, Lee JS, Zo JI, Lee DH, et al. Dose-volumetric parameters for predicting severe radiation pneumonitis after three-dimensional conformal radiation therapy for lung cancer. Radiology. 2005;235(1):208-15.

37. Bradley JD, Hope A, El Naqa I, Apte A, Lindsay PE, Bosch W, et al. A nomogram to predict radiation pneumonitis, derived from a combined analysis of RTOG 9311 and institutional data. International journal of radiation oncology, biology, physics. 2007;69(4):985-92.

38. Loganathan RS, Stover DE, Shi W, Venkatraman E. Prevalence of COPD in women compared to men around the time of diagnosis of primary lung cancer. Chest. 2006;129(5):1305-12.

39. Marks LB, Prosnitz LR. Estimation of normal tissue complication probabilities with three-dimensional technology. International journal of radiation oncology, biology, physics. 1994;28(3):777-9.

40. Ireland RH, Tahir BA, Wild JM, Lee CE, Hatton MQ. Functional Image-guided Radiotherapy Planning for Normal Lung Avoidance. Clinical oncology (Royal College of Radiologists (Great Britain)). 2016;28(11):695-707.

41. Kumar AM, Parker JA. Ventilation/perfusion scintigraphy. Emergency medicine clinics of North America. 2001;19(4):957-73.

42. Bauman G, Scholz A, Rivoire J, Terekhov M, Friedrich J, de Oliveira A, et al. Lung ventilation- and perfusion-weighted Fourier decomposition magnetic resonance imaging: in vivo validation with hyperpolarized 3He and dynamic contrast-enhanced MRI. Magnetic resonance in medicine. 2013;69(1):229-37.

43. Lan F, Jeudy J, Senan S, van Sornsen de Koste JR, D'Souza W, Tseng HH, et al. Should regional ventilation function be considered during radiation treatment planning to prevent radiation-induced complications? Medical physics. 2016;43(9):5072.

44. Vinogradskiy YY, Castillo R, Castillo E, Chandler A, Martel MK, Guerrero T. Use of weekly 4DCT-based ventilation maps to quantify changes in lung function for patients undergoing radiation therapy. Medical physics. 2012;39(1):289-98.

45. Yamamoto T, Kabus S, Lorenz C, Mittra E, Hong JC, Chung M, et al. Pulmonary ventilation imaging based on 4-dimensional computed tomography: comparison with pulmonary function tests and SPECT ventilation images. International journal of radiation oncology, biology, physics. 2014;90(2):414-22.
46. Siva S, Thomas R, Callahan J, Hardcastle N, Pham D, Kron T, et al. High-resolution pulmonary ventilation and perfusion PET/CT allows for functionally adapted intensity modulated radiotherapy in lung cancer. Radiotherapy and oncology : journal of the European Society for Therapeutic Radiology and Oncology. 2015;115(2):157-62.
47. Kerl JM, Lehnert T, Schell B, Bodelle B, Beeres M, Jacobi V, et al. Intravenous contrast material administration at high-pitch dual-source CT pulmonary angiography: test bolus versus bolus-tracking technique. European journal of radiology. 2012;81(10):2887-91.
48. Delbeke D, Coleman RE, Guiberteau MJ, Brown ML, Royal HD, Siegel BA, et al. Procedure Guideline for SPECT/CT Imaging 1.0. Journal of nuclear medicine : official publication, Society of Nuclear Medicine. 2006;47(7):1227-34.
49. Lapointe A, A. L, H. B, J-F. C, S. B, H. B. Robust quantitative contrast-enhanced dual-energy CT for radiotherapy applications. Unpublished results. 2017.
50. Lapointe A, Bahig H, Blais D, Bouchard H, Filion E, Carrier J-F, et al. Assessing lung function using contrast-enhanced dual energy computed tomography for potential applications in radiation therapy. Unpublished results. 2017.
51. Landry G, Gaudreault M, van Elmpt W, Wildberger JE, Verhaegen F. Improved dose calculation accuracy for low energy brachytherapy by optimizing dual energy CT imaging protocols for noise reduction using sinogram affirmed iterative reconstruction. Zeitschrift fur medizinische Physik. 2016;26(1):75-87.
52. Hunemohr N, Paganetti H, Greilich S, Jakel O, Seco J. Tissue decomposition from dual energy CT data for MC based dose calculation in particle therapy. Medical physics. 2014;41(6):061714.
53. Bourque AE, Carrier JF, Bouchard H. A stoichiometric calibration method for dual energy computed tomography. Physics in medicine and biology. 2014;59(8):2059-88.
54. Mangold S, Gatidis S, Luz O, Konig B, Schabel C, Bongers MN, et al. Single-source dual-energy computed tomography: use of monoenergetic extrapolation for a reduction of metal artifacts. Investigative radiology. 2014;49(12):788-93.
55. Wichmann JL, Noske EM, Kraft J, Burck I, Wagenblast J, Eckardt A, et al. Virtual monoenergetic dual-energy computed tomography: optimization of kiloelectron volt settings in head and neck cancer. Investigative radiology. 2014;49(11):735-41.
56. Toepker M, Czerny C, Ringl H, Fruehwald-Pallamar J, Wolf F, Weber M, et al. Can dual-energy CT improve the assessment of tumor margins in oral cancer? Oral oncology. 2014;50(3):221-7.
57. Ferda J, Ferdova E, Mirka H, Baxa J, Bednarova A, Flohr T, et al. Pulmonary imaging using dual-energy CT, a role of the assessment of iodine and air distribution. European journal of radiology. 2011;77(2):287-93.
58. Washko GR, Hoffman E, Reilly JJ. Radiographic evaluation of the potential lung volume reduction surgery candidate. Proceedings of the American Thoracic Society. 2008;5(4):421-6.
59. Cederlund K, Hogberg S, Jorfeldt L, Larsen F, Norman M, Rasmussen E, et al. Lung perfusion scintigraphy prior to lung volume reduction surgery. Acta radiologica (Stockholm, Sweden : 1987). 2003;44(3):246-51.

60. Wyser C, Stulz P, Soler M, Tamm M, Muller-Brand J, Habicht J, et al. Prospective evaluation of an algorithm for the functional assessment of lung resection candidates. American journal of respiratory and critical care medicine. 1999;159(5 Pt 1):1450-6.
61. Imaeda T, Kanematsu M, Asada S, Seki M, Matsui E, Doi H, et al. Prediction of pulmonary function after resection of primary lung cancer. Utility of inhalation-perfusion SPECT imaging. Clinical nuclear medicine. 1995;20(9):792-9.
62. Giordano A, Calcagni ML, Meduri G, Valente S, Galli G. Perfusion lung scintigraphy for the prediction of postlobectomy residual pulmonary function. Chest. 1997;111(6):1542-7.
63. Bauer RW, Frellesen C, Renker M, Schell B, Lehnert T, Ackermann H, et al. Dual energy CT pulmonary blood volume assessment in acute pulmonary embolism - correlation with D-dimer level, right heart strain and clinical outcome. European radiology. 2011;21(9):1914-21.
64. Pontana F, Faivre JB, Remy-Jardin M, Flohr T, Schmidt B, Tacelli N, et al. Lung perfusion with dual-energy multidetector-row CT (MDCT): feasibility for the evaluation of acute pulmonary embolism in 117 consecutive patients. Academic radiology. 2008;15(12):1494-504.
65. Chae EJ, Seo JB, Jang YM, Krauss B, Lee CW, Lee HJ, et al. Dual-energy CT for assessment of the severity of acute pulmonary embolism: pulmonary perfusion defect score compared with CT angiographic obstruction score and right ventricular/left ventricular diameter ratio. AJR American journal of roentgenology. 2010;194(3):604-10.
66. Meysman M, Everaert H, Buls N, Nieboer K, de Mey J. Comparison of ventilation-perfusion single-photon emission computed tomography (V/Q SPECT) versus dual-energy CT perfusion and angiography (DECT) after 6 months of pulmonary embolism (PE) treatment. European journal of radiology. 2015;84(9):1816-9.
67. Cai XR, Feng YZ, Qiu L, Xian ZH, Yang WC, Mo XK, et al. Iodine Distribution Map in Dual-Energy Computed Tomography Pulmonary Artery Imaging with Rapid kVp Switching for the Diagnostic Analysis and Quantitative Evaluation of Acute Pulmonary Embolism. Academic radiology. 2015;22(6):743-51.
68. Pansini V, Remy-Jardin M, Faivre JB, Schmidt B, Dejardin-Bothelo A, Perez T, et al. Assessment of lobar perfusion in smokers according to the presence and severity of emphysema: preliminary experience with dual-energy CT angiography. European radiology. 2009;19(12):2834-43.
69. Moon JW, Bae JP, Lee HY, Kim N, Chung MP, Park HY, et al. Perfusion- and pattern-based quantitative CT indexes using contrast-enhanced dual-energy computed tomography in diffuse interstitial lung disease: relationships with physiologic impairment and prediction of prognosis. European radiology. 2016;26(5):1368-77.
70. Chae EJ, Kim N, Seo JB, Park JY, Song JW, Lee HJ, et al. Prediction of postoperative lung function in patients undergoing lung resection: dual-energy perfusion computed tomography versus perfusion scintigraphy. Investigative radiology. 2013;48(8):622-7.
71. Shioyama Y, Jang SY, Liu HH, Guerrero T, Wang X, Gayed IW, et al. Preserving functional lung using perfusion imaging and intensity-modulated radiation therapy for advanced-stage non-small cell lung cancer. International journal of radiation oncology, biology, physics. 2007;68(5):1349-58.
72. Yaremko BP, Guerrero TM, Noyola-Martinez J, Guerra R, Lege DG, Nguyen LT, et al. Reduction of normal lung irradiation in locally advanced non-small-cell lung cancer patients,

using ventilation images for functional avoidance. International journal of radiation oncology, biology, physics. 2007;68(2):562-71.

73. Hodge CW, Tome WA, Fain SB, Bentzen SM, Mehta MP. On the use of hyperpolarized helium MRI for conformal avoidance lung radiotherapy. Medical dosimetry : official journal of the American Association of Medical Dosimetrists. 2010;35(4):297-303.

74. Ireland RH, Bragg CM, McJury M, Woodhouse N, Fichele S, van Beek EJ, et al. Feasibility of image registration and intensity-modulated radiotherapy planning with hyperpolarized helium-3 magnetic resonance imaging for non-small-cell lung cancer. International journal of radiation oncology, biology, physics. 2007;68(1):273-81.

75. Fink C, Puderbach M, Bock M, Lodemann KP, Zuna I, Schmahl A, et al. Regional lung perfusion: assessment with partially parallel three-dimensional MR imaging. Radiology. 2004;231(1):175-84.

76. Jang YM, Oh YM, Seo JB, Kim N, Chae EJ, Lee YK, et al. Quantitatively assessed dynamic contrast-enhanced magnetic resonance imaging in patients with chronic obstructive pulmonary disease: correlation of perfusion parameters with pulmonary function test and quantitative computed tomography. Investigative radiology. 2008;43(6):403-10.

77. Ding K, Bayouth JE, Buatti JM, Christensen GE, Reinhardt JM. 4DCT-based measurement of changes in pulmonary function following a course of radiation therapy. Medical physics. 2010;37(3):1261-72.

78. Ohno Y, Seki S, Koyama H, Yoshikawa T, Matsumoto S, Takenaka D, et al. 3D ECG- and respiratory-gated non-contrast-enhanced (CE) perfusion MRI for postoperative lung function prediction in non-small-cell lung cancer patients: A comparison with thin-section quantitative computed tomography, dynamic CE-perfusion MRI, and perfusion scan. Journal of magnetic resonance imaging : JMRI. 2015;42(2):340-53.

79. Yamamoto T, Kabus S, von Berg J, Lorenz C, Keall PJ. Impact of four-dimensional computed tomography pulmonary ventilation imaging-based functional avoidance for lung cancer radiotherapy. International journal of radiation oncology, biology, physics. 2011;79(1):279-88.

80. Wang R, Zhang S, Yu H, Lin S, Zhang G, Tang R, et al. Optimal beam arrangement for pulmonary ventilation image-guided intensity-modulated radiotherapy for lung cancer. Radiation oncology (London, England). 2014;9:184.

81. Kimura T, Nishibuchi I, Murakami Y, Kenjo M, Kaneyasu Y, Nagata Y. Functional image-guided radiotherapy planning in respiratory-gated intensity-modulated radiotherapy for lung cancer patients with chronic obstructive pulmonary disease. International journal of radiation oncology, biology, physics. 2012;82(4):e663-70.

82. McGuire SM, Marks LB, Yin FF, Das SK. A methodology for selecting the beam arrangement to reduce the intensity-modulated radiation therapy (IMRT) dose to the SPECT-defined functioning lung. Physics in medicine and biology. 2010;55(2):403-16.

83. St-Hilaire J, Lavoie C, Dagnault A, Beaulieu F, Morin F, Beaulieu L, et al. Functional avoidance of lung in plan optimization with an aperture-based inverse planning system. Radiotherapy and oncology : journal of the European Society for Therapeutic Radiology and Oncology. 2011;100(3):390-5.

84. Bates EL, Bragg CM, Wild JM, Hatton MQ, Ireland RH. Functional image-based radiotherapy planning for non-small cell lung cancer: A simulation study. Radiotherapy and oncology : journal of the European Society for Therapeutic Radiology and Oncology. 2009;93(1):32-6.

85. De Bari B, Deantonio L, Bourhis J, Prior JO, Ozsahin M. Should we include SPECT lung perfusion in radiotherapy treatment plans of thoracic targets? Evidences from the literature. Critical reviews in oncology/hematology. 2016;102:111-7.

86. Farr KP, Kallehauge JF, Moller DS, Khalil AA, Kramer S, Bluhme H, et al. Inclusion of functional information from perfusion SPECT improves predictive value of dose-volume parameters in lung toxicity outcome after radiotherapy for non-small cell lung cancer: A prospective study. Radiotherapy and oncology : journal of the European Society for Therapeutic Radiology and Oncology. 2015;117(1):9-16.

87. Kimura T, Doi Y, Nakashima T, Imano N, Kawabata H, Nishibuchi I, et al. Combined Ventilation and Perfusion Imaging Correlates With the Dosimetric Parameters of Radiation Pneumonitis in Radiation Therapy Planning for Lung Cancer. International journal of radiation oncology, biology, physics. 2015;93(4):778-87.

88. Young RP, Hopkins RJ, Christmas T, Black PN, Metcalf P, Gamble GD. COPD prevalence is increased in lung cancer, independent of age, sex and smoking history. The European respiratory journal. 2009;34(2):380-6.

89. Clarke M, Collins R, Darby S, Davies C, Elphinstone P, Evans V, et al. Effects of radiotherapy and of differences in the extent of surgery for early breast cancer on local recurrence and 15-year survival: an overview of the randomised trials. Lancet (London, England). 2005;366(9503):2087-106.

90. Darby SC, Ewertz M, McGale P, Bennet AM, Blom-Goldman U, Bronnum D, et al. Risk of ischemic heart disease in women after radiotherapy for breast cancer. The New England journal of medicine. 2013;368(11):987-98.

91. Prosnitz RG, Chen YH, Marks LB. Cardiac toxicity following thoracic radiation. Seminars in oncology. 2005;32(2 Suppl 3):S71-80.

92. Darby S, McGale P, Correa C, Taylor C, Arriagada R, Clarke M, et al. Effect of radiotherapy after breast-conserving surgery on 10-year recurrence and 15-year breast cancer death: meta-analysis of individual patient data for 10,801 women in 17 randomised trials. Lancet. 2011;378(9804):1707-16.

93. Borger JH, Hooning MJ, Boersma LJ, Snijders-Keilholz A, Aleman BM, Lintzen E, et al. Cardiotoxic effects of tangential breast irradiation in early breast cancer patients: the role of irradiated heart volume. International journal of radiation oncology, biology, physics. 2007;69(4):1131-8.

94. Schultz-Hector S, Trott KR. Radiation-induced cardiovascular diseases: is the epidemiologic evidence compatible with the radiobiologic data? International journal of radiation oncology, biology, physics. 2007;67(1):10-8.

95. Taylor CW, Povall JM, McGale P, Nisbet A, Dodwell D, Smith JT, et al. Cardiac dose from tangential breast cancer radiotherapy in the year 2006. International journal of radiation oncology, biology, physics. 2008;72(2):501-7.

96. Gyenes G, Gagliardi G, Lax I, Fornander T, Rutqvist LE. Evaluation of irradiated heart volumes in stage I breast cancer patients treated with postoperative adjuvant radiotherapy. Journal of clinical oncology : official journal of the American Society of Clinical Oncology. 1997;15(4):1348-53.

97. Hurkmans CW, Cho BC, Damen E, Zijp L, Mijnheer BJ. Reduction of cardiac and lung complication probabilities after breast irradiation using conformal radiotherapy with or without intensity modulation. Radiotherapy and oncology : journal of the European Society for Therapeutic Radiology and Oncology. 2002;62(2):163-71.

98. Schubert LK, Gondi V, Sengbusch E, Westerly DC, Soisson ET, Paliwal BR, et al. Dosimetric comparison of left-sided whole breast irradiation with 3DCRT, forward-planned IMRT, inverse-planned IMRT, helical tomotherapy, and topotherapy. Radiotherapy and oncology : journal of the European Society for Therapeutic Radiology and Oncology. 2011;100(2):241-6.
99. Mast ME, van Kempen-Harteveld L, Heijenbrok MW, Kalidien Y, Rozema H, Jansen WP, et al. Left-sided breast cancer radiotherapy with and without breath-hold: does IMRT reduce the cardiac dose even further? Radiotherapy and oncology : journal of the European Society for Therapeutic Radiology and Oncology. 2013;108(2):248-53.
100. Hui SK, Das RK, Kapatoes J, Oliviera G, Becker S, Odau H, et al. Helical tomotherapy as a means of delivering accelerated partial breast irradiation. Technology in cancer research & treatment. 2004;3(6):639-46.
101. Jagsi R, Moran JM, Kessler ML, Marsh RB, Balter JM, Pierce LJ. Respiratory motion of the heart and positional reproducibility under active breathing control. International journal of radiation oncology, biology, physics. 2007;68(1):253-8.
102. Korreman SS, Pedersen AN, Aarup LR, Nottrup TJ, Specht L, Nystrom H. Reduction of cardiac and pulmonary complication probabilities after breathing adapted radiotherapy for breast cancer. International journal of radiation oncology, biology, physics. 2006;65(5):1375-80.
103. Hayden AJ, Rains M, Tiver K. Deep inspiration breath hold technique reduces heart dose from radiotherapy for left-sided breast cancer. Journal of medical imaging and radiation oncology. 2012;56(4):464-72.
104. Vikstrom J, Hjelstuen MH, Mjaaland I, Dybvik KI. Cardiac and pulmonary dose reduction for tangentially irradiated breast cancer, utilizing deep inspiration breath-hold with audio-visual guidance, without compromising target coverage. Acta oncologica (Stockholm, Sweden). 2011;50(1):42-50.
105. Bradley JA, Dagan R, Ho MW, Rutenberg M, Morris CG, Li Z, et al. Initial Report of a Prospective Dosimetric and Clinical Feasibility Trial Demonstrates the Potential of Protons to Increase the Therapeutic Ratio in Breast Cancer Compared With Photons. International journal of radiation oncology, biology, physics. 2016;95(1):411-21.
106. Orecchia R, Fossati P, Zurrida S, Krengli M. New frontiers in proton therapy: applications in breast cancer. Current opinion in oncology. 2015;27(6):427-32.
107. Kirby AM, Evans PM, Helyer SJ, Donovan EM, Convery HM, Yarnold JR. A randomised trial of supine versus prone breast radiotherapy (SuPr study): comparing set-up errors and respiratory motion. Radiotherapy and oncology : journal of the European Society for Therapeutic Radiology and Oncology. 2011;100(2):221-6.
108. Kirby AM, Evans PM, Donovan EM, Convery HM, Haviland JS, Yarnold JR. Prone versus supine positioning for whole and partial-breast radiotherapy: a comparison of non-target tissue dosimetry. Radiotherapy and oncology : journal of the European Society for Therapeutic Radiology and Oncology. 2010;96(2):178-84.
109. Nieder C, Schill S, Kneschaurek P, Molls M. Influence of different treatment techniques on radiation dose to the LAD coronary artery. Radiation oncology (London, England). 2007;2:20.
110. Nilsson G, Holmberg L, Garmo H, Duvernoy O, Sjogren I, Lagerqvist B, et al. Distribution of coronary artery stenosis after radiation for breast cancer. Journal of clinical oncology : official journal of the American Society of Clinical Oncology. 2012;30(4):380-6.

111. Correa CR, Litt HI, Hwang WT, Ferrari VA, Solin LJ, Harris EE. Coronary artery findings after left-sided compared with right-sided radiation treatment for early-stage breast cancer. Journal of clinical oncology : official journal of the American Society of Clinical Oncology. 2007;25(21):3031-7.
112. Nilsson G, Witt Nystrom P, Isacsson U, Garmo H, Duvernoy O, Sjogren I, et al. Radiation dose distribution in coronary arteries in breast cancer radiotherapy. Acta oncologica (Stockholm, Sweden). 2016;55(8):959-63.
113. Lee J, Hua KL, Hsu SM, Lin JB, Lee CH, Lu KW, et al. Development of delineation for the left anterior descending coronary artery region in left breast cancer radiotherapy: An optimized organ at risk. Radiotherapy and oncology : journal of the European Society for Therapeutic Radiology and Oncology. 2017;122(3):423-30.
114. Aznar MC, Korreman SS, Pedersen AN, Persson GF, Josipovic M, Specht L. Evaluation of dose to cardiac structures during breast irradiation. The British journal of radiology. 2011;84(1004):743-6.
115. Ding Z, Friedman MH. Dynamics of human coronary arterial motion and its potential role in coronary atherogenesis. Journal of biomechanical engineering. 2000;122(5):488-92.
116. Vennarini S, Fournier-Bidoz N, Aristei C, de Almeida CE, Servois V, Campana F, et al. Visualisation of the left anterior descending coronary artery on CT images used for breast radiotherapy planning. The British journal of radiology. 2013;86(1025):20120643.
117. White BM, Vennarini S, Lin L, Freedman G, Santhanam A, Low DA, et al. Accuracy of routine treatment planning 4-dimensional and deep-inspiration breath-hold computed tomography delineation of the left anterior descending artery in radiation therapy. International journal of radiation oncology, biology, physics. 2015;91(4):825-31.
118. Wang X, Pan T, Pinnix C, Zhang SX, Salehpour M, Sun TL, et al. Cardiac motion during deep-inspiration breath-hold: implications for breast cancer radiotherapy. International journal of radiation oncology, biology, physics. 2012;82(2):708-14.
119. Mathieu D, Martel C, Campeau MP, Filion E, Roberge D, Bahig H, et al. Accuracy of Breath-hold CT in Treatment Planning for Lung Stereotactic Ablative Radiotherapy. Cureus. 2014;6(12):e236.
120. Nguyen NT, Charron G, Blais D, Roberge D. Turn down the noise--a blinded evaluation of iterative image reconstruction in radiation therapy computed tomography simulation. Practical radiation oncology. 2015;5(4):e393-400.
121. Feng M, Moran JM, Koelling T, Chughtai A, Chan JL, Freedman L, et al. Development and validation of a heart atlas to study cardiac exposure to radiation following treatment for breast cancer. International journal of radiation oncology, biology, physics. 2011;79(1):10-8.
122. Kini S, Bis KG, Weaver L. Normal and variant coronary arterial and venous anatomy on high-resolution CT angiography. AJR American journal of roentgenology. 2007;188(6):1665-74.
123. Kim WW, Lee CH, Goo JM, Park SJ, Kim JH, Park EA, et al. Xenon-enhanced dual-energy CT of patients with asthma: dynamic ventilation changes after methacholine and salbutamol inhalation. AJR American journal of roentgenology. 2012;199(5):975-81.
124. Austen WG, Edwards JE, Frye RL, Gensini GG, Gott VL, Griffith LS, et al. A reporting system on patients evaluated for coronary artery disease. Report of the Ad Hoc Committee for Grading of Coronary Artery Disease, Council on Cardiovascular Surgery, American Heart Association. Circulation. 1975;51(4 Suppl):5-40.

125. Oncel D, Oncel G, Tastan A. Effectiveness of dual-source CT coronary angiography for the evaluation of coronary artery disease in patients with atrial fibrillation: initial experience. Radiology. 2007;245(3):703-11.
126. Nakatani S. Left ventricular rotation and twist: why should we learn? Journal of cardiovascular ultrasound. 2011;19(1):1-6.
127. Stewart JR, Fajardo LF, Gillette SM, Constine LS. Radiation injury to the heart. International journal of radiation oncology, biology, physics. 1995;31(5):1205-11.
128. Gagliardi G, Constine LS, Moiseenko V, Correa C, Pierce LJ, Allen AM, et al. Radiation dose-volume effects in the heart. International journal of radiation oncology, biology, physics. 2010;76(3 Suppl):S77-85.
129. M.V. DDDATGPADSDA. Clinically relevant morphometric analysis of left coronary artery. Int J Biol Med Res 0. 2012;3(1): :1327-133.
130. Wennstig AK, Garmo H, Hallstrom P, Nystrom PW, Edlund P, Blomqvist C, et al. Inter-observer variation in delineating the coronary arteries as organs at risk. Radiotherapy and oncology : journal of the European Society for Therapeutic Radiology and Oncology. 2017;122(1):72-8.
131. Betgen A, Alderliesten T, Sonke JJ, van Vliet-Vroegindeweij C, Bartelink H, Remeijer P. Assessment of set-up variability during deep inspiration breath hold radiotherapy for breast cancer patients by 3D-surface imaging. Radiotherapy and oncology : journal of the European Society for Therapeutic Radiology and Oncology. 2013;106(2):225-30.
132. Lutz CM, Poulsen PR, Fledelius W, Offersen BV, Thomsen MS. Setup error and motion during deep inspiration breath-hold breast radiotherapy measured with continuous portal imaging. Acta oncologica (Stockholm, Sweden). 2016;55(2):193-200.
133. Sung K, Lee KC, Lee SH, Ahn SH, Lee SH, Choi J. Cardiac dose reduction with breathing adapted radiotherapy using self respiration monitoring system for left-sided breast cancer. Radiation oncology journal. 2014;32(2):84-94.
134. Duane F, Aznar MC, Bartlett F, Cutter DJ, Darby SC, Jagsi R, et al. A cardiac contouring atlas for radiotherapy. Radiotherapy and oncology : journal of the European Society for Therapeutic Radiology and Oncology. 2017;122(3):416-22.
135. Galiwango P, Chow BJ. Cardiac computed tomography and risks of radiation exposure: how low can we go? The Canadian journal of cardiology. 2011;27(5):536-7.
136. Natarajan MK, Paul N, Mercuri M, Waller EJ, Leipsic J, Traboulsi M, et al. Canadian Cardiovascular Society position statement on radiation exposure from cardiac imaging and interventional procedures. The Canadian journal of cardiology. 2013;29(11):1361-8.
137. van Elmpt W, Landry G, Das M, Verhaegen F. Dual energy CT in radiotherapy: Current applications and future outlook. Radiother Oncol. 2016;119(1):137-44.
138. Naderi S, Wang Y, Miller AL, Rodriguez F, Chung MK, Radford MJ, et al. The impact of age on the epidemiology of atrial fibrillation hospitalizations. Am J Med. 2014;127(2):158 e1-7.
139. Kistler PM, Sanders P, Fynn SP, Stevenson IH, Spence SJ, Vohra JK, et al. Electrophysiologic and electroanatomic changes in the human atrium associated with age. J Am Coll Cardiol. 2004;44(1):109-16.
140. Haissaguerre M, Jais P, Shah DC, Takahashi A, Hocini M, Quiniou G, et al. Spontaneous initiation of atrial fibrillation by ectopic beats originating in the pulmonary veins. N Engl J Med. 1998;339(10):659-66.

141. Takigawa M, Takahashi A, Kuwahara T, Okubo K, Takahashi Y, Watari Y, et al. Long-term follow-up after catheter ablation of paroxysmal atrial fibrillation: the incidence of recurrence and progression of atrial fibrillation. Circ Arrhythm Electrophysiol. 2014;7(2):267-73.
142. Calkins H, Kuck KH, Cappato R, Brugada J, Camm AJ, Chen SA, et al. 2012 HRS/EHRA/ECAS expert consensus statement on catheter and surgical ablation of atrial fibrillation: recommendations for patient selection, procedural techniques, patient management and follow-up, definitions, endpoints, and research trial design: a report of the Heart Rhythm Society (HRS) Task Force on Catheter and Surgical Ablation of Atrial Fibrillation. Developed in partnership with the European Heart Rhythm Association (EHRA), a registered branch of the European Society of Cardiology (ESC) and the European Cardiac Arrhythmia Society (ECAS); and in collaboration with the American College of Cardiology (ACC), American Heart Association (AHA), the Asia Pacific Heart Rhythm Society (APHRS), and the Society of Thoracic Surgeons (STS). Endorsed by the governing bodies of the American College of Cardiology Foundation, the American Heart Association, the European Cardiac Arrhythmia Society, the European Heart Rhythm Association, the Society of Thoracic Surgeons, the Asia Pacific Heart Rhythm Society, and the Heart Rhythm Society. Heart Rhythm. 2012;9(4):632-96 e21.
143. Deshmukh A, Patel NJ, Pant S, Shah N, Chothani A, Mehta K, et al. In-hospital complications associated with catheter ablation of atrial fibrillation in the United States between 2000 and 2010: analysis of 93 801 procedures. Circulation. 2013;128(19):2104-12.
144. Sharma A, Wong D, Weidlich G, Fogarty T, Jack A, Sumanaweera T, et al. Noninvasive stereotactic radiosurgery (CyberHeart) for creation of ablation lesions in the atrium. Heart Rhythm. 2010;7(6):802-10.
145. Maguire P.J. GE, Jack A.B., Zei P., Al-Ahmad A., Fajardo L., Ladich E., and Takeda P. Cardiac radiosurgery (CyberHeart™) for treatment of arrhythmia: Physiologic and histopathologic correlation in the porcine model. Cureus 3(8). 2011: e32–e49.
146. Gardner EA, Sumanaweera TS, Blanck O, Iwamura AK, Steel JP, Dieterich S, et al. In vivo dose measurement using TLDs and MOSFET dosimeters for cardiac radiosurgery. J Appl Clin Med Phys. 2012;13(3):3745.
147. Blanck O, Bode F, Gebhard M, Hunold P, Brandt S, Bruder R, et al. Dose-escalation study for cardiac radiosurgery in a porcine model. Int J Radiat Oncol Biol Phys. 2014;89(3):590-8.
148. Bode F, Blanck O, Gebhard M, Hunold P, Grossherr M, Brandt S, et al. Pulmonary vein isolation by radiosurgery: implications for non-invasive treatment of atrial fibrillation. Europace. 2015;17(12):1868-74.
149. Ipsen S, Blanck O, Oborn B, Bode F, Liney G, Hunold P, et al. Radiotherapy beyond cancer: target localization in real-time MRI and treatment planning for cardiac radiosurgery. Med Phys. 2014;41(12):120702.
150. Rolfes CD, Howard SA, Goff RP, Iaizzo PA. Cardiac remodeling as a consequence of atrial fibrillation: An anatomical study of perfusion-fixed human heart specimens. J Geriatr Cardiol. 2011;8(3):141-6.
151. Rettmann ME, Holmes DR, 3rd, Johnson SB, Lehmann HI, Robb RA, Packer DL. Analysis of Left Atrial Respiratory and Cardiac Motion for Cardiac Ablation Therapy. Proc SPIE Int Soc Opt Eng. 2015;9415.

152. Wang Z, Willett CG, Yin FF. Reduction of organ motion by combined cardiac gating and respiratory gating. Int J Radiat Oncol Biol Phys. 2007;68(1):259-66.
153. Lefebvre JL, Ang KK. Larynx preservation clinical trial design: key issues and recommendations-a consensus panel summary. Int J Radiat Oncol Biol Phys. 2009;73(5):1293-303.
154. Agopian B, Dassonville O, Chamorey E, Poissonnet G, Pierre CS, Peyrade F, et al. [Total pharyngolaryngectomy in the 21st century: indications, oncologic and functional outcomes]. Rev Laryngol Otol Rhinol (Bord). 2011;132(4-5):209-14.
155. Riga M, Chelis L, Danielides V, Vogiatzaki T, Pantazis TL, Pantazis D. Systematic review on T3 laryngeal squamous cell carcinoma; still far from a consensus on the optimal organ preserving treatment. Eur J Surg Oncol. 2017;43(1):20-31.
156. Pulte D, Brenner H. Changes in survival in head and neck cancers in the late 20th and early 21st century: a period analysis. Oncologist. 2010;15(9):994-1001.
157. Siegel RL MK, Jemal A. . Cancer statistics,. CA Cancer J Clin. 2016;66:7–30.
158. Wolf GT, Fisher SG, Hong WK, Hillman R, Spaulding M, Laramore GE, et al. Induction chemotherapy plus radiation compared with surgery plus radiation in patients with advanced laryngeal cancer. N Engl J Med. 1991;324(24):1685-90.
159. Forastiere AA, Goepfert H, Maor M, Pajak TF, Weber R, Morrison W, et al. Concurrent chemotherapy and radiotherapy for organ preservation in advanced laryngeal cancer. The New England journal of medicine. 2003;349(22):2091-8.
160. Lefebvre JL, Andry G, Chevalier D, Luboinski B, Collette L, Traissac L, et al. Laryngeal preservation with induction chemotherapy for hypopharyngeal squamous cell carcinoma: 10-year results of EORTC trial 24891. Ann Oncol. 2012;23(10):2708-14.
161. Forastiere AA, Zhang Q, Weber RS, Maor MH, Goepfert H, Pajak TF, et al. Long-term results of RTOG 91-11: a comparison of three nonsurgical treatment strategies to preserve the larynx in patients with locally advanced larynx cancer. J Clin Oncol. 2013;31(7):845-52.
162. Yabuki K, Shiono O, Komatsu M, Sano D, Nishimura G, Takahashi M, et al. Predictive and prognostic value of metabolic tumor volume (MTV) in patients with laryngeal carcinoma treated by radiotherapy (RT) / concurrent chemoradiotherapy (CCRT). PLoS One. 2015;10(2):e0117924.
163. Preda L, Conte G, Bonello L, Giannitto C, Travaini LL, Raimondi S, et al. Combining standardized uptake value of FDG-PET and apparent diffusion coefficient of DW-MRI improves risk stratification in head and neck squamous cell carcinoma. Eur Radiol. 2016;26(12):4432-41.
164. Grkovski M, Schoder H, Lee NY, Carlin SD, Beattie BJ, Riaz N, et al. Multiparametric Imaging of Tumor Hypoxia and Perfusion with (18)F-Fluoromisonidazole Dynamic PET in Head and Neck Cancer. J Nucl Med. 2017;58(7):1072-80.
165. Bogowicz M, Riesterer O, Stark LS, Studer G, Unkelbach J, Guckenberger M, et al. Comparison of PET and CT radiomics for prediction of local tumor control in head and neck squamous cell carcinoma. Acta Oncol. 2017;56(11):1531-6.
166. Abgral R, Keromnes N, Robin P, Le Roux PY, Bourhis D, Palard X, et al. Prognostic value of volumetric parameters measured by 18F-FDG PET/CT in patients with head and neck squamous cell carcinoma. Eur J Nucl Med Mol Imaging. 2014;41(4):659-67.
167. Dirix P, Vandecaveye V, De Keyzer F, Stroobants S, Hermans R, Nuyts S. Dose painting in radiotherapy for head and neck squamous cell carcinoma: value of repeated

functional imaging with (18)F-FDG PET, (18)F-fluoromisonidazole PET, diffusion-weighted MRI, and dynamic contrast-enhanced MRI. J Nucl Med. 2009;50(7):1020-7.
168. Mortensen LS, Johansen J, Kallehauge J, Primdahl H, Busk M, Lassen P, et al. FAZA PET/CT hypoxia imaging in patients with squamous cell carcinoma of the head and neck treated with radiotherapy: results from the DAHANCA 24 trial. Radiother Oncol. 2012;105(1):14-20.
169. Chawla S, Kim S, Dougherty L, Wang S, Loevner LA, Quon H, et al. Pretreatment diffusion-weighted and dynamic contrast-enhanced MRI for prediction of local treatment response in squamous cell carcinomas of the head and neck. AJR Am J Roentgenol. 2013;200(1):35-43.
170. King AD, Mo FK, Yu KH, Yeung DK, Zhou H, Bhatia KS, et al. Squamous cell carcinoma of the head and neck: diffusion-weighted MR imaging for prediction and monitoring of treatment response. Eur Radiol. 2010;20(9):2213-20.
171. Lambrecht M, Van Calster B, Vandecaveye V, De Keyzer F, Roebben I, Hermans R, et al. Integrating pretreatment diffusion weighted MRI into a multivariable prognostic model for head and neck squamous cell carcinoma. Radiother Oncol. 2014;110(3):429-34.
172. Shukla-Dave A, Lee NY, Jansen JF, Thaler HT, Stambuk HE, Fury MG, et al. Dynamic contrast-enhanced magnetic resonance imaging as a predictor of outcome in head-and-neck squamous cell carcinoma patients with nodal metastases. Int J Radiat Oncol Biol Phys. 2012;82(5):1837-44.
173. Hermans R, Meijerink M, Van den Bogaert W, Rijnders A, Weltens C, Lambin P. Tumor perfusion rate determined noninvasively by dynamic computed tomography predicts outcome in head-and-neck cancer after radiotherapy. Int J Radiat Oncol Biol Phys. 2003;57(5):1351-6.
174. Razek AA, Tawfik AM, Elsorogy LG, Soliman NY. Perfusion CT of head and neck cancer. Eur J Radiol. 2014;83(3):537-44.
175. Ash L, Teknos TN, Gandhi D, Patel S, Mukherji SK. Head and neck squamous cell carcinoma: CT perfusion can help noninvasively predict intratumoral microvessel density. Radiology. 2009;251(2):422-8.
176. Ling S, Deng D, Mo Y, Zhang X, Guan X, Wei Q. Correlations between CT perfusion parameters and vascular endothelial growth factor expression and microvessel density in implanted VX2 lung tumors. Cell Biochem Biophys. 2014;70(1):629-33.
177. Forghani R, Srinivasan A, Forghani B. Advanced Tissue Characterization and Texture Analysis Using Dual-Energy Computed Tomography: Horizons and Emerging Applications. Neuroimaging Clin N Am. 2017;27(3):533-46.
178. Vogl TJ, Schulz B, Bauer RW, Stover T, Sader R, Tawfik AM. Dual-energy CT applications in head and neck imaging. AJR Am J Roentgenol. 2012;199(5 Suppl):S34-9.
179. Miles KA. Tumour angiogenesis and its relation to contrast enhancement on computed tomography: a review. Eur J Radiol. 1999;30(3):198-205.
180. Lalonde A, Bouchard H. A general method to derive tissue parameters for Monte Carlo dose calculation with multi-energy CT. Phys Med Biol. 2016;61(22):8044-69.
181. Issa MR, Samuels SE, Bellile E, Shalabi FL, Eisbruch A, Wolf G. Tumor Volumes and Prognosis in Laryngeal Cancer. Cancers (Basel). 2015;7(4):2236-61.
182. Tawfik AM, Razek AA, Kerl JM, Nour-Eldin NE, Bauer R, Vogl TJ. Comparison of dual-energy CT-derived iodine content and iodine overlay of normal, inflammatory and metastatic squamous cell carcinoma cervical lymph nodes. Eur Radiol. 2014;24(3):574-80.

183. Kuno H, Onaya H, Iwata R, Kobayashi T, Fujii S, Hayashi R, et al. Evaluation of cartilage invasion by laryngeal and hypopharyngeal squamous cell carcinoma with dual-energy CT. Radiology. 2012;265(2):488-96.
184. Schmid-Bindert G, Henzler T, Chu TQ, Meyer M, Nance JW, Jr., Schoepf UJ, et al. Functional imaging of lung cancer using dual energy CT: how does iodine related attenuation correlate with standardized uptake value of 18FDG-PET-CT? European radiology. 2012;22(1):93-103.
185. Mankoff DA, Dunnwald LK, Gralow JR, Ellis GK, Charlop A, Lawton TJ, et al. Blood flow and metabolism in locally advanced breast cancer: relationship to response to therapy. J Nucl Med. 2002;43(4):500-9.
186. Hermans R, Lambin P, Van der Goten A, Van den Bogaert W, Verbist B, Weltens C, et al. Tumoural perfusion as measured by dynamic computed tomography in head and neck carcinoma. Radiother Oncol. 1999;53(2):105-11.
187. Gillies RJ, Schornack PA, Secomb TW, Raghunand N. Causes and effects of heterogeneous perfusion in tumors. Neoplasia. 1999;1(3):197-207.
188. Eschmann SM, Paulsen F, Reimold M, Dittmann H, Welz S, Reischl G, et al. Prognostic impact of hypoxia imaging with 18F-misonidazole PET in non-small cell lung cancer and head and neck cancer before radiotherapy. J Nucl Med. 2005;46(2):253-60.
189. Thorwarth D, Eschmann SM, Scheiderbauer J, Paulsen F, Alber M. Kinetic analysis of dynamic 18F-fluoromisonidazole PET correlates with radiation treatment outcome in head-and-neck cancer. BMC Cancer. 2005;5:152.
190. Lehtio K, Eskola O, Viljanen T, Oikonen V, Gronroos T, Sillanmaki L, et al. Imaging perfusion and hypoxia with PET to predict radiotherapy response in head-and-neck cancer. Int J Radiat Oncol Biol Phys. 2004;59(4):971-82.
191. Hoefling NL, McHugh JB, Light E, Kumar B, Walline H, Prince M, et al. Human papillomavirus, p16, and epidermal growth factor receptor biomarkers and CT perfusion values in head and neck squamous cell carcinoma. AJNR Am J Neuroradiol. 2013;34(5):1062-6, s1-2.
192. Pietsch C, de Galiza Barbosa F, Hullner MW, Schmid DT, Haerle SK, Huber GF, et al. Combined PET/CT-perfusion in patients with head and neck cancers might predict failure after radio-chemotherapy: a proof of concept study. BMC Med Imaging. 2015;15:60.
193. Ljungkvist AS, Bussink J, Rijken PF, Kaanders JH, van der Kogel AJ, Denekamp J. Vascular architecture, hypoxia, and proliferation in first-generation xenografts of human head-and-neck squamous cell carcinomas. Int J Radiat Oncol Biol Phys. 2002;54(1):215-28.
194. Hlatky L, Hahnfeldt P, Folkman J. Clinical application of antiangiogenic therapy: microvessel density, what it does and doesn't tell us. J Natl Cancer Inst. 2002;94(12):883-93.
195. Carmeliet P, Jain RK. Molecular mechanisms and clinical applications of angiogenesis. Nature. 2011;473(7347):298-307.
196. Bisdas S, Spicer K, Rumboldt Z. Whole-tumor perfusion CT parameters and glucose metabolism measurements in head and neck squamous cell carcinomas: a pilot study using combined positron-emission tomography/CT imaging. AJNR Am J Neuroradiol. 2008;29(7):1376-81.
197. Bernstein JM, Homer JJ, West CM. Dynamic contrast-enhanced magnetic resonance imaging biomarkers in head and neck cancer: potential to guide treatment? A systematic review. Oral Oncol. 2014;50(10):963-70.

198. Jackson A, O'Connor JP, Parker GJ, Jayson GC. Imaging tumor vascular heterogeneity and angiogenesis using dynamic contrast-enhanced magnetic resonance imaging. Clin Cancer Res. 2007;13(12):3449-59.

199. Jansen JF, Lu Y, Gupta G, Lee NY, Stambuk HE, Mazaheri Y, et al. Texture analysis on parametric maps derived from dynamic contrast-enhanced magnetic resonance imaging in head and neck cancer. World J Radiol. 2016;8(1):90-7.

200. Thieme SF, Hoegl S, Nikolaou K, Fisahn J, Irlbeck M, Maxien D, et al. Pulmonary ventilation and perfusion imaging with dual-energy CT. European radiology. 2010;20(12):2882-9.

201. Chae EJ, Seo JB, Lee J, Kim N, Goo HW, Lee HJ, et al. Xenon ventilation imaging using dual-energy computed tomography in asthmatics: initial experience. Investigative radiology. 2010;45(6):354-61.

202. Chae EJ, Seo JB, Goo HW, Kim N, Song KS, Lee SD, et al. Xenon ventilation CT with a dual-energy technique of dual-source CT: initial experience. Radiology. 2008;248(2):615-24.

203. Yanagita H, Honda N, Nakayama M, Watanabe W, Shimizu Y, Osada H, et al. Prediction of postoperative pulmonary function: preliminary comparison of single-breath dual-energy xenon CT with three conventional methods. Japanese journal of radiology. 2013;31(6):377-85.

204. Park EA, Goo JM, Park SJ, Lee HJ, Lee CH, Park CM, et al. Chronic obstructive pulmonary disease: quantitative and visual ventilation pattern analysis at xenon ventilation CT performed by using a dual-energy technique. Radiology. 2010;256(3):985-97.

205. Jogi J, Ekberg M, Jonson B, Bozovic G, Bajc M. Ventilation/perfusion SPECT in chronic obstructive pulmonary disease: an evaluation by reference to symptoms, spirometric lung function and emphysema, as assessed with HRCT. European journal of nuclear medicine and molecular imaging. 2011;38(7):1344-52.

206. Bajc M, Markstad H, Jarenback L, Tufvesson E, Bjermer L, Jogi J. Grading obstructive lung disease using tomographic pulmonary scintigraphy in patients with chronic obstructive pulmonary disease (COPD) and long-term smokers. Annals of nuclear medicine. 2015;29(1):91-9.

207. van Dijk LV, Thor M, Steenbakkers R, Apte A, Zhai TT, Borra R, et al. Parotid gland fat related Magnetic Resonance image biomarkers improve prediction of late radiation-induced xerostomia. Radiotherapy and oncology : journal of the European Society for Therapeutic Radiology and Oncology. 2018.

208. Marzi S, Forina C, Marucci L, Giovinazzo G, Giordano C, Piludu F, et al. Early radiation-induced changes evaluated by intravoxel incoherent motion in the major salivary glands. Journal of magnetic resonance imaging : JMRI. 2015;41(4):974-82.

209. Cao Y, Wang H, Johnson TD, Pan C, Hussain H, Balter JM, et al. Prediction of liver function by using magnetic resonance-based portal venous perfusion imaging. International journal of radiation oncology, biology, physics. 2013;85(1):258-63.

210. Patankar K, Low RS, Blakeway D, Ferrari P. Comparison of computer tomographic volumetry versus nuclear split renal function to determine residual renal function after living kidney donation. Acta radiologica (Stockholm, Sweden : 1987). 2014;55(6):753-60.

211. Frennby B, Almen T, Lilja B, Eriksson LG, Hellsten S, Lindblad B, et al. Determination of the relative glomerular filtration rate of each kidney in man. Comparison

between iohexol CT and 99mTc-DTPA scintigraphy. Acta radiologica (Stockholm, Sweden : 1987). 1995;36(4):410-7.

212. Fowler JC, Beadsmoore C, Gaskarth MT, Cheow HK, Bernal R, Hegarty P, et al. A simple processing method allowing comparison of renal enhancing volumes derived from standard portal venous phase contrast-enhanced multidetector CT images to derive a CT estimate of differential renal function with equivalent results to nuclear medicine quantification. The British journal of radiology. 2006;79(948):935-42.

213. Frennby B, Almen T. Use of spiral CT and the contrast medium iohexol to determine in one session aortorenal morphology and the relative glomerular filtration rate of each kidney. European radiology. 2001;11(11):2270-7.

214. Tsushima Y, Blomley MJ, Okabe K, Tsuchiya K, Aoki J, Endo K. Determination of glomerular filtration rate per unit renal volume using computerized tomography: correlation with conventional measures of total and divided renal function. The Journal of urology. 2001;165(2):382-5.

215. Helck A, Sommer WH, Klotz E, Wessely M, Sourbron SP, Nikolaou K, et al. Determination of glomerular filtration rate using dynamic CT-angiography: simultaneous acquisition of morphological and functional information. Investigative radiology. 2010;45(7):387-92.

216. Helck A, Schonermarck U, Habicht A, Notohamiprodjo M, Stangl M, Klotz E, et al. Determination of split renal function using dynamic CT-angiography: preliminary results. PloS one. 2014;9(3):e91774.

217. Wichmann JL, Booz C, Wesarg S, Kafchitsas K, Bauer RW, Kerl JM, et al. Dual-energy CT-based phantomless in vivo three-dimensional bone mineral density assessment of the lumbar spine. Radiology. 2014;271(3):778-84.

218. Wesarg S, Kirschner M, Becker M, Erdt M, Kafchitsas K, Khan MF. Dual-energy CT-based assessment of the trabecular bone in vertebrae. Methods Inf Med. 2012;51(5):398-405.

219. Bredella MA, Daley SM, Kalra MK, Brown JK, Miller KK, Torriani M. Marrow Adipose Tissue Quantification of the Lumbar Spine by Using Dual-Energy CT and Single-Voxel (1)H MR Spectroscopy: A Feasibility Study. Radiology. 2015;277(1):230-5.

220. Ali IT, Wong WD, Liang T, Khosa F, Mian M, Jalal S, et al. Clinical Utility of Dual-Energy CT Analysis of Bone Marrow Edema in Acute Wrist Fractures. AJR American journal of roentgenology. 2018;210(4):842-7.

221. Kaup M, Wichmann JL, Scholtz JE, Beeres M, Kromen W, Albrecht MH, et al. Dual-Energy CT-based Display of Bone Marrow Edema in Osteoporotic Vertebral Compression Fractures: Impact on Diagnostic Accuracy of Radiologists with Varying Levels of Experience in Correlation to MR Imaging. Radiology. 2016;280(2):510-9.

222. Poort LJ, Stadler AAR, Ludlage JHB, Hoebers FJP, Kessler P, Postma AA. Detection of Bone Marrow Edema Pattern With Dual-Energy Computed Tomography of the Pig Mandible Treated With Radiotherapy and Surgery Compared With Magnetic Resonance Imaging. Journal of computer assisted tomography. 2017;41(4):553-8.

223. Lv P, Lin XZ, Li J, Li W, Chen K. Differentiation of small hepatic hemangioma from small hepatocellular carcinoma: recently introduced spectral CT method. Radiology. 2011;259(3):720-9.

224. Mileto A, Nelson RC, Marin D, Roy Choudhury K, Ho LM. Dual-energy multidetector CT for the characterization of incidental adrenal nodules: diagnostic performance of contrast-enhanced material density analysis. Radiology. 2015;274(2):445-54.

225. Chae EJ, Song JW, Krauss B, Song KS, Lee CW, Lee HJ, et al. Dual-energy computed tomography characterization of solitary pulmonary nodules. Journal of thoracic imaging. 2010;25(4):301-10.

226. Yamada Y, Jinzaki M, Tanami Y, Abe T, Kuribayashi S. Virtual monochromatic spectral imaging for the evaluation of hypovascular hepatic metastases: the optimal monochromatic level with fast kilovoltage switching dual-energy computed tomography. Investigative radiology. 2012;47(5):292-8.

227. Lin XZ, Wu ZY, Tao R, Guo Y, Li JY, Zhang J, et al. Dual energy spectral CT imaging of insulinoma-Value in preoperative diagnosis compared with conventional multi-detector CT. European journal of radiology. 2012;81(10):2487-94.

228. Zhang LJ, Yang GF, Wu SY, Xu J, Lu GM, Schoepf UJ. Dual-energy CT imaging of thoracic malignancies. Cancer imaging : the official publication of the International Cancer Imaging Society. 2013;13:81-91.

229. Schabel C, Patel B, Harring S, Duvnjak P, Ramirez-Giraldo JC, Nikolaou K, et al. Renal Lesion Characterization with Spectral CT: Determining the Optimal Energy for Virtual Monoenergetic Reconstruction. Radiology. 2018;287(3):874-83.

230. Forghani R, Kelly HR, Curtin HD. Applications of Dual-Energy Computed Tomography for the Evaluation of Head and Neck Squamous Cell Carcinoma. Neuroimaging clinics of North America. 2017;27(3):445-59.

231. Pan Z, Pang L, Ding B, Yan C, Zhang H, Du L, et al. Gastric cancer staging with dual energy spectral CT imaging. PloS one. 2013;8(2):e53651.

232. Chen CY, Hsu JS, Jaw TS, Wu DC, Shih MC, Lee CH, et al. Utility of the iodine overlay technique and virtual nonenhanced images for the preoperative T staging of colorectal cancer by dual-energy CT with tin filter technology. PloS one. 2014;9(12):e113589.

233. Bamberg F, Dierks A, Nikolaou K, Reiser MF, Becker CR, Johnson TR. Metal artifact reduction by dual energy computed tomography using monoenergetic extrapolation. European radiology. 2011;21(7):1424-9.

234. Cuculich PS, Schill MR, Kashani R, Mutic S, Lang A, Cooper D, et al. Noninvasive Cardiac Radiation for Ablation of Ventricular Tachycardia. The New England journal of medicine. 2017;377(24):2325-36.

235. Scheffel H, Alkadhi H, Plass A, Vachenauer R, Desbiolles L, Gaemperli O, et al. Accuracy of dual-source CT coronary angiography: First experience in a high pre-test probability population without heart rate control. European radiology. 2006;16(12):2739-47.

236. Jin KN, De Cecco CN, Caruso D, Tesche C, Spandorfer A, Varga-Szemes A, et al. Myocardial perfusion imaging with dual energy CT. European journal of radiology. 2016;85(10):1914-21.

237. So A, Hsieh J, Narayanan S, Thibault JB, Imai Y, Dutta S, et al. Dual-energy CT and its potential use for quantitative myocardial CT perfusion. Journal of cardiovascular computed tomography. 2012;6(5):308-17.

238. Winklhofer S, Lambert JW, Sun Y, Wang ZJ, Sun DS, Yeh BM. Pelvic Beam-Hardening Artifacts in Dual-Energy CT Image Reconstructions: Occurrence and Impact on Image Quality. AJR American journal of roentgenology. 2016:1-10.

239. Szucs-Farkas Z, Kurmann L, Strautz T, Patak MA, Vock P, Schindera ST. Patient exposure and image quality of low-dose pulmonary computed tomography angiography: comparison of 100- and 80-kVp protocols. Investigative radiology. 2008;43(12):871-6.

240. McCollough CH, Leng S, Yu L, Fletcher JG. Dual- and Multi-Energy CT: Principles, Technical Approaches, and Clinical Applications. Radiology. 2015;276(3):637-53.
241. Ameli-Renani S, Rahman F, Nair A, Ramsay L, Bacon JL, Weller A, et al. Dual-energy CT for imaging of pulmonary hypertension: challenges and opportunities. Radiographics : a review publication of the Radiological Society of North America, Inc. 2014;34(7):1769-90.
242. Patino M, Prochowski A, Agrawal MD, Simeone FJ, Gupta R, Hahn PF, et al. Material Separation Using Dual-Energy CT: Current and Emerging Applications. Radiographics : a review publication of the Radiological Society of North America, Inc. 2016;36(4):1087-105.
243. Hsu SH, Cao Y, Huang K, Feng M, Balter JM. Investigation of a method for generating synthetic CT models from MRI scans of the head and neck for radiation therapy. Physics in medicine and biology. 2013;58(23):8419-35.